Advanced Drug Delivery Reviews 105 (2016) 109–144

Contents lists available at ScienceDirect

Advanced Drug Delivery Reviews

journal homepage: www.elsevier.com/locate/addr

Toxicology of graphene-based nanomaterials☆

Gaurav Lalwani [a,b,*], Michael D'Agati [b], Amit Mahmud Khan [b], Balaji Sitharaman [a,b,**]

[a] Theragnostic Technologies Inc., Long Island High Technology Incubator Suite 123, Stony Brook, NY 11790, USA
[b] Department of Biomedical Engineering, Stony Brook University, Stony Brook, NY 11794-5281, USA

ARTICLE INFO

Article history:
Received 22 January 2016
Received in revised form 28 March 2016
Accepted 26 April 2016
Available online 3 May 2016

Keywords:
Graphene
Toxicity
In vitro
In vivo
Antimicrobial
Environmental
Biodistribution

ABSTRACT

Graphene based nanomaterials possess remarkable physiochemical properties suitable for diverse applications in electronics, telecommunications, energy and healthcare. The human and environmental exposure to graphene-based nanomaterials is increasing due to advancements in the synthesis, characterization and large-scale production of graphene and the subsequent development of graphene based biomedical and consumer products. A large number of *in vitro* and *in vivo* toxicological studies have evaluated the interactions of graphene-based nanomaterials with various living systems such as microbes, mammalian cells, and animal models. A significant number of studies have examined the short- and long-term *in vivo* toxicity and biodistribution of graphene synthesized by variety of methods and starting materials. A key focus of these examinations is to properly associate the biological responses with chemical and morphological properties of graphene. Several studies also report the environmental and genotoxicity response of pristine and functionalized graphene. This review summarizes these *in vitro* and *in vivo* studies and critically examines the methodologies used to perform these evaluations. Our overarching goal is to provide a comprehensive overview of the complex interplay of biological responses of graphene as a function of their physiochemical properties.

Contents

☆ This review is part of the *Advanced Drug Delivery Reviews* theme issue on "Graphene-based materials in nanomedicine".

* Correspondence to: G. Lalwani, Theragnostic Technologies Inc., Long Island High Technology Incubator Suite 123, Stony Brook, NY 11790, United States. Tel.: +1 631 512 3980.
** Correspondence to: B. Sitharaman, Department of Biomedical Engineering, Bioengineering Building Room 115, Stony Brook University, Stony Brook, NY 11794-5281, United States. Tel.: +1 631 632 1810.
E-mail addresses: gauravlalwani06@gmail.com (G. Lalwani), balaji.sitharaman@stonybrook.edu (B. Sitharaman).

http://dx.doi.org/10.1016/j.addr.2016.04.028
0169-409X/

1. Introduction

Carbon nanomaterials such as fullerenes, carbon nanotubes and graphene are the most widely researched class of materials and hold immense potential to impact several scientific disciplines [1–3]. Their transformative potential has been recognized with multiple honors including the Kavli and Nobel Prize [4,5]. Owing to the distinct arrangement of sp^2 bonded carbon atoms, each carbon nanomaterial can exhibit significantly different physical, morphological and chemical properties.

Graphene, a two-dimensional (2D) sheet of carbon atoms packed in a honeycomb lattice is widely regarded as a basic building block of graphitic allotropes (Fig. 1) [6]. The theoretical existence of graphene was discussed over 55 years ago by Slonczewski and Weiss [7]. Landau, Peierls and Mermin reported that existence of atomically thin 2D crystals (such as graphene) was practically impossible due to thermodynamic instabilities, a theory that was supported by several independent experimental observations [8–11]. However, in 2004, Novoselov and Geim isolated single sheets of graphene by micromechanical cleavage of graphite or the "scotch-tape method" [12] and characterized their quantum electrodynamics [13,14]. Since then research on graphene has exploded. The number of research papers published on graphene has been increasing exponentially (Fig. 2) attracting scientists from all areas of science and technology towards the graphene "gold-rush". In 2013, the European Union announced the graphene flagship project — a $1.3 billion 10 year investment in graphene research and development to translate graphene-based technologies from academic labs to the marketplace [15]. The Korean Graphene Project, also announced in 2013, is a $44 million 5 year investment for graphene research [16]. In 2011, United Kingdom committed £50 million investment for graphene research [17]. Recently, in October 2015, Chinese company Huawei Technologies has announced a $1 billion 5 year investment towards the development of information and communication technologies focused on graphene [18].

Graphene has interesting optical, thermal, mechanical and electrical properties. The sp^2 hybridization of 2D graphene plane results in delocalized out of plane π bonds that provide an exceptionally high carrier mobility (~200,000 $cm^2 V^{-1} s^{-1}$ for suspended graphene [19,20] and ~500,000 $cm^2 V^{-1} s^{-1}$ for graphene-based field effect transistors) [21,22]. Graphene exhibits room temperature quantum hall effect for electrons and holes [13,23]. Graphene sheets also exhibit high surface area (2630 $m^2 g^{-1}$) [21], thermal conductivity (~5000 $Wm K^{-1}$) [24], mechanical property (Young's modulus of ~1 TPa) [25] and optical transparency (single layer graphene absorbs ~2.3% of visible light) [26].

Graphene can be synthesized using various physical (such as mechanical cleavage ("scotch tape method") [27] or arc discharge [28]) and chemical methods (chemical vapor deposition [29], Hummer's method (chemical oxidation of graphite followed by mechanical exfoliation) [30] or longitudinal unzipping of carbon nanotubes [31]). Depending on the method of synthesis, graphene can exist in various morphologies such as sheets, platelets, ribbons, onions and quantum dots (Fig. 3). Pristine graphene is apolar and very hydrophobic. It needs to be oxidized to improve its dispersibility in aqueous media.

Oxidized graphene is typically synthesized via chemical oxidation. Depending on the synthesis or morphology of the graphene, oxidized graphene are referred by various terminologies. For example, oxidized

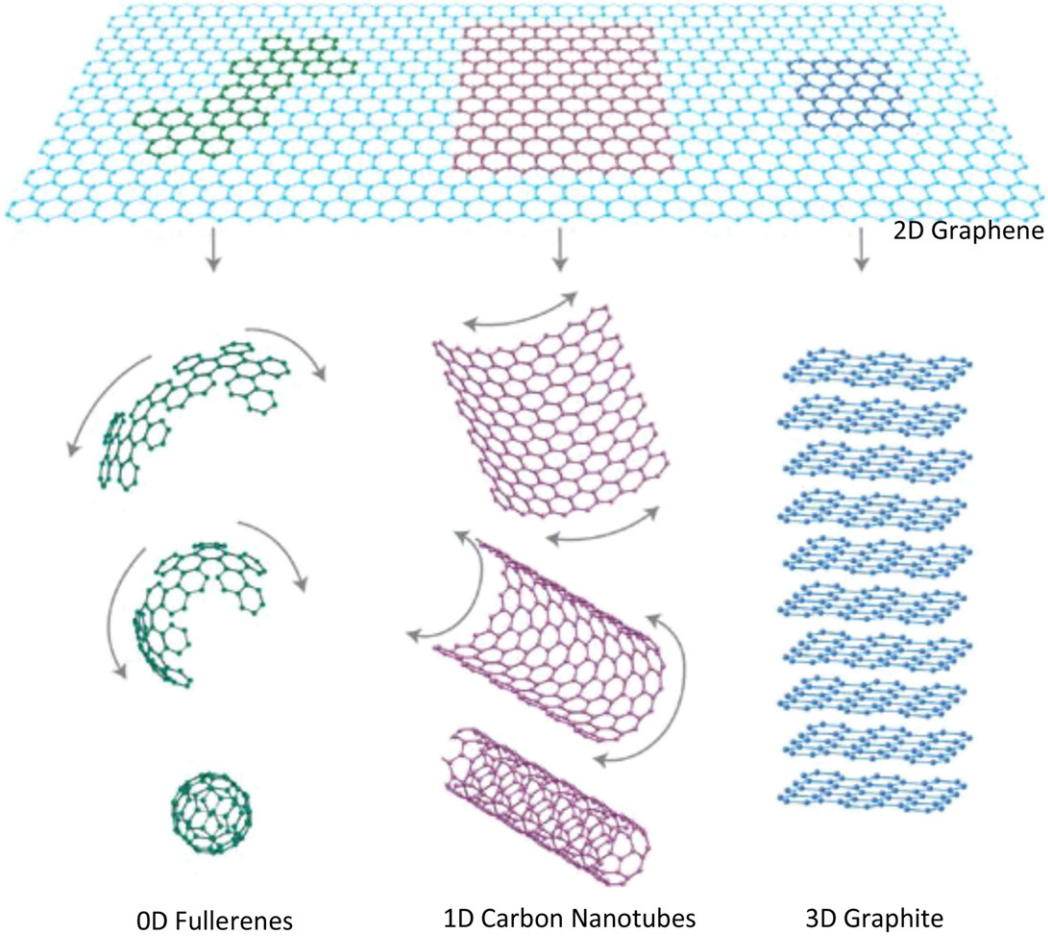

Fig. 1. Graphene is the building material for 0D fullerenes, 1D carbon nanotubes and 3D graphite.
Schematic adapted from Reference [6] with permission, copyright © Macmillan Publishers Limited, 2007.

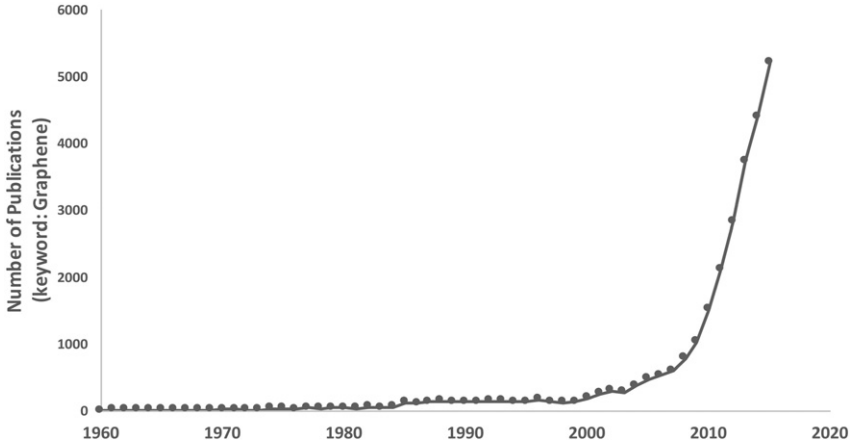

Fig. 2. Number of publications with the keyword 'graphene' from 1960 to 2015. Data retrieved from PubMed (www.ncbi.nlm.nih.gov).

graphene prepared by Hummer's method is typically referred as graphene oxide (GO) or graphene nanoplatelet. Oxidized graphene prepared by longitudinal unzipping are referred as graphene oxide nanoribbons. The pristine sp^2 characteristic of graphene can to a large extend (but not completely) be restored by treating oxidized graphene nanoparticles with reducing agents such as hydrazine and hydrogen iodide [32]. Although the presence of hydrogen bonds between the polar oxidative functional groups (such as oxide, acid, alcohol, and epoxide) of oxidized graphene imparts colloidal stability, the dispersibility of oxidized graphene in aqueous and biological media is inadequate for several biomedical applications. Functionalization strategies have been employed to further improve graphene's aqueous dispersibility. Graphene can be covalently or non-covalently functionalized with several chemical moieties (for instance amine) or biological molecules (such as nucleic acids and proteins). Oxidized graphene nanoparticle-based formulations has been extensively explored for several biomedical applications such as bioimaging [33–35], drug and gene delivery [36–38], photothermal therapy [39,40], tissue engineering [41–43], and stem cell technology [44,45]. Pristine or nearly pristine (oxidized graphene treated with reducing agents) graphene have also been investigated for several biomedical applications [27,35,46,47].

The evaluation of *in vitro* cytotoxicity and *in vivo* biocompatibility is critical to develop nanoparticle-based formulations for biomedical applications. The potential widespread use of graphene-based nanomaterials for commercial materials science applications will increase their interactions with biological and environmental constituents. Furthermore, a thorough analysis of the biocompatibility of graphene is an essential prerequisite before their use for *in vivo* biomedical applications. Consequently, several studies have been performed to assess the *in vitro* and *in vivo* cyto- and bio-compatibility of graphene-based nanomaterials [48–56]. These studies indicate that the toxicity of graphene is dependent on the complex interplay of several physiochemical properties such as shape, size, oxidative state, functional groups, dispersion state, synthesis methods, route and dose of administration, and exposure times [48–57]. Post synthesis processing steps could lead to disruption of graphene structure and production of smaller carbonaceous debris or methods to synthesize graphene could lead to the incorporation of several metallic impurities in the final product. These confounding factors may elicit variable toxicity responses [58–60].

In this article, we provide a comprehensive review of recent *in vitro* and *in vivo* toxicity studies using graphene-based nanomaterials and examine the methodologies used to perform these evaluations. We also review studies investigating the effects of graphene on antimicrobial biota (e.g. bacteria and fungi) and environmental constituents (e.g. crops, waste water). Finally we summarize the current understanding of the toxicity mechanisms of graphene-based nanomaterials. The goal of this article is to provide the readers with an overview on graphene toxicity and its dependence on the various physiochemical properties of graphene. Such an understanding could lead to development of strategies to mitigate potential adverse effects towards successful development of graphene-based consumer and healthcare products.

2. *In vitro* toxicity

The assessment of *in vitro* cytotoxicity is the initial step towards significantly expensive and elaborate *in vivo* studies. Table 1 summarizes the *in vitro* cytotoxicity of graphene and graphene oxide (GO) assessed using several representative cell lines at various treatment concentrations.

2.1. Dose, time, and morphology dependent cytotoxicity

Zhang et al. investigated the interactions of graphene (diameter 100–110 nm, thickness 3–5 nm) with rat pheochromocytoma PC12 cells using 3-(4,5-dimethylthiazol-2-yl)-2,5-diphenyltetrazolium bromide (MTT) and lactate dehydrogenase (LDH) assays and compared the results with single-walled carbon nanotubes (SWCNTs) [61]. More than 70% cell death was observed for 100 μg/ml treatment concentration of SWCNTs whereas no cell death was observed for 0.01–10 μg/ml concentrations of graphene (Fig. 4A). Nearly 15–20% cell death was observed for graphene treatment at 100 μg/ml. The observed cytotoxicity was attributed to the agglomeration of graphene, generation of reactive oxygen species (Fig. 4B) and an increased caspase-3 activation (Fig. 4C) resulting in apoptosis. These results showed a dose dependent cytotoxicity trend that was dependent on the morphology (shape and composition) of the nanomaterial, with graphene exhibiting an overall lower toxicity compared to single-walled carbon nanotubes (SWCNTs). Vallabani et al. investigated the toxicity of graphene oxide using normal human lung cells (BEAS-2B) after 24 and 48 h of exposure at concentrations between 10 and 100 μg/ml. A significant dose- and time-dependent decrease in cell viability and an increase in the number of early and late apoptotic cells was observed using MTT assay [62].

Yuan et al. evaluated the cytotoxicity of graphene oxide on human hepatoma HepG2 cells using MTT assay, DFDA fluorescence analysis and 2D LC–MS proteome analysis [63]. After 48 h of exposure to GO at 1 μg/ml concentration, HepG2 cells showed 6% mitochondrial damage, 8% increase in ROS generation and no significant changes in apoptotic cell population, cell cycle, and expression of metabolic and cytoskeletal proteins. Cells treated with oxidized-SWCNTs (ox-SWCNTs) showed ~20% mitochondrial damage, >100% increase in ROS generation, ~26% increase in apoptotic cell population, and ~30 differentially expressed

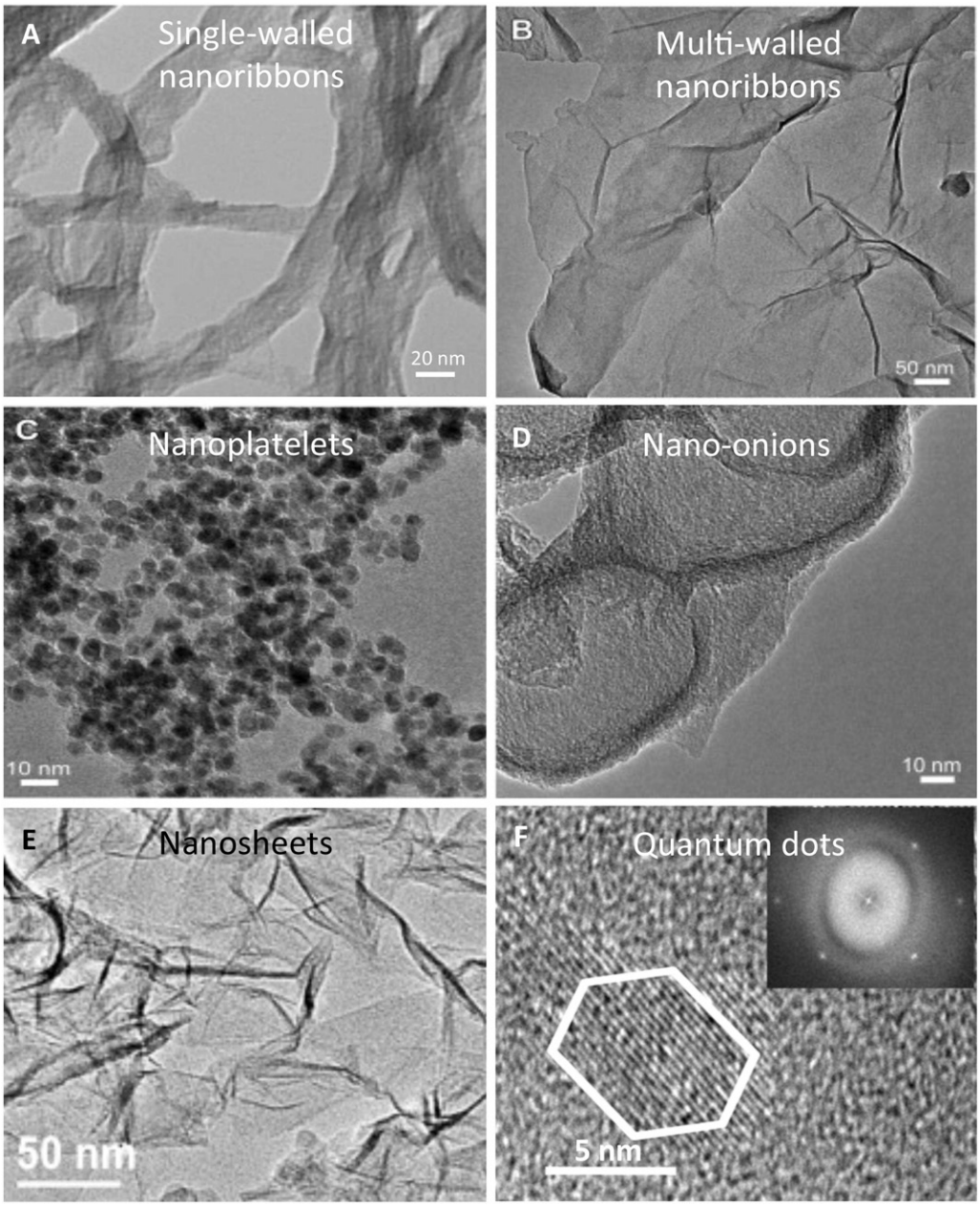

Fig. 3. Representative transmission electron microscopy images of (A and B) graphene nanoribbons, (C) graphene nanoplatelets, (D) graphene nanoonions, (E) graphene nanosheets and (F) graphene quantum dots.
Image (A) adapted from Reference [41], (B–D) adapted from Reference [44], (E) adapted from Reference [95] and (F) adapted from Reference [145], with permissions. (A) copyright © American Chemical Society 2013, (B–D) copyright © Elsevier 2014, (E) copyright © Elsevier 2015, and (F) copyright © American Chemical Society, 2013.

proteins involved in metabolic pathway, redox regulation, cytoskeleton formation, and cell growth. These results suggested that GO may be less cytotoxic compared to ox-SWCNTs. In another study, Lv et al. showed that GO does not elicit cytotoxic or apoptotic effects in human neuroblastoma SH-SY5Y cells at low concentrations (<80 μg/ml) [64]. Interestingly, GO enhanced the retinoic acid induced differentiation of SH-SY5Y cells, improving neurite length and expression of MAP2 (neuronal marker), suggesting that GO may be suitable for applications in neurodegenerative diseases.

Talukdar et al. investigated the effects of graphene nanostructures of various morphologies (such as oxidized-nanoribbons (GONRs), oxidized-nanoplatelets (GONPs), and nanoonions (GNOs)) on the toxicity and stem cell differentiation potential of human mesenchymal stem cells (hMSCs) [44]. hMSCs (derived from bone marrow and adipose tissue) were treated with various concentrations (5–300 μg/ml) of GONRs, GONPs and GNOs for 24 or 72 h and cytotoxicity was evaluated using Alamar blue and CalceinAM assays. Results showed a dose-dependent (no time-dependent) cytotoxicity of various 2D graphene nanostructures with concentrations >50 μg/ml eliciting no cytotoxicity. TEM imaging showed cellular and nuclear uptake of GNOs and GONPs (Fig. 5A–D). Furthermore, results showed that all graphene nanostructures did not induce any changes in the adipogenic and osteogenic differentiation of hMSCs (Fig. 5E–J) suggesting the use of graphene as labels for stem cell imaging and therapy.

Chng et al. have reported a comparative study on the cytotoxicity of GONRs and GONPs [65]. GONRs were synthesized from the longitudinal unzipping of CNTs and GONPs were synthesized from stacked graphene nanofibers. *In vitro* cytotoxicity evaluated using MTT and WST-8 assays

Table 1
In vitro cytotoxicity of graphene.

Material	Characterization	Properties	Treatment concentration	Cell line	Assays	Conclusions	References
Graphene, SWCNT	TEM, SEM, AFM, X-ray diffraction	G: thickness = 3–5 nm	0.01–100 μg/ml	PC12 cells	MTT, LDH, ROS, caspase 3/7	Dose and shape dependent cytotoxicity was observed for graphene and SWCNT.	Zhang et al. [61]
GO, ox-SWCNT	AFM, FTIR, EDS	GO: length = 100 nm; height = 1 nm	1 μg/ml	HepG2 cells	MTT, ROS, FITC, DFDA fluorescence analysis, 2D LC–MS proteome analysis	GO shows less mitochondrial damage, ROS generation, apoptotic cell population compared to cells treated with ox-SWCNTs.	Yuan et al. [63]
GO	AFM, DLS, FTIR, Uv–Vis	GO: thickness = 1 nm; size = 100–600 nm	10–100 μg/ml	SH-SY5Y cells	MTT, caspase-3	Viability of cells are dose and time dependent. No apoptosis induced by GO. MAP2 expression and neurite length improved.	Lv et al. [64]
GNO, GONP, GONR (PEG-DSPE dispersed)	TEM, Raman, TGA, zeta potential, hydrodynamic diameter	GNO: diameter = 50–300 nm; I_D/I_G = 0.92; ζ-potential = −32.3 ± 1.35; hydrodynamic radius = 460.76 ± 53.58 GONR: width = 60–90 nm, length = 500–1500 nm; I_D/I_G = 1.28; ζ-potential = −26.3 ± 0.75; hydrodynamic radius = 457.5 ± 35.70 GONP: diameter = 20–40 nm, thickness = 3–5 nm; I_D/I_G = 1.09; ζ-potential = −12.47 ± 0.12; hydrodynamic radius = 296.4 ± 20.32	5–300 μg/ml	Human adMSCs and bmMSCs	Alamar blue, calcein AM, adipogenic differentiation (oil red O) and osteogenic differentiation (alizarin red, ALP, calcium deposition)	Dose dependent cytotoxicity (not time dependent; Graphene does not affect differentiation potential of human stem cells.	Talukdar et al. [44]
GONR and GONP	Raman, XPS	GONR: I_D/I_G = 1.09; lattice size = 22.2 nm; C/O ratio = 1.9; percentage of C═O groups = 28.22 GONP: I_D/I_G = 0.88; lattice size = 19.1 nm; C/O ratio = 1.9; percentage of C═O groups = 11.06	3–400 μg/ml	A549 cells	MTT, WST-8	Size and functional group dependent toxicity; GONR exhibit greater toxicity than GONP due to presence of greater number of carbonyl groups and greater length	Chng et al. [65]
GONR, rGONR, GOS and rGOS	TEM, SEM, AFM, XPS, Raman spectroscopy	GONR and rGONR: length = 10 μm, width = 50–200 nm; thickness = 1 nm; O/C ratio = 54% for GONR and 19% for rGONR; increase in I_D/I_G ratio upon reduction GOS and rGOS: thickness = 1.2 nm; lateral size = 2 μm; reduction in oxygen content and increase in I_D/I_G ratio upon reduction	0.01–100 μg/ml	Human MSCs	ROS assay, RNA efflux, cell viability (FDA) assay, Comet assay, Giemsa staining	Dose and shape dependent cytotoxicity with GONRs more cytotoxic than GOS. GONRs and rGONRs induce DNA fragmentation and chromosomal aberrations at 1 μg/ml.	Akhavan et al. [66]
GP	TEM, z-potential	GP: diameter = 450 nm–1.5 μm; z-potential = −9.61	5–100 μg/ml	U87, U118	Trypan blue, XXT-based proliferation, LDH, apoptosis kit	Activated apoptosis and necrosis in U87 cells whereas only apoptosis was activated in U118 cells.	Jaworski et al. [67]
Pristine-G, COOH-GO	TEM, AFM, Raman, XPS	Thickness = 0.5 μm	0–300 μg/ml	Vero cells	Alamar blue, LDH, apoptosis, ROS	Surface functionalization of graphene is critical for pacifying strong hydrophobic interaction associated with toxicity effects.	Sasidharan et al. [68]
GQD-NH_2, GQD-COOH, GQD-CO-N(CH_3)$_2$	UV–Vis, TEM, FTIR	GQD-NH_2: diameter = 7.5 nm; UV–Vis peak = 230 nm; Ex/Em = 420/500 nm; FTIR peaks at 1627 cm^{-1} (C═O), 1417 cm^{-1} (N–H), 1328 cm^{-1} (C–N), GQD-COOH: diameter = 15 nm; UV–Vis peak = 362 nm; Ex/Em = 400/440 nm; FTIR peaks at 1388 and 1571 cm^{-1} (COO–), GQD-CO-N(CH3)2: diameter = 3–10 nm; UV–Vis peak = 300 nm; Ex/Em = 400/500 nm; FTIR peaks at 1400 and 1304 cm^{-1} (C–N)	0–200 μg/ml	A549 and C6 glioma cells	MTT, Trypan blue, fluorescence imaging	No cytotoxic effects upto 200 μg/ml treatment for all GQDs. Intracellular accumulation of GQDs was observed, nuclear translocation was absent.	Yuan et al. [70]

(continued on next page)

Table 1 (*continued*)

Material	Characterization	Properties	Treatment concentration	Cell line	Assays	Conclusions	References
GO and rGO	AFM, EDX, aerodynamic diameter (d_{ae})	Lateral dimension = 100 nm–5 μm; height = 1.1–15 nm; d_{ae} = 20–200 nm; oxygen content = 40% in GO and 10% in rGO	0.0125–12.5 μg/cm^2	A549 and RAW 264.7 cells	MTT, DNA assay, FMCA assay, apoptosis, ROS, cell TEM	Dose dependent cytotoxicity. Cellular internalization of GO inside phagoendosomes was observed	Horváth et al. [71]
PEG-amine functionalized GO	TEM, AFM, FTIR, DLS	Thickness = 1.8 nm; hydrodynamic size = 10–120 nm;	75 μg/ml	Saos-2 osteoblasts, MC3t3-E1 preosteoblast, RAW-264.7 macrophages	ROS, Hoechst 33,258, Gen-Probe Diaclone kit	After internalization, nanosheets are localized on F-actin filaments inducing cell-cycle alterations, apoptosis, and oxidative stress.	Matesanz et al. [69]
GO, rGO	AFM, TEM, XPS, Raman spectroscopy	Flake size = 0.4–0.8 μm; thickness = 1 nm	1–10 μg/ml	HUVEC	MTT, LDH, ROS, FACS, RT-PCR, Comet assay	Oxidation state, dose and size dependent cytotoxicity. GO exhibits higher toxicity than rGO due to ROS generation. Small flake size graphene exhibit greater cytotoxicity compared to larger sheets due to intracellular accumulation of graphene.	Das et al. [72]
GQD-PEG	AFM, TEM, FTIR, TGA, XPS, elemental analysis	Diameter = 3–5 nm; height = 0.5–1 nm; 1–2 graphene layers; oxygen content 36%	10–640 μg/ml	HeLa, A549	WST-1, annexin V and PI, LDH, ROS,	No cytotoxicity; (HeLa cells treated with 160 μg/ml and A549 cells with 320 μg/ml doses show no cytotoxicity)	Chong et al. [73]
TRGO-Cl, TRGO-Br, TRGO-I	Raman spectroscopy, elemental analysis, XPS	TRGO-Cl: crystallite size/nm = 14.4, amt. of halogen = 2.1, C/O = 16.77; TRGO-Br: crystallite size/nm = 15.4, amt. of halogen = 1.6, C/O = 20.37; TRGO-I: crystallite size/nm = 22.3, amt. of halogen = 0.2, C/O = 11.75.	0–200 μg/ml	A549	MTT, WST-8	Dose-dependent cytotoxicity between 3.125 and 200 μg/ml. Cytotoxicity depends on the amount of halogen content and follows the trend: TRGO-Cl > TRGOO-Br > TRGO-I.	Teo et al. [74]
Fluorinated Graphene (F-G)	SEM, Elemental analysis, XPS, FTIR, XRD	Three different formulations with varying F content − 1.5%, 42.6%, 50.7%, C═C (284.5 eV), C–F (289 eV), C–F_2 (284.5 eV), C–CF (286.1 eV), C–CF_2 (287.3 eV), CF–CF_2 (290.5 eV), C–F_3 (293.5 eV); FTIR peaks at 1150 cm^{-1} (C–F)	0–400 μg/ml	A549	MTT, WST-8	Dose-dependent cytotoxicity of fluorinated graphene with greater cytotoxicity for graphene containing higher mono-fluoro substituted carbon atoms.	Teo et al. [75]
Highly hydrogenated graphene (HHG) and GO	XPS, elemental analysis	HHG: C/O ratio (8.79), H (37.42%), O (10.41%); GO: C/O ratio (2.78), H (25.72%), O (37.65%)	0–400 μg/ml	A549	MTT, WST-8	Greater cytotoxicity was observed due to increased adsorption of micronutrients on hydrophobic surface of HHG sheets limiting their availability.	Chng et al. [76]
rGO, rGO + Arg, rGO + Pro	TEM, FTIR, zeta ζ potential	Size: 100 nm–1.5 μm. ζ = 19.5 (rGO), 32.5 (rGO + Arg), 39.8 (rGO + Pro) FTIR: rGO: 1769 cm^{-1} (C═O), 1602 cm^{-1} (C═C) and 1289 cm^{-1} (C–O); rGO + Arg and rGO + Pro: 3500–3140 cm^{-1} (O–H, N–H), 1570 cm^{-1} (C–O, C–N), 890–810 cm^{-1} (N–H), 1725 cm^{-1} (C═O)	50 μg/ml	U87	Trypan blue, XTT, gene expression	Reduction in GBM tumor volume was observed. rGO + Arg shows anti-angiogenic and pro-apoptotic characteristics and has potential for GBM therapy.	Sawosz et al. [77]
GONR (PEG-DSPE dispersed)	TEM, Raman	Width = 125–220 nm, length = 500–2500 nm; I_D/I_G = 1.3	10–400 μg/ml	HeLa, MCF-7, SKBR, NIH3T3	Alamar blue, neutral red, Trypan blue, LDH, ROS	Cell type dose, and time dependent cytotoxicity. Significant cell death observed for HeLa cells.	Mullick Chowdhury et al. [36]
rGONP, GONP	AFM, XPS, Raman	GONP: length = 3.8 ± 0.4 μm; thickness = 0.7 nm rGONP: Length = 418 ± 56 nm; thickness = 1.1–2.3 nm	0.01–100 μg/ml	hMSCs	FDA, ROS, RNA efflux, comet	Size dependent cytotoxic response with smaller particles eliciting lower cytotoxicity compared to larger particles. Oxidative stress and direct contact interaction of extremely sharp edges of graphene were determined as most likely mechanisms for cytotoxicity of sheets and nanoplatelets.	Akhavan, et al. [78]

Table 1 (*continued*)

Material	Characterization	Properties	Treatment concentration	Cell line	Assays	Conclusions	References
GO	TEM, AFM, FTIR, Raman spectroscopy, XPS, particle-size distribution and ζ-potential	Large (l-GO): size = 780 ± 410 nm, thickness = 0.9 nm, hydrodynamic diameter = 556 nm, FTIR peaks at 1720 cm^{-1} and band at 3400 cm^{-1}, oxygen content = 33.1%, I_D/I_G = 1.27, ζ-potential = −72.9 Small (s-GO): size = 160 ± 90 nm, thickness = 0.9 nm, hydrodynamic diameter = 148 nm, FTIR peaks at 1720 cm^{-1} and band at 3400 cm^{-1}, oxygen content = 37%, I_D/I_G = 1.26, ζ-potential = −51.9 Mixture (m-GO): size = 430 ± 300 nm, thickness = 0.9 nm, hydrodynamic diameter = 588 nm, FTIR peaks at 1720 cm^{-1} and band at 3400 cm^{-1}, oxygen content = 35.8%, I_D/I_G = 1.25, ζ-potential = −59.2	10–200 μg/ml	A549 cells	CCK-8, Trypan blue, LDH, FITC-annexin V apoptosis, ROS	Cell viability and ROS generation is dependent on the size of GO sheets. Smaller GO sheet exhibit greater cell viability and less ROS generation.	Chang et al. [79]
GO	AFM, stability and dispersion capacity, carboxyl group assay, TEM	GO: length = 350 nm and 2 μm; height = 3.9 and 4.05 nm; thickness = 1 nm;	0–20 μg/ml	PMØ, J774A.1, LLC, MCF-7, HepG2, HUVEC	LIVE/DEAD, CCK8, Coomassie Blue, CLSM, cytokine assay	Cellular internalization independent of graphene size due to differential uptake mechanisms. Removal of Mn from Graphene sheets resulted in reduction of toxicity. Micron sized graphene induced stronger inflammatory response and release of cytokines.	Yue et al. [80]
GO, PVP-GO	AFM, UV–Vis, FTIR	GO: thickness = 1.7 nm; UV absorption peaks at 230 nm and 300 nm; FTIR peaks at 3395 cm^{-1}, 1726 cm^{-1}, 1620 cm^{-1}, 1410 cm^{-1}, 1226 cm^{-1}, 1052 cm^{-1} PVP-GO: thickness = 2.5 nm; UV absorption peak at 265 nm; FTIR peaks at 3395 cm^{-1}, 1726 cm^{-1}, 1620 cm^{-1}	25–100 μg/ml	Dendritic cells, macrophages, T lymphocytes	MTT assay, phenotype assessment, apoptosis assay	PVP functionalized GO sheets are immunocompatible and may be used as adjuvants to improve vaccine therapy	Zhi et al. [81]
Pristine Graphene in 1% F108 pluronic	SEM, XRD, Raman	GO: I_D/I_G = 1.23; thickness = 2–3 nm; size = 500–1000 nm	0–100 μg/ml	RAW 264.7 macrophages	ROS, MMP, apoptosis, TEM, Western-blotting, PCR	Pristine Graphene can induce cytotoxicity through the depletion of mitochondrial membrane potential resulting in the increase of ROS leading to the activation of MAPK and TGF-β that in turn activate caspase-3 and PARP proteins resulting in apoptosis.	Li et al. [82]
GO	AFM, HRXPS, ATR-FTIR, DLS	GO: thickness = 1–1.2 nm; hydrodynamic diameter = 2.4 μm and 350 nm	5 or 100 μg/ml	SNY-449, Mahlavu, A549, HEK293, RAW264.7	TEM, immunofluorescence, Western-blotting, RT-PCR, Flow cytometry, siRNA	GO simultaneously triggers autophagy and activates toll-like receptors TLR4/TLR9 resulting in inflammatory responses.	Chen et al. [83]
GO, C_{60}, C_{60}-TRIS	TEM, SEM, AFM, microscopy, spectroscopy, X-ray diffraction	GO: z-potential = −32.4 mV; C60-fullerenes: z-potential = −13.6; sizes = 45.2 ± 25.3 nm; C_{60}-TRIS fullerenes: z-potential = −26.1; size = 45.6 ± 18.8 nm	1.0, 6.25, 25.0 μg/ml	B3Z T cells	LAL, FITC/Lucifer Yellow	Both C_{60} and graphene capable of modulating antigen-specific T cell responses due to ability to directly affect functional activity of dendritic cells. GO suppresses antigen processing machinery of DCs.	Tkach et al. [84]
GO, GS	X-ray diffraction, AFM, XPS, DLS, Z-potential	GO: diameter = 765 nm; z-potential = −40.6; GS: diameter = 3018 nm; z-potential = −37.2 mV	3–200 μg/ml	Suspended human RBCs and adherent skin fibroblasts	MTT, WST-8, Trypan blue, ROS	Individually dispersed GO leads to greater RBC membrane damage compared to aggregated graphene sheets. Chitosan coated GO show no hemolytic activity	Liao et al. [85]

(*continued on next page*)

Table 1 (*continued*)

Material	Characterization	Properties	Treatment concentration	Cell line	Assays	Conclusions	References
GO, rGO	HR-TEM, 2DFFT, FTIR	Size = 0.2–5 μm	0–20 μg/ml	Human platelets	FITC, immunoblotting, LDH, ROS, Electron Microscopy	GO can evoke strong aggregatory response in platelets comparable to that elicited by thrombin.	Singh et al. [86]
G-NH_2	FTIR, HR-TEM, FFT, Raman, z-potential, FSC, SSC	Size = 2 μm	0–10 μg/ml	Human platelets	ROS, MTT	G-NH2 is not associated with any pro-thrombotic characteristics and does not induce platelet-stimulating response. Membrane integrity of RBCs is maintained.	Singh et al. [94]
GO, rGO	HR-TEM, Raman, UV/vis, XRD	Size = 100–350 nm	3–100 μg/ml	L929 mice fibroblast cells	WST-1	Dose and surfactant dependent cytotoxicity of GO and rGO. Good cytocompatibility observed for concentrations between 3.125 and 12.5 μg/ml of GO and rGO dispersed in PEG.	Wojtoniszak et al. [90]
GNP-Dex	AFM	Diameter = 60–100 nm; thickness = 2–4 nm	1–10 mg/ml	RBL-2H3 mast cells, human platelets	Histamine release, platelet activation, complement activation, cytokine release, blood cell hemolysis	Dextran coated graphene oxide nanoplatelets exhibit no hematological toxicity	Mullick Chowdhury et al. [88]
FBS-GO	TEM, AFM	Thickness = 1 nm	20 and 100 μg/ml	A549 cells	MTT, Bradford protein assay	FBS coating of GO attenuates cytotoxicity	Hu et al. [91]
BSA-GO	FITC-BSA, steady state fluorescence spectra, AFM, Z-potential, SEM, CLSM, flow cytometry, TEM	Flake size: 50 nm or 1 μm; z-potential = −10 mV; thickness = 9.1 ± 7.1 nm	50 μg/ml	C2C12 cells	TEM, SEM, confocal microscopy, WST-1	BSA coated GO sheets exhibit size-dependent internalization. Small GO sheets are internalized by clathrin-mediated endocytosis and large GO sheets are internalized by phagocytosis.	Mu et al. [92]
FBS and human plasma serum functionalized GONRs	AFM, XPS, Raman spectroscopy, FTIR, mass spectrometry	Width = 100 nm; height = 1 nm; FTIR peaks at 3400 cm^{-1} (O–H), 1760 cm^{-1} (C═O), 1300 cm^{-1} (C–OH), 1080 cm^{-1} (C–O); O/C ratio = 0.54; I_D/I_G = 1.38	10–100 μg/ml	A549 cells	Trypan blue and apoptosis assay	Dose dependent cytotoxicity of protein-functionalized GONRs was observed. Concentrations below 50 μg/ml did not exhibit cytotoxic effects.	Mbeh et al. [93]

using human epithelial (A549 cells) showed that GONRs exhibit a significantly higher cytotoxic response than GONPs over all concentrations (3–400 μg/ml). The increased cytotoxicity of GONRs was attributed to the presence of a greater amount of carbonyl groups (28.22% on GONRs vs. 11.06% on GONPs) and the high aspect ratio (width × length of GONRs ~310 × 5000 nm and GONPs ~100 × 100 nm) of GONRs.

Akhavan et al. reported the cyto- and geno-toxicity of reduced GONRs and reduced graphene oxide sheets (rGOS) using human MSCs derived from umbilical cord blood [66]. Cell viability measured by fluorescein diacetate (FDA) test showed that rGONRs are toxic, significant cytotoxicity was observed after 1 h of exposure with rGONRs at 10 μg/ml, while the same cytotoxicity was observed upon incubation with 100 μg/ml of rGOS after 96 h. The cytotoxicity of rGOS was attributed to the generation of oxidative stress whereas the cytotoxicity of rGONRs was attributed to DNA fragmentation and chromosomal aberrations (observed even at low concentrations of ~1 μg/ml after 1 h) due to penetration of rGONRs inside the cells. These results suggested that the cytotoxicity and genotoxicity of graphene is dependent on the dose and shape of the nanomaterial (sheets vs. nanoribbons).

Jaworski et al. reported the interactions of graphene platelets with human glioblastoma U87 and U118 cells [67]. After 24 h of incubation with 100 μg/ml graphene, 42% and 52% cell mortality was observed for U87 and U118 cells, respectively. However, graphene activated

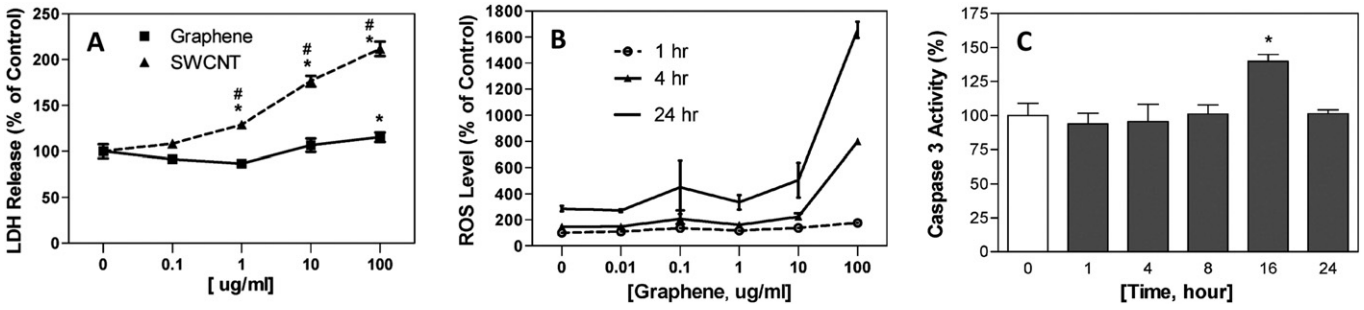

Fig. 4. Effects on (A) lactate dehydrogenase release, (B) reactive oxygen species generation and (C) caspase-3 activity (apoptosis marker) of PC12 cells treated with 0.1–100 μg/ml of graphene and single-walled carbon nanotubes.
Adapted from Reference [61] with permission, copyright © American Chemical Society, 2010.

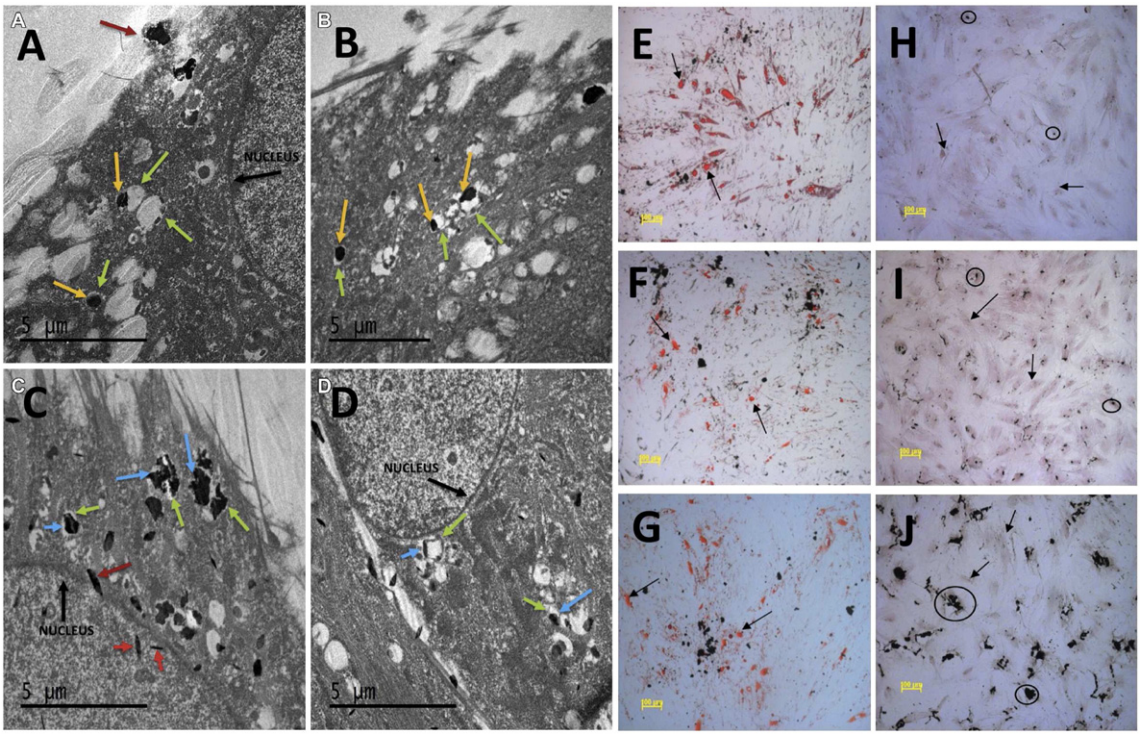

Fig. 5. Representative transmission electron microscopy images of mesenchymal stem cells (MSC) treated with graphene nanoonions (GNOs, A & B) and oxidized-graphene nanoplatelets (GONPs, C & D) at 50 μg/ml for 24 h. Yellow arrows correspond to aggregates of GNO visualized in vacuoles (green arrows). No nuclear uptake of GNOs was observed. Blue arrows correspond to aggregates of GONPs. GONPs were observed inside the nucleus (red arrows). Oil red O staining after adipogenic differentiation of MSC treated with 50 μg/ml of (E) GNO, (F) GONR and (G) GONP. Alizarin Red staining after osteogenic differentiation of MSC treated with 50 μg/ml of (H) GNO, (I) GONR and (J) GONP. No changes in the adipogenic and osteogenic differentiation of MSCs were observed.
Adapted from Reference [44] with permission, copyright © Elsevier, 2014.

apoptosis only in U118 cells not in U87 cells where apoptosis and necrosis both were activated.

2.2. Functionalization dependent cytotoxicity

Sasidharan et al. investigated the cytotoxicity of pristine graphene and carboxylated GO (GO-COOH) using monkey renal cells at concentrations between 10 and 300 μg/ml to assess the differences between cellular interactions of hydrophobic and hydrophilic graphene derivatives [68]. Pristine graphene accumulated on the cell membrane leading to the destabilization of F-actin alignment whereas GO-COOH was internalized by cells and accumulated in the perinuclear region without any membrane destabilization even at 300 μg/ml doses. These results suggested that hydrophilic (more oxidized) graphene nanoparticles may be more cytocompatible and efficient intracellular delivery systems. In another study, Matesanz et al. observed internalization and localization of poly(ethylene glycol amine)-functionalized GO sheets on F-actin filaments resulting in cell-cycle alterations, oxidative stress and apoptosis in MC3T3-E1 murine pre-osteoblasts, Saos-2 osteoblasts and RAW-264.7 macrophage cells [69].

Yuan et al. investigated the cytotoxicity and distribution of three kinds of GQD (NH_2, COOH and CO-N$(CH_3)_2$ functionalized) in human neural glioma C6 and A549 lung carcinoma cells using MTT and Trypan blue assay [70]. Results showed absence of apoptosis or necrosis at all treatment concentrations (10–200 μg/ml) after 24 h for all three GQD groups. Furthermore, Raman spectroscopic analysis showed intracellular accumulation of all three GQDs; nuclear translocation was absent.

Horváth et al. evaluated the toxicity of GO and rGO in A549 human lung epithelial cells and RAW 264.7 mouse peritoneal macrophages using MTT assay, fluorometric DNA assay and fluorometric microculture cytotoxicity assay (FMCA) [71]. Cells treated with 0.0125–12.5 μg/cm^2 of GO or rGO for 5 days showed a dose dependent cytotoxicity. Significant differences in cell death between control and GO or rGO treated cells were observed from day 2 in A549 cells and day 3 in RAW 264.7 macrophages at concentrations of 1.25–12.5 μg/cm^2. Cells treated with lower concentrations of GO (0.0125–0.125 μg/cm^2) did not lead to an increases in ROS production. Cellular internalization of GO was observed in phagoendosomes without signs of any intracellular damage.

Aggregation of pristine graphene in biological buffers could result in greater cytotoxicity in comparison to oxidized graphene derivatives that can be readily dispersed without aggregation during the duration of cytotoxicity studies. Das et al. reported higher cytotoxicity of GO sheets compared to reduced graphene oxide sheets of similar dimensions, an effect attributed to the presence of high density of oxidative functional groups on the surface of GO which lead to the generation of reactive oxygen species [72]. HUVEC cells treated with 1, 5 or 10 μg/ml concentration of GO and rGO showed a dose and functionalization state dependent cytotoxicity. Furthermore, a size dependent cytotoxicity was also observed for both GO and rGO. Upon a 10 fold reduction in the size of oxidized and reduced graphene sheets, smaller graphene nanosheets showed a higher toxicity compared to non-sonicated larger GO or rGO sheets which was attributed to an increased intracellular interaction and uptake of small sized graphene. However, Chong et al. have reported the low cytotoxicity of PEG dispersed graphene quantum dots (>30 nm diameter stacks of 1–10 graphene layers) upto 160 μg/ml for HeLa cells and 320 μg/ml for A549 cells (Fig. 6) [73].

Teo et al. investigated the cytotoxicity of halogenated graphene sheets [74]. GO sheets prepared by oxidation of graphite were thermally reduced with chlorine, bromine, and iodine vapor to form chlorine-, bromine-, and iodine-doped graphene, respectively (TRGO-Cl, TRGO-Br, and TRGO-I). A549 cells were treated with 0–200 μg/ml

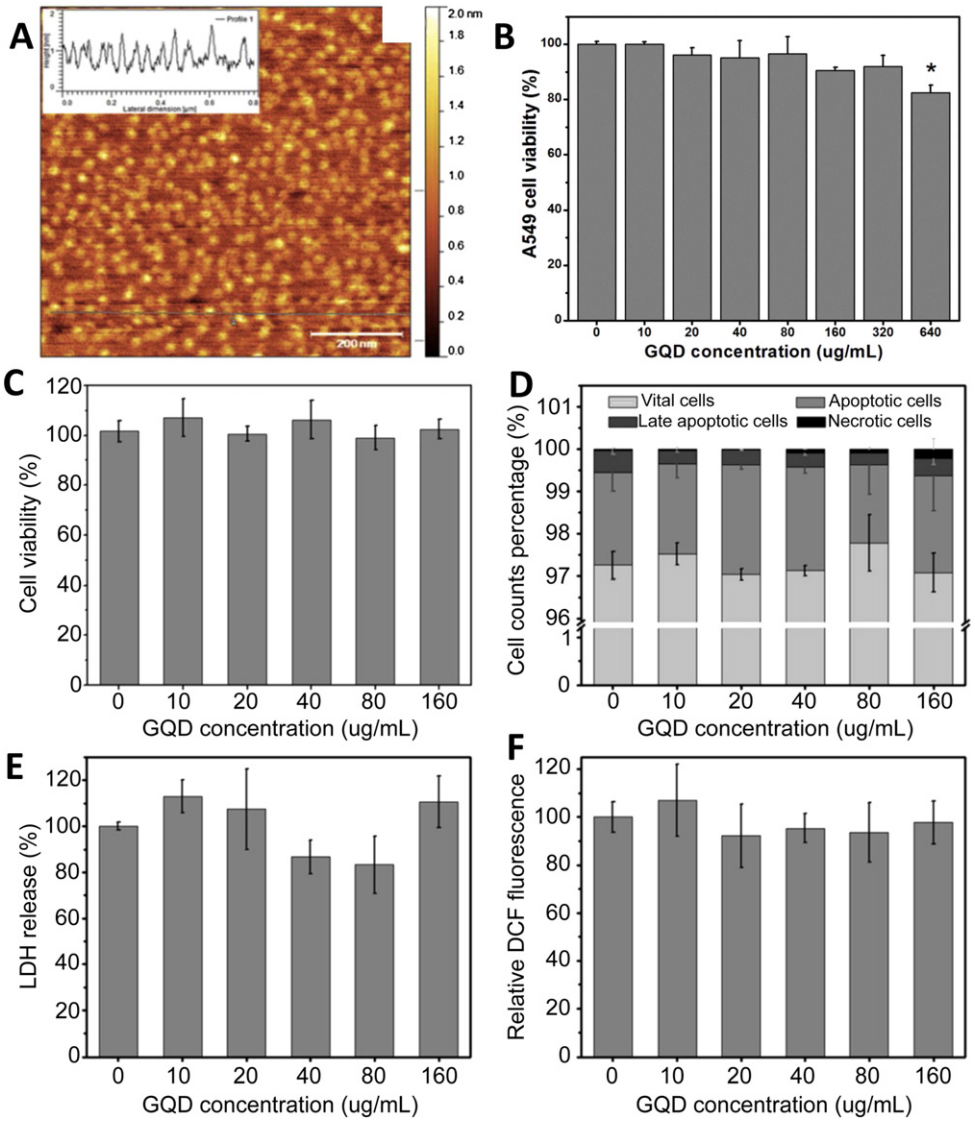

Fig. 6. (A) Representative atomic force microscopy (AFM) image of graphene quantum dots (GQDs). Inset in image A depicts AFM height profile. (B) Cell viability of A549 cells assessed by WST-1 assay. Data reported as means ± SE. No significant differences in cell viability were observed upto a treatment concentration of 320 μg/ml. (C) Cell viability assessed by WST-1 assay, (D) cell apoptosis and necrosis (E) LDH assay and (F) ROS generation by HeLa cells upon treatment with 0–160 μg/ml of GQDs. No toxicity upto 160 μg/ml concentration was observed. Adapted from Reference [73] with permission, copyright © Elsevier, 2014.

concentration of halogenated graphene for 24 h and cell viability was analyzed using MTT and WST-8 assays. Results showed that all halogenated graphene nanoparticles exhibit a dose-dependent cytotoxicity between 3.125 and 200 μg/ml with TRGO-Cl exhibiting highest cytotoxicity (~25.7% cell viability at maximum treatment concentration of 200 μg/ml). The levels of observed cytotoxicity followed the trend: TRGO-Cl > TRGO-Br > TRGO-I and was dependent on the amount of halogen functionalization. In another study, Teo et al. reported the cytotoxicity of fluorinated graphene (FG) [75]. Three types of graphene derivatives with varying amount of fluorine content were prepared (1.5%, 42.6%, and 50.7%). A549 cells were treated with 0–400 μg/ml of fluorinated graphene and cytotoxicity was analyzed using MTT and WST-8 assays. Results show a dose-dependent cytotoxicity response with greater cytotoxicity observed for graphene with higher monofluoro substituted carbon atoms. In a similar study, Chng et al. synthesized highly hydrogenated graphene (HHG) and evaluated their *in vitro* cytotoxicity profile against A548 cells [76]. After 24 h of exposure, MTT and WST-8 assay results show a dose-dependent cytotoxicity of HHG compared to GO controls at all treatment concentrations (0–400 μg/ml). The increased cytotoxicity of HHG was hypothetically attributed to the preferential adsorption of essential micronutrients on the hydrophobic surfaces of HHG compared to hydrophilic surfaces of GO sheets, thereby limiting nutrient availability.

Sawosz et al. have investigated the cytotoxicity of arginine (Arg) and proline (Pro) functionalized rGO using U87 glioblastoma multiforme (GBM) cells and tumors *in vitro* [77]. Cells were treated with 50 μg/ml of rGO, rGO + Arg and rGO + Pro for 24 h and cell viability was evaluated using Trypan blue and XTT assay. Results show ~40% cell death for rGO group and ~15% cell death for rGO + Arg and rGO + Pro groups. GBM tumors cultured on chorioallantoic membrane of chicken embryo were injected with rGO, rGO + Arg and rGO + Pro for 3 days. A greater reduction in tumor volume was observed for rGO group, compared to rGO + Arg and rGO + Pro groups, which reduced the tumor volume albeit lower than rGO. Histological analysis of tumors showed the presence of white gaps and rupture sites indicating necrosis and endothelial proliferation. rGO + Arg were observed close to microglial cells and small blood vessels whereas rGO + Pro were aligned outside the cells in the tissue rather than inside the cells. Tumor cells require arginine for aggressive growth, therefore rGO + Arg were present in the outer layers of tumor — site for active angiogenesis. Gene expression

analysis suggests that rGO + Arg, leads to the down regulation of MDM2 expression and increased expression of NQO1. Furthermore, no change in the expression of COX6 and CASP3 mRNA expression were observed. These results suggest that rGO + Arg is anti-angiogenic and pro-apoptotic and has potential for GBM therapy.

2.3. Cell dependent cytotoxicity

Cytotoxicity of certain types of graphene nanoparticles could be dependent on cell type. Mullick-Chowdhury et al. reported the cytotoxicity screening of graphene oxide nanoribbons (GONRs) dispersed in DSPE-PEG (1,2-distearoyl-sn-glycero-3-phosphoethanolamine-N-[amino(polyethylene glycol)]) using six different assays and four representative cell lines: NIH-3T3 mouse fibroblast cells (NIH-3T3), Henrietta Lacks cells (HeLa) derived from cervical cancer tissue, Michigan cancer foundation-7 breast cancer cells (MCF7), and Sloan Kettering breast cancer cells (SKBR3) [36]. All cell lines exhibit a dose dependent (10–400 μg/ml) and time dependent (12–48 h) decrease in cell viability. HeLa cells showed the least cell viability (5–25%), compared to other cell types (78–100%), depending on the treatment concentration and exposure time. An increased cellular uptake of GONRs was observed and attributed to an increased cytotoxic response in HeLa cells. TEM imaging (Fig. 7) show the formation of cytoplasmic vesicles to facilitate intracellular uptake. Swollen and ruptured plasma membrane was observed suggesting necrotic cell death.

2.4. Size dependent cytotoxicity

Akhavan et al. investigated the cytotoxicity of reduced graphene oxide nanoplatelets (rGONPs) of various sizes (11 ± 4 nm, 91 ± 37 nm and 418 ± 56 nm) and as prepared GO (3.8 ± 0.4 μm) using human mesenchymal stem cells (hMSCs) [78]. The cytotoxicity and cell viability was assessed using fluorescein diacetate (FDA) assay, ROS assay, RNA efflux and Comet assay. Results showed a significant size-dependent cytotoxicity; a treatment concentration of 100 μg/ml rGONPs (11 ± 4 nm) showed >95% cell death which reduced with increasing lateral size dimensions (Fig. 8). As-prepared GO with largest lateral size dimensions (3.8 ± 0.4 μm) showed lowest (~20%) cell death. Results showed that rGONPs can also induce DNA fragmentation even at a low concentration of 0.1 μg/ml.

Chang et al. investigated the cytotoxicity of GO of various sizes (160 ± 90 nm, 430 ± 300 nm and 780 ± 410 nm) using A549 (human lung adenocarcinoma) cells [79]. Cell viability was assessed using CCK-8 assay after 24–72 h of incubation at GO concentrations between 10–200 μg/ml. Small GO sheets (160 ± 90 nm) showed lower cell viability of ~67% compared to large GO sheets (430 ± 300 nm and 780 ± 410 nm) that showed >80% cell viability. However, GO sheets of dimensions 780 ± 410 nm show >50% higher ROS generation compared to GO of dimensions 160 ± 90 nm and 430 ± 300 nm. The results suggested that the cell viability and ROS generation potential of GO is dependent on the size of graphene sheets.

Dasgupta et al. reported the size dependent cytotoxicity of graphene oxide nanoribbons (GONRs) after post processing sonication steps that result in a size reduction of nanoparticles [60]. GONRs were dispersed in cell culture media by bath sonication (5 or 20 min) or probe sonication (1, 5 or 10 min) and MCF-7 and A549 cells were exposed to GONR containing media at 20 μg/ml concentrations. LDH assay, presto blue assay and ROS generation showed that GONR solutions prepared via probe sonication results in a decrease of metabolic stress of cells *in vitro*. No adverse effects were noted when cells were exposed to non-sonicated and bath sonicated solutions of GONRs. TEM analysis showed presence of smaller GONR fragments and carbonaceous debris after probe sonication, which may be the cause of observed cytotoxicity.

Yue et al. reported that cellular internalization and regulation of cellular responses are directly dependent on the lateral dimension of GO [80]. In this study, six representative cell lines (peritoneal macrophage PMØ, murine macrophage J774A.1, murine Lewis lung carcinoma LLC, human breast cancer MCF-7, human hepatocarcinoma cells HepG2, and human umbilical vein endothelial cells HUVEC) were exposed to GO sheets of different sizes (350 nm and 2 μm) at a concentration of 20 μg/ml for cell viability analysis (LIVE/DEAD assay). After 48 h of incubation, a significant cytotoxicity (~40–60% cell death) was detected for all six cell types. However, cell viability was restored upon the removal of manganese (Mn), an impurity present during the oxidative synthesis of GO. Cells upon treatment with Mn-free GO at 20 μg/ml showed ~80–100% cell viability. The results highlighted the importance of purification steps involved during the synthesis of GO to eliminate false positive contributions from metal ions. PMØ and J774A.1 macrophage cells were treated with 2–6 μg/ml of nano- and micro-sized GO. Cellular uptake studies showed that internalization of GO was independent of size and both nano- and micro-sized GO (350 nm and 2 μm) had similar intracellular accumulation. The analyses of uptake mechanisms showed that GO of size 350 nm was wrapped by filopodia of macrophages and internalized whereas GO of 2 μm was internalized via direct penetration. Post cellular internalization, the micron sized GO developed wrinkle formations and appeared to be sequestered into lysosomes. Furthermore, the micron sized GO induced a stronger inflammatory response and release of cytokines. These results suggested that cytokine release and inflammatory response are dependent on the size of GO sheets.

2.5. Immunotoxicity of graphene

Zhi et al. reported the immunotoxicity of GO with and without functionalization by poly(vinyl pyrrolidone) (PVP) against human immune cells such as T lymphocytes, dendritic cells and macrophages [81]. Results showed that PVP-coated GO (PVP-GO) exhibit lower immunogenicity compared to pristine GO at concentrations between 25 and 100 μg/ml. The differentiation and maturation of dendritic cells was unaffected upon incubation with PVP-GO; the levels of secreted TNF-α and IL-1β showed no significant differences between GO and PVP-GO groups, yet the secretion of IL-6 was maintained in PVP-GO group. Incubation with PVP-GO also delayed the apoptosis of T lymphocytes and stimulated and enhanced the physiological activity of macrophages.

Li et al. investigated the interactions of pristine graphene with RAW 264.7 macrophage cells at concentrations between 5 and 100 μg/ml (dispersed in 1% pluronic F108 surfactant) [82]. Pristine graphene showed dose-dependent cytotoxicity in RAW 264.7 cells; ~78% cell death was observed at 100 μg/ml treatment concentrations. Further investigation of the mechanisms of cytotoxicity showed that interaction of pristine graphene with macrophage cell membrane leads to depletion of mitochondrial membrane potential thereby increasing ROS leading to the activation of apoptotic cascade. MAPK and TGF-β signaling pathways were activated which in turn activated two pro-apoptotic proteins (Bim and Bax). Consequently, caspase-3 and PARP proteins were activated triggering apoptosis. The identification of mechanisms of cytotoxicity is extremely important and provides information towards development of strategies to control graphene-induced apoptosis.

Chen et al. showed that GO triggers autophagy (catabolic self-destruction of dysfunctional cellular components) in liver cancer cells (SNU-449 and mahlavu), lung cancer cells (A549), human embryonic kidney cell (HEK293), and RAW 264.7 macrophages by stimulating toll-like receptor signaling cascade (release of cytokines such as IL-2, IFN-γ, IL-10 and TNF-α) at treatment concentrations of 5 or 100 μg/ml [83]. Toll like receptors — TLR4 and TLR9 were activated resulting in GO-mediated inflammatory responses. The results of this study show that GO exposure to cells simultaneously triggers autophagy and TLR4/9 mediated inflammatory responses.

Tkach et al. showed that treatment of dendritic cells (DCs) with GO at 6.25 μg/ml results in an impaired stimulatory potential of DCs (activation of T-cells); treatment with similar concentrations of fullerenes (C_{60} and C_{60}-tris) promotes the ability of DCs to activate T-cells [84]. Further

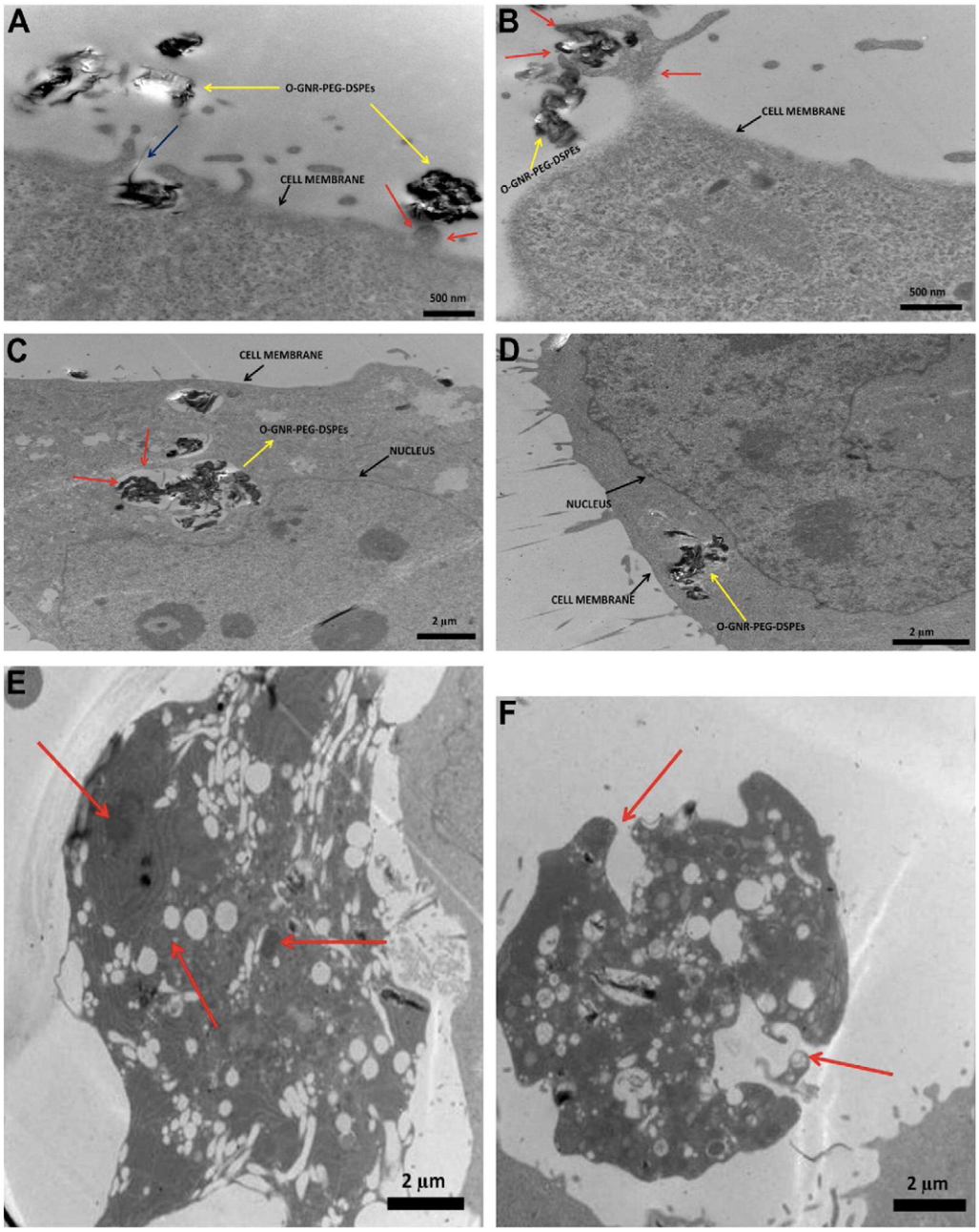

Fig. 7. Representative transmission electron microscopy images of HeLa cells treated with 20 μg/ml of PEG-DSPE dispersed graphene oxide nanoribbons for 3 h. (A) Presence of GONR aggregates towards cell periphery (blue arrows), (B) cell membrane protrusion and internalization of GONRs (red arrows), (C & D) GONR aggregates enclosed in large cytoplasmic vesicles or endosomes (red arrows), (E and F) HeLa cells showing ruptured plasma membrane and swollen vesicles suggesting necrotic cell death after 24 h of exposure to 20 μg/ml DSPE-PEG dispersed GONRs.
Adapted from Reference [36] with permission, copyright © Elsevier, 2013.

analysis showed that GO did not alter antigen uptake by DCs nor inhibit antigen peptide presenting abilities of DCs. However, exposure of DCs to GO resulted in suppression of an immunoproteosome subunit (LMP-7), which is a critical component of MHC-I antigen processing machinery (APM) illustrating the mechanism of inactivation of DCs by GO. These results suggested that GO may modulate antigen-specific T-cell response and emphasized the importance of elaborate assessment of immunomodulatory effects of graphene nanoparticles.

2.6. Hemolytic toxicity of graphene

Hemolytic potential of graphene is dependent on the size and aggregation state of individual nanosheets. Liao et al. investigated the cytotoxicity of graphene and GO using human erythrocytes (RBCs) [85]. Hemolysis was quantified by measuring the amount of hemoglobin released due to RBC membrane damage upon incubation with graphene and GO at 3–200 μg/ml for 3 h. At 200 μg/ml, individually dispersed GO sheets showed ~60% hemolysis, significantly higher than graphene dispersions which showed ~20% hemolysis. The aggregation of graphene in DI water resulted in fewer cell-contractable ROS groups on the surface of graphene. However, cells interact with several ROS species present on the surface of individually dispersed GO, leading to greater hemolysis. Chitosan coated GO aggregate in DI water due to pH dependent conformational change of chitosan resulting in no hemolytic toxicity of GO.

Singh et al. have reported the *in vitro* hemolytic toxicity of GO and rGO using human platelets [86]. Freshly isolated suspension of platelets exposed to GO (2 μg/ml) showed aggregation and platelet activation at

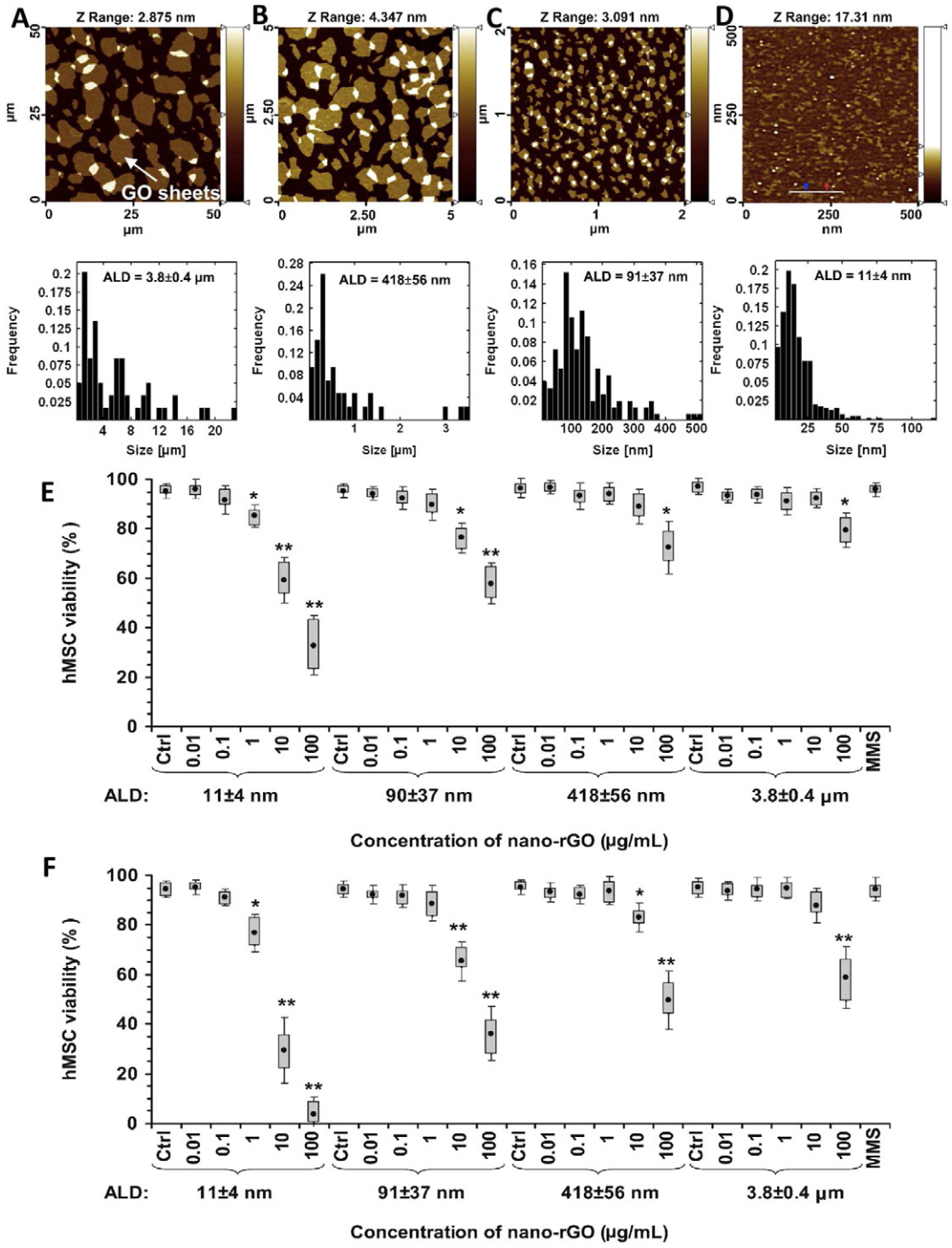

Fig. 8. Representative atomic force microscopy (AFM) images of (A) as-prepared rGO (3.8 ± 0.4 μm), (B) sonicated rGO (418 ± 56 nm), (C) large rGONPs (91 ± 37 nm) and (D) small rGONPs (11 ± 4 nm). Corresponding lateral size distributions are shown below. Images (E and F) show human mesenchymal stem cell viability after treatment with 0.01–100 μg/ml concentration of rGONPs for 1 and 24 h, respectively.
Adapted from Reference [78] with permission, copyright © Elsevier, 2012.

levels greater than induction by thrombin (1 U/ml, a strong platelet agonist). Exposure of platelets to GO resulted in the activation of Src kinases and release of calcium, leading to thrombus formation. In comparison, rGO at 2 μg/ml induced minor platelet aggregation, only 10% of aggregation induced by GO. In another study, Singh et al. showed that amine functionalized GO does not induce lysis of erythrocytes and has no stimulatory effects on platelets highlighting their non-thrombotoxic properties [87]. The results suggested that surface modifications of graphene nanoparticles play an important role towards defining their hemolytic activity.

Mullick Chowdhury et al. showed that graphene oxide nanoplatelets (GONPs) functionalized with biocompatible polymer dextran (GNP-Dex) exhibit no hematological toxicity [88]. RBL-2H3 mast cells and human platelets showed no histamine release, platelet activation or blood cell hemolysis upon treatment with GNP-Dex at concentrations ranging from 1 to 10 mg/ml. At concentrations >7 mg/ml, RBL-2H3 cells showed 12–20% increase in complement protein expression. However, cytokine TNF-alpha and IL-10 levels remained within physiological levels. In another study, Mullick Chowdhury et al. investigated the interactions of DSPE-PEG functionalized graphene oxide nanoribbons

(GONRs) with blood vascular system components [89]. No release of histamine, platelet PF4 activation and complement activation was observed from mast cells upto treatment concentrations of 80 μg/ml. TEM imaging shows significant uptake of GONRs into endothelial cells and exhibit a concentration dependent reduction of cell viability. Results indicated that DSPE-PEG functionalized GONRs could be hemocompatible upto a concentration of 80 μg/ml.

2.7. Surfactant/coating dependent cytotoxicity

Wojtoniszak et al. investigated the cytotoxicity of GO and rGO dispersed using three surfactants (polyethylene glycol (PEG), polyethylene glycol–polypropylene glycol–polyethylene glycol (Pluronic P123), and sodium deoxycholate (DOC)) at concentrations between 3.12 and 100 μg/ml using mice fibroblasts L929 cells [90]. Cytotoxicity analysis using WST-1 assay showed that the cell viability is dependent on the surfactant used to stabilize the suspension, chemical state of material (oxidized or reduced), and the treatment concentration. GO functionalized with PEG exhibits the lowest toxicity (cell viability ~36.3% at 100 μg/ml) whereas GO functionalized with DOC and Pluronic P123 shows 15.5% and 6.3% cell viability, respectively. L929 cells exposed to the PEG dispersed rGO between 3.125 and 25 μg/ml show ~95–60% cell viability. Similar results are observed for rGO functionalized with DOC, however rGO functionalized with Pluronic P123 showed least cell viability. Both, GO and rGO showed good cytocompatibility between 3.125 and 12.5 μg/ml. GO dispersed in PEG showed the best cytocompatibility. These results suggested that GO and rGO exhibit a dose- and surfactant-dependent cytotoxicity.

Hu et al. investigated the cytotoxic effects of fetal bovine serum (FBS) coated GO using A549 cells [91]. At 100 μg/ml exposure, FBS coated GO showed ~90% cell viability whereas GO without FBS coating showed only ~50% cell viability. TEM analysis showed irreversible cell membrane damage after 2 h of exposure to GO. FBS coated GO did not induce any membrane damage. These results suggested that cytotoxicity of GO is a result of direct physical interactions with cell membrane that can be mitigated by coating GO with FBS.

Mu et al. investigated the cellular uptake of bovine serum albumin (BSA) coated GO (flake size ~500 nm or ~1 μm) by mouse mesenchymal progenitor C2C12 cells [92]. Results showed that small GO (~500 nm) are internalized by clathrin-mediated endocytosis whereas large GO (~1 μm) are internalized by phagocytosis. Large GO sheets translocate into the reticuloendothelial system and small GO sheets are accumulated in various organelles.

Mbeh et al. have reported the cytotoxicity of albumin functionalized GONRs against A549 cells evaluated using Trypan blue and apoptosis (hoechst and propidium iodide staining) [93]. A dose-dependent cytotoxicity was observed wherein albumin functionalized GONRs at concentrations <50 μg/ml did not exhibit significant cytotoxicity, whereas incubation of A549 cells with higher concentrations (100 μg/ml) resulted in loss of cell proliferation and induction of apoptosis.

3. *In vivo* toxicology

A crucial step in the toxicological assessment of graphene-based formulations is their dose- and/or time-dependent safety pharmacological assessment in small and large animal models under various modes of administration (e.g. intravenous, intraperitoneal, oral). Table 2 summarizes the *in vivo* toxicological studies of graphene-based formulations.

3.1. Intravenous administration

Intravenous (IV) administration is a widely employed method wherein a needle is inserted into the vein and formulation is administered through that needle. It is the preferred mode of systemically introducing pharmaceutical formulations for imaging, drug delivery or therapy. Singh et al. investigated the *in vivo* platelet aggregation of GO and rGO nanosheets. GO and rGO sheets were administered intravenously via tail vein injection to Swiss male mice (8–12 weeks old) at 250 μg/kg dose for 15 min [86]. A collagen-epinephrine mixture was administered as positive control whereas saline was used as the negative control. After 15 min post injection, the mice were euthanized and lungs were harvested for histological analysis. Hematoxylin and eosin (H&E) staining showed ~48% thromboembolism whereas the collagen–epinephrine control solution resulted in ~64% occlusion of blood vessels. rGO was not as effective as GO towards platelet activation; rGO administration resulted in ~8% blood vessel blockage, significantly less than GO. These results showed that GO induces severe pulmonary thromboembolism that may be attributed to the greater surface charge density of graphene surface upon oxidation. In a follow-up study, Singh et al. investigated the *in vivo* thrombogenic properties of amine-modified GO (NH_2-GO) [94]. Compared to GO which induces platelet aggregation, NH_2-GO does not elicit any stimulatory effects on platelets or pulmonary thromboembolism. H&E staining revealed that GO resulted in ~46% blockage of pulmonary blood vessels while NH_2-GO showed no signs of obstruction.

Sasidharan et al. reported the long term *in vivo* toxicology of pristine and functionalized few layered graphene (FLG), FLG-COOH and FLG-PEG (Fig. 9A) administered intravenously to Swiss albino mice at 20 mg/kg for 1, 8, 30, and 90 days [95]. Sterile physiological saline was administered to control animals. All animals survived over the course of 90 days, however, the body weight of FLG, FLG-COOH and FLG-PEG treated mice was lower on days 60–90 compared to control mice. To dynamically track the *in vivo* biodistribution, ^{99m}Tc labeled FLG-COOH and FLG-PEG were injected and whole body images were captured at 0.1, 1, 3, 12, and 24 h (Fig. 9B). ^{99m}Tc-FLG-COOH showed accumulation and retention in lungs over 24 h. However, after 12 h, ^{99m}Tc-FLG-PEG was redistributed to RES system such as spleen and liver. FLG-COOH accumulated in the lungs resulting in thicker alveolar walls. Injection of FLG and FLG-COOH resulted in extensive spleen damage including the loss of dividing line between red pulp and marginal zone, abundance of megakaryocytes in the red pulp 90 days post injection, and lack of lymphocytes in the white pulp. On the contrary, FLG-PEG did not result in any injury to the marginal zone and only several black spots in the red pulp were observed. Liver tissue analysis revealed that FLG and FLG-COOH induced liver tissue degeneration while FLG-PEG did not and was observed as black spots. However, kidney necrosis was observed upon administration of both FLG and FLG-COOH as early as the first day of administration. FLG-PEG was noted as black spots on the tissue but did not exhibit any signs of necrosis. FLG, FLG-COOH, and FLG-PEG did not damage brain, heart, or testis suggesting that graphene cannot pass through the blood–brain barrier.

Zhang et al. have reported the toxicity of dextran functionalized graphene oxide (GO-Dex) intravenously administered via tail vein injection to female Balb/c mice at 20 mg/kg dose for 1, 3, and 7 days [96]. H&E staining of liver sections showed a significant increase in black spots – areas of GO aggregation – after 7 days indicating clearance of GO-Dex from mouse liver. For biodistribution and pharmacokinetic studies, ^{125}I labeled GO-Dex (^{125}I-GO-Dex) was injected via tail vein at 4 mg/kg concentration and blood was collected after 4, 24, 72, and 168 h. After 4 h of administration, ^{125}I-GO-Dex was found in liver, spleen, stomach, lungs, kidney, and intestine. At later time points, ^{125}I-GO-Dex was predominantly found in the liver and spleen. Histological sections of liver and kidney confirmed the presence of ^{125}I-GO-Dex as black dots that were abundant at day 1 and decreased at later time points suggesting the excretion of ^{125}I-GO-Dex via renal and fecal pathways. Since GO-Dex has a wide size distribution, small GO-Dex sheets could pass through glomerulus for renal excretion and large GO-Dex sheets accumulated in RES organs could be excreted out in feces via biliary pathway.

Zhang et al. have reported the distribution and biocompatibility of GO after intravenous administration to male Sprague Dawley rats at 1 and 10 mg/kg dose [97]. Histopathological analysis of lung, liver, spleen

Table 2
In vivo toxicity of graphene.

Material	Characterization	Properties	Animal model	Dose, route and duration	Conclusion	References
Intravenous administration						
GO, rGO	HR-TEM, zeta-potential, UV–Vis NIR spectroscopy, flow cytometry and fluorescence spectroscopy	GO: size = 0.2–5 μm, bilayer GO sheets with intersheet distance of 0.40 ± 0.02 nm. FFT diffraction pattern confirms single and bi-layer GO. FTIR peak at 1735 cm^{-1} confirming C═O groups. rGO: size = 0.2–5 μm, UV Vis: red shift to 260 nm. FTIR confirms removal of oxygenated functional groups.	Swiss male mice (8–12 weeks old)	Intravenous administration. 250 μg/kg dose injected via tail vein. Lungs collected for histological analysis (H&E staining) after 15 min.	GO: thrombotoxicity, pulmonary embolism and human platelet aggregation observed. Nearly 48% lung vessels totally or partially obstructed by platelet thrombosis. rGO: limited platelet aggression and reduced thromboembolism compared to GO. rGO induce ~8% total or partial obstruction of lung blood vessels.	Singh et al. [86]
Amine Graphene Oxide (NH_2-GO)	HR-TEM, FTIR, Raman spectroscopy, zeta-potential, UV–Vis NIR spectroscopy, flow cytometry	Sheet size: 2 μm, FTIR peaks: 950 cm^{-1}, 1250 cm^{-1}, 1573 cm^{-1}; Raman spectroscopy: G band = 1580 cm^{-1}, D band = 1350 cm^{-1}. High absorbance in visible and NIR region. No detectable fluorescence properties.	Swiss male mice (8–12 weeks old)	Intravenous administration. 250 μg/kg dose injected via tail vein. Lungs collected for histological analysis (H&E staining) after 15 min.	NH_2-GO: no thrombotoxicity. Blood vessels appear normal with no indication of occlusive pathology	Singh et al. [94]
FLG, FLG-COOH, FLG-PEG, ^{99m}Tc-FLG-COOH, ^{99m}Tc-FLG-PEG	HR-TEM, AFM, Raman spectroscopy, FTIR, BET	Graphene sheets with 2–4 layers; size: 128 ± 37.6 nm; thickness: 0.7 ± 0.31 nm; Raman peaks at 1325 cm^{-1}, 1575 cm^{-1}, and 2640 cm^{-1} corresponding to D, G, and 2D bands, respectively; BET surface area = 210–650 m^2/g. FTIR peaks at 3400 cm^{-1}, 1715 cm^{-1}	Swiss albino mice (4–5 weeks old)	Intravenous administration. A single dose of 20 mg/kg injected via tail vein. Brain, kidney, lungs, liver, spleen, intestine, heart and testis were collected after 1, 8, 30, and 90 days.	Mice survived after 90 days of graphene administration. Body weight of mice on days 60, 70, 80, and 90 were significantly lower than untreated mice.	Sasidharan et al. [95]
GO-Dex, ^{125}I-GO-Dex	AFM, FTIR, TGA, UV–Vis	Size: 50–100 nm; thickness: 2.8 nm; UV–VIS absorbance peak at 230–240 nm	Female Balb/c mice	Intravenous administration. 20 mg/kg GO-Dex injected into tail vein. Major organs collected for histology after 1, 3 and 7 days post injection. ^{125}I-GO-Dex injected at a dose of 4 mg/kg. Blood collected for pharmacokinetics and biodistribution study at 4, 24, 72, and 168 h post injection.	No short-term toxicity, excretion via renal and fecal pathways.	Zhang et al. [96]
GO, ^{188}Re-GO	AFM, Raman spectroscopy, zeta potential	Size: 100–800 nm; thickness: 1 nm; single layered sheets; zeta potential = −29.87 (GO), −20.47 (^{188}Re-GO)	Kun Ming mice (Sprague–Dawley rats, 6–8 weeks old)	Intravenous administration. GO: 1 and 10 mg/kg dose. Histopathological analysis of lung, liver, spleen and kidneys performed after 14 days post injection. ^{188}Re-GO: 200 μl (50 μCi) dose. Biodistribution measured after 1, 3, 6, 12, 24, and 48 h post injection.	Dose dependent toxicity. No significant pathological changes were observed after day 1 whereas inflammation, cell infiltration, pulmonary edema and granuloma formation were observed after 14 days. GO exhibits high blood half life (5.3 ± 1.2 h) and low RES uptake. Maximum uptake was observed in lungs.	Zhang et al. [97]
GO	AFM, TEM, FTIR	Monolayer sheet; Thickness: 1 nm; FTIR peaks at 3395 cm^{-1} (O–H), 1726 cm^{-1} (C═O), 1426 cm^{-1} (O–H), 1226 cm^{-1} (C–O), 1052 cm^{-1} (C–O)	Female Kunming mice (Sprague–Dawley rats, 4–5 weeks old)	Intravenous administration. Doses: 0 mg, 0.1 mg, 0.25 mg and 0.4 mg per mouse injected via tail vein. Histology and biodistribution analysis performed after 1, 7, and 30 days post injection.	No toxicity observed upto 0.25 mg dose. Chronic toxicity observed for 0.4 mg dose with 4/9 mice death. Long-term accumulation observed in liver, kidneys and spleen along with granuloma formation in lungs. No accumulation in brain — GO cannot pass blood brain barrier.	Wang et al. [98]
GO, ^{125}I-GO	AFM, TEM, Raman spectroscopy, infrared spectroscopy, particle size distribution, zeta potential, DLS	Size: large GO = 1–5 μm, small GO = 110–500 nm; thickness: 0.9 nm (single layer); D_h for large GO = 914 nm, D_h for small GO = 243 nm.	Male ICR mice	Intravenous administration. Single dose of 1–10 mg/kg administered via tail vein injection for biodistribution and pharmacokinetics studies. Tissue samples collected after 2–180 min post injection. For ultrastructural observation, 10 mg/kg dose was administered and lungs and liver collected 10 min post injection.	GO elimination from blood was observed. Large GO sheets accumulated in lungs and small GO accumulated in liver. Small GO has a longer blood half-life than large GO.	Liu et al. [99]

(continued on next page)

Table 2 (*continued*)

Material	Characterization	Properties	Animal model	Dose, route and duration	Conclusion	References
NanoGraphene Sheets functionalized with polyethylene glycol (NGS-PEG)	AFM, FTIR, UV–Vis, NIR fluorescence	Size: 10–50 nm; single or bi-layered sheets; FTIR peaks at 2800 cm^{-1} (C–H) and 1100–1500 cm^{-1} (C–O)	Tumor bearing Balb/c mice	Intravenous administration. Single dose of 20 mg/kg. Organs harvested after 1, 6, and 24 h post injection.	High tumor build up, no sign of abnormalities on the kidney, spleen, heart, liver and lung. Gradual elimination. Low uptake by RES. Photothermal therapy resulted in disappearance of tumor after 1-day treatment and an increase in the longevity of mouse by at least 24 days.	Yang et al. [100]
NanoGraphene Sheets functionalized with polyethylene glycol (NGS-PEG), ^{125}I-NGS-PEG	AFM, FTIR, XPS	Size: 10–30 nm; single or bi-layered GO sheets; FTIR peaks at 2800 cm^{-1} (C–H) and 1100–1500 cm^{-1} (C–O)	Balb/c mice	Intravenous administration. Pharmacokinetics study: Mice injected with 4-mg/kg doses of ^{125}I-NGS-PEG and blood drawn between 0 and 25 h. Biodistribution study: 4 mg/kg dose injected then sacrificed at 1 h, 6 h, 1 d, 3 d, 7 d, 15 d, 30 d, 60 d. Blood biochemistry/hematology study: injected intravenously 20 mg/kg sacrificed at 3, 7, 20, 40, and 90 days.	NGS-PEG mainly accumulates in the reticuloendothelial system and can be gradually cleared by renal and fecal excretion.	Yang et al. [101]
GNP-Dex	TEM, AFM	Disk shaped; diameter: 100 nm; thickness: 3 nm	Wistar rats	Intravenous administration. Dose: 1, 50, and 100 mg/kg 3 times a week for 3 weeks. Heart, liver, kidney and brain harvested for histology.	1 mg/kg and 50 mg/kg doses show no sign of toxicity. All vital parameters such as body weight, blood pressure, breathing and heart rate were normal. Two out of 8 animals died for 100 mg/kg dose after 2 weeks.	Kanakia et al. [102]
GNP-Dex	AFM	Diameter range: 60–100 nm. Thickness: 2–4 nm. Soluble in water up to 100 mg/ml	Male hamsters	Hamsters' left cheek pouch was exteriorized, pinned across a Lucite pedestal, and cleared of connective tissue. GNP-Dex was micropipetted at dosages of 0, 0.1, 0.5, 2.6, 10, 50 mg/ml at 30 s exposure and 5-min washout between dosages.	GNP-Dex showed no signs of arteriole dilation upto concentrations of 50 mg/ml.	Chowdhury et al. [88]
GNP-Dex	TEM, AFM	Disk shaped; diameter: 100 nm; thickness: 3 nm	Wistar male rats	Intravenous administration. Single doses of 1, 25, 50, 125, 250 and 500 mg/kg were injected via tail vein. Organs were harvested 1 and 30 days post injection of GNP-Dex for biodistribution and histopathological analysis.	Maximum tolerable dosage is between 50 mg/kg and 125 mg/kg. No changes in brain, neither cardiovascular, nor hematological factors at dosages less than 125 mg/kg.	Kanakia et al. [103]
GO, GO-NH_2, GO-DOTA, ^{111}In-DOTA-GO	TEM, AFM, FTIR, XPS, TGA, Raman spectroscopy	Size: 50–2000 nm; single or bilayered GO sheets, FTIR peaks at 3400 cm^{-1} (OH), 1729 cm^{-1} (C═O), 1624 cm^{-1} (H–O–H), 1374 cm^{-1} (O–H), 1225 cm^{-1} (C–O–C); $I_D/I_G = 1.34$ (GO-DOTA), 1.21 (GO), 0.31 (graphite)	C57BL/6 mice (6–8 weeks)	Intravenous administration. A dose of 200 μl of ^{111}In-GO-DOTA (5–6 MBq) was injected via tail vein (t = 1, 4, 24 h) for SPECT/CT study. For biodistribution study, animals were injected with 1–2 MBq equivalent dose for 1, 4, and 24 h.	Maximum accumulation was observed in liver and spleen, however, GO translocation from liver to spleen was also observed. No biliary excretion or metabolism by hepatocytes was observed. GO was eliminated via urine. These results suggest that chemical functionalization of GO sheets can alter their biodistribution.	Jasim et al. [104]
Intraperitoneal administration						
^{125}I labeled GO, nGO-PEG, RGO-PEG and nRGO-PEG	AFM	Size: diameters of GO, nGO-PEG, RGO-PEG and nRGO-PEG are 450, 25, 50 and 27 nm, respectively. Average thickness of GO, GO-PEG, RGO-PEG, and nRGO-PEG are 0.94, 1.22, 4.43 and 5.66 nm, respectively.	Female Balb/c mice	Intraperitoneal administration: 80 mice were intraperitoneally injected with GO, nGO-PEG, RGO-PEG, and nRGO-PEG at 50 mg/kg (20 μCi) and euthanized 1, 7, 30, and 90 days post administration. Oral administration: 15 mice were orally injected with nGO-PEG at 100 mg/kg dose and euthanized at 1, 7, and 30 days post injection. Blood was collected for serum biochemistry and blood panel analysis. All major organs were collected for histology and biodistribution.	High accumulation in liver and spleen after intraperitoneal administration. No accumulation was observed after oral administration. PEG GO derivatives were phagocytized in the RES system in a size and surface coating dependent manner. Despite long-term retention, no toxicity was observed in blood analysis, serum biochemistry and histology analysis. Toxicity and biodistribution of graphene is dependent on size, surface coatings and route of administration.	Yang et al. [105]

Table 2 (*continued*)

Material	Characterization	Properties	Animal model	Dose, route and duration	Conclusion	References
cGO and pGO (highly pure GO)	TEM, AFM, FTIR, Raman spectroscopy, UV–Vis	Size: cGO: > 0.1 μm^2, pGO: 0.01–0.02 μm^2; Thickness ~ 1 nm. UV absorbance peak at 230 nm. Raman spectroscopy: D Band = 1350 cm^{-1}, G Band = 1590 cm^{-1}	C57BL/6 mice (6–8 weeks old)	Intraperitoneal administration: dose 50 μg in 0.5 ml saline. Animals euthanized 24 h and 7 days post administration and assessment of inflammatory reactions, protein levels in peritoneal lavage and histology of diaphragm was performed.	Highly purified single layered GO sheets show no signs of inflammation or granuloma formation upto 50-μg/animal dose administered intraperitoneally.	Ali-Boucetta et al. [106]
GO-pluronic hydrogel	TEM, SEM, rheology	Size: 100–500 nm. Gelation at pH = 7, absorbs IR light	Female Balb/c mice (6–7 weeks old)	Intraperitoneal administration. Gel composition: 0.4% GO-0.25–1% pluronic. GO-pluronic gel implanted in subcutaneous cavity of mice. After 3 and 8 weeks post implantation, dermal tissue was analyzed by histology.	No toxicity was observed. Mild inflammation observed after 3 weeks of implantation. After 8 weeks, the number of macrophages reduced. No tissue necrosis, acute inflammation or tissue hemorrhaging was observed suggesting a good biocompatibility of GO-pluronic gels.	Sahu et al. [107]
GO, graphite, nanodiamonds (ND)	TEM, Zeta potential	Size: 8–25 nm (GO), 3–4 nm (graphite and ND); zeta potential: −83.8 ± 0.25 mV (GO), 12.5 ± 0.43 (graphite), −15.8 ± 0.55 mV (ND)	Female Wistar rats (6 weeks old)	Intraperitoneal administration: 40 mice were injected with a dose of 4 mg/kg administered for 4 or 12 weeks at 3-day intervals. Liver and blood collected post euthanasia for analysis of blood serum biochemical indices, blood morphology and liver physiology.	No toxicity was observed. Blood biochemical indices and liver enzymes were within physiological range. Large aggregates of nanomaterials were observed at the injection site, smaller aggregates were observed in liver serosa and mesentery.	Strojny et al. [108]
Oral administration						
GO	TEM, AFM, XRD, FTIR, XPS, UV–Vis and Raman spectroscopy	Size: 0.2 μm; thickness = 1.8 nm; XRD peaks at 12° and 43°; UV–Vis peaks at 232 nm and 280 nm; FTIR peaks at 1715 cm^{-1} (C═O), 1120 cm^{-1} (C–O–C), 3400 and 1620 cm^{-1} (O–H); XPS — C:O molar ratio 2:11, C1s peaks at 285 eV (C═C), 286.1 eV (C–O), 287.5 eV (C═O), 288.5 eV (C═O); Raman peaks at 1355 cm^{-1} (D band), 1588 cm^{-1} (G band) and 2680 cm^{-1} (2D band).	Female ICR mice (6–8 weeks old)	Oral administration. Dose: 0.5 and 0.05 mg/ml. GO mixed with drinking water. Days 1–38 for maternal mice and 1–21 for filial mice. After 21 and 38 days, blood was collected for biochemistry analysis and organs were harvested for H&E staining.	Decrease in body weight, body length and tail length for high concentration group. No significant differences in blood biochemistry. Pathological examination shows severe atrophy of all major organs. H&E staining of intestine showed increased villi and duodenum width. Results show that GO is toxic to developmental offsprings in mice.	Fu et al. [109]
^{125}I-rGO	TEM, particle size distribution	Size: small GO (~100 nm), large GO (~450 nm)	Male C57b/6 mice (6–8 weeks old)	Oral administration. Dose 60 mg/kg, administered via oral gavage every 24 h for 5 days.	Initial decrease neuromuscular coordination and locomotor activity, which were restored to normal levels at later time points (15 and 60 days post administration). No significant differences in blood biochemistry, liver function, kidney function, blood enzyme levels, learning, memory, anxiety, and spatial and exploratory behaviors. rGO administered via oral administration is non-toxic.	Zhang et al. [110]
GO	TEM, AFM, FTIR, Raman spectroscopy and particle size tracking	Size: 72 ± 11 nm; thickness: 1 nm, FTIR peaks: 3425 cm^{-1} (O–H), 1749 cm^{-1} (C═O), 1630 cm^{-1} (C═O), 1130 cm^{-1} (C–O). Raman peaks at 1377 cm^{-1} (D band) and 1609 cm^{-1} (G band); zeta potential = −20.2 mV.	*Caenorhabditis elegans*	Oral administration. GO mixed with food (K medium) at 0.1–100 mg/l. Acute exposure (24 h) and prolonged exposure (larvae to adult). Lethality, growth, reproduction and locomotion behavior was analyzed.	Prolonged exposure to 0.5–100 mg/l of GO caused damage in primary (intestine) and secondary (neurons and reproductive) organs. GO translocated into intestinal wall due to loss of villi and were distributed surrounding mitochondria. Additional observations were increased mean defecation cycle length and hyper-permeable state of intestinal barrier. Results suggest that GO exposure to environmental organisms is toxic.	Wu et al. [111]

(*continued on next page*)

Table 2 (*continued*)

Material	Characterization	Properties	Animal model	Dose, route and duration	Conclusion	References
Pulmonary administration						
GNPs	SEM, EPR, BET, density measurement, aerodynamic diameter, ICP-MS	Size: diameter = 5.64 ± 4.56 nm, layers = 1–10; surface area = ~100 m^2/g; density = ~2; EPR = 867.3 ± 77.5 a.u.	Female C57BL/6 mice (9 weeks old)	Pharyngeal administration. Dose — 50 μg/mouse. Mice sacrificed after 24 h and 1-week post exposure. BAL fluid was extracted. Intrapleural injection: dose — 5 μg/mouse. Mice sacrificed after 24 h and 7 days. Pleural space was lavaged and the surrounding tissue was excised for histology.	GNPs upto 25 μm are respirable and deposit beyond ciliary airways post inhalation. GNPs induced inflammation in lung and pleural space with an increase in the levels of MIP-1α, MCP-1, MIP-2, IL-8 and IL-1β. SEM images revealed signs of frustrated phagocytosis. Inflammatory response decreased one-week post exposure.	Schinwald et al. [112]
Graphene (aggregated in water), graphene (2% pluronic), GO	AFM, XPS, Raman spectroscopy, optical absorbance	Optical absorbance: 600 nm; size: 40,000 nm^2 (graphene), 200,000 nm^2 (GO); thickness: 1.2–5 nm (graphene), 0.5–2 nm (GO)	Male C56BL/6 mice (8–12 weeks old)	Pulmonary administration. Dose — 50 μg/mouse administered via intratracheal instillation. GO is injected directly into the lungs. Lung assessment post 24 h using histology and electron microscopy	Inflammation, apoptosis, increase of mitochondrial respiration and pulmonary inflammation were observed.	Duch et al. [113]
^{125}I-GO	TEM, SEM, AFM, FTIR, Raman spectroscopy	Size: 10–800 nm; thickness: 1 nm; FTIR peaks at 1731 cm^{-1} (O–H), 1628 cm^{-1} (C═C), 1078 cm^{-1} (C–O); Raman peaks: 1333 cm^{-1} (D band), 1594 cm^{-1} (G band).	Male Kunming mice (biodistribution) and male C57BL/6 mice (pulmonary toxicity)	Pulmonary administration. Dose: 1, 5, 10 mg/kg for dose dependent acute and chronic pulmonary toxicity assessed after 24 h. 10 mg/kg for time dependent toxicity assessed after 0, 24, 48, 72 h and 1 week. 10 mg/kg for long-term chronic toxicity assessed after 1 and 3 months. Biodistribution evaluated by SPECT imaging, pulmonary toxicity by histology and cell injury, lung edema and neutrophil infiltration assays.	Acute lung injury, thickening of alveolar septa, increased neutrophil counts and oxidative damage were observed. GO can pass through air–blood barrier albeit in smaller amounts and care must be taken to ensure minimal exposure by inhalation during large-scale production of GO.	Li et al. [114]
Intravitreal administration						
GO	AFM, FTIR, Raman spectroscopy	Size: 50–500 nm; thickness: 1 nm; FTIR peaks at 3430 cm^{-1}, 1720 cm^{-1}, and 1000 cm^{-1}; Raman spectroscopy: D band at 1370 cm^{-1}, G band at 1590 cm^{-1}. I_D/I_G = 0.75	Japanese white rabbits (2–3 kg)	Intravitreal administration. Dose: 0.1, 0.2, or 0.3 mg. Eye function was measured using electroretinography (ERG) after 2, 7, 28 and 49 days post injection. After 49 days, animals were euthanized and eyes were collected for histological examination. Balanced saline solution was used as the controls.	No significant differences in ERG amplitudes compared to controls. H&E staining showed small amounts of GO residue, however, no retinal abnormality was observed.	Yan et al. [115]

and kidneys performed 14 days post injection shows no pathological changes for all organs examined for 1 mg/kg dose. For 10 mg/kg treatment, all organs except lung showed normal pathophysiology. However, due to high accumulation and slow clearance, GO accumulated in lungs resulted in pulmonary edema, granulomatous lesions, inflammatory cell infiltration, and fibrosis. These results suggest that GO is biocompatible, however, accumulation in lungs at higher concentration may lead to safety concerns. Biodistribution of GO was assessed by tracking intravenously administered ^{188}Re labeled GO (^{188}Re-GO) after 1, 3, 6, 12, 24, and 48 h. It was observed that GO cleared from blood, accumulated in lungs, liver and spleen and was up taken by mononuclear phagocytes in the reticuloendothelial system.

Wang et al. reported the biocompatibility of GO administered via tail vein injections to 4–5 week old female kunming mice (Sprague Dawley rats) at 0, 0.1 mg (low), 0.25 mg (medium), and 0.4 mg (high) doses [98]. No toxicity was observed for low and medium doses. However, for high dose, 4 out of 9 mice died after 1 week due to airway blockage caused by accumulation of GO. Histology analysis after 1, 7, and 30 days shows long-term accumulation of graphene in liver, kidney and spleen. Granuloma formation along with the presence of neutrophils and foamy alveolar macrophages was observed in lungs suggesting a foreign body immune response. No accumulation was observed in brain suggesting that GO cannot pass the blood brain barrier. These results suggest that GO is non-toxic at low concentrations and results in irreversible airway damage and chronic pulmonary toxicity at high concentrations.

Liu et al. reported the dose- and size-dependent toxicity and biodistribution of GO sheets [99]. Male ICR mice were intravenously injected with small and large GO sheets (s-GO and l-GO) labeled with ^{125}I to enable radioactive tracking of tissue biodistribution, organ accumulation and blood clearance of GO after 2–180 min post injection at 1–10 mg/kg doses. It was observed that s-GO mainly accumulated in the liver with some aggregates present in lungs and spleen, however, after 180 min, clearance of s-GO was observed with a residual accumulation of ~11% in liver and <1% in lungs. On the contrary, in comparison to s-GO, l-GO showed higher accumulation in lungs with a residual accumulation of ~19% after 180 min. TEM analysis of lung sections show intracellular accumulation of s-GO in phagocytic cells while l-GO particles (bigger than 1 μm) was lodged in cell gaps of lungs. The size-regulated biodistribution of s-GO and l-GO was attributed to the different aggregation states of the nanoparticles. The less dispersed GO resulted in the formation of larger GO-protein complexes, which were filtered by the pulmonary blood vessels. At higher doses, s-GO aggregated to

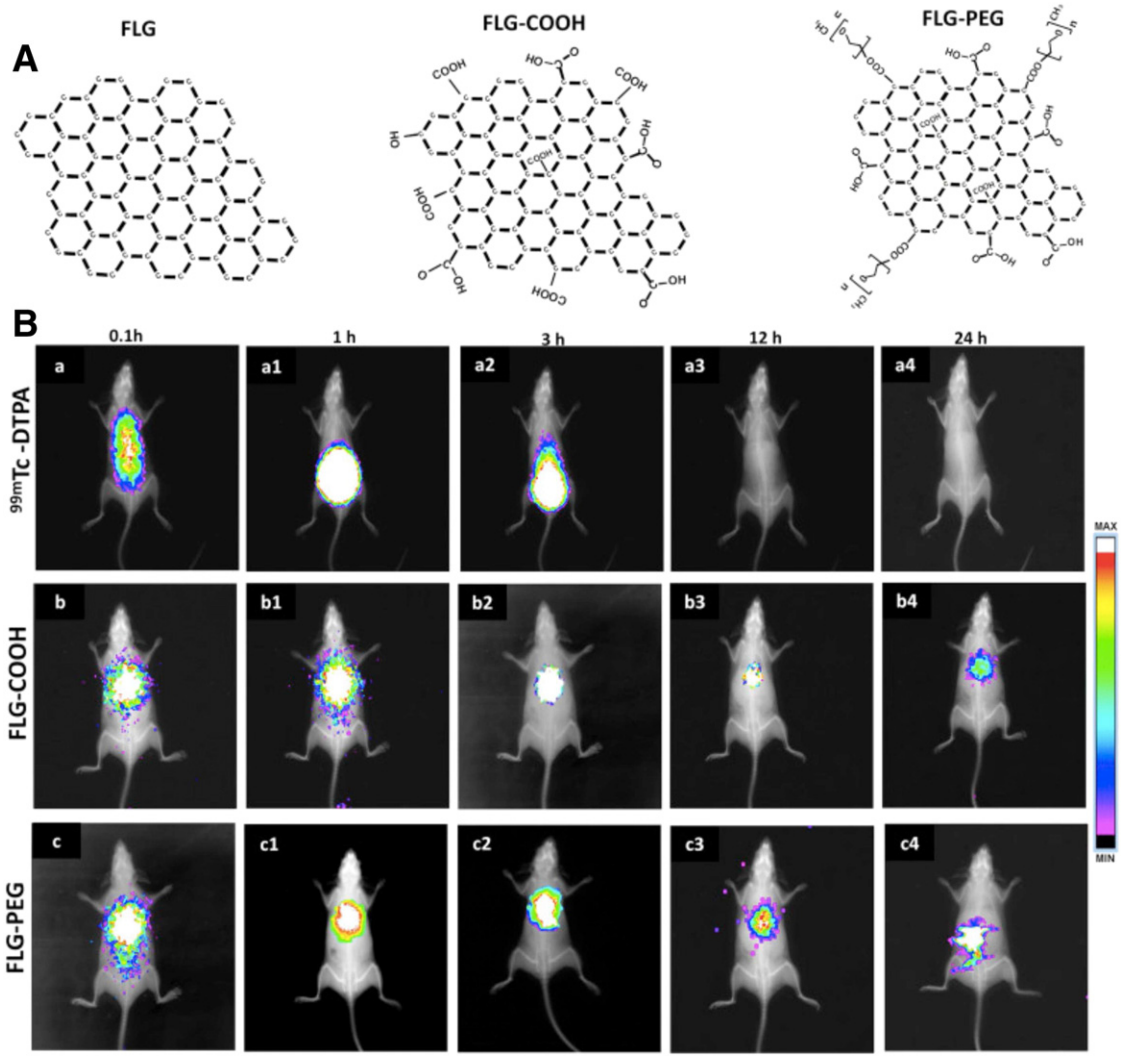

Fig. 9. (A) Schematic illustrating structural depiction of few layered graphene (FLG), FLG-COOH and FLG-PEG. (B) Real time *in vivo* biodistribution of ^{99}Tc labeled FLG, FLG-COOH, FLG-PEG, signal accrued for 24 h.
Adapted from Reference [95] with permission, copyright © Elsevier, 2015.

large particulates resulting in the entrapment in lungs. The blood half-life of s-GO was 2.2 min ($T_{1/2}$ alpha) and 170 min ($T_{1/2}$ beta). For l-GO, $T_{1/2}$ alpha was 1.8 min and $T_{1/2}$ beta was 102 min. These results suggest that s-GO possesses longer blood retention time than l-GO.

Yang et al. reported *in vivo* biodistribution and photothermal activity of PEG functionalized nano graphene sheets (NGS-PEG) [100]. Cy7 dye labeled NGS-PEG was intravenously injected into tumor bearing Balb/C mice at a dose of 20 mg/kg and organs were harvested after 1, 6, and 24 h. Significant accumulation of NGS-PEG was observed in tumors purportly due to leaky vasculature along with low accumulation in RES organs. After 24 h post injection, the kidneys showed strong fluorescence (Fig. 10) attributed to the renal excretion of small sized NGS particles. NGS-PEG showed no toxicity — neither death nor significant weight loss was observed in all animals. After NGS-PEG administration, the tumors on the right shoulder of 4T1 Balb/c mice were exposed to 808 nm laser until the surface temperature reached ~50 °C. The tumors disappeared 1-day post laser treatment leaving a black scar that disappeared after one week. No tumor regrowth was observed after 40 days. These results suggest that PEG functionalized graphene can be suitable for *in vivo* photothermal therapy applications. In another study, Yang et al. have reported the long term *in vivo* biodistribution and pharmacokinetics of ^{125}I-labeled NGS-PEG intravenously administered in Balb/c mice at 4 mg/kg dose [101]. For pharmacokinetics study, blood was drawn after 0–25 h and measured by a gamma counter. To examine the biodistribution of ^{125}I-NGS-PEG, 4 mg/kg was administered intravenously and organs were harvested at various time points: 1 h–60 days post injection. NGS-PEG initially accumulated in several organs, however accumulation at later time points was observed in liver and spleen. H&E staining of liver and spleen sections showed a reducing number of NGS-PEG aggregates over time suggesting removal of NGS-PEG from RES system. Renal pathway cleared out smaller sized NGS-PEG (10 nm diameter) while larger NGS-PEG aggregates were excreted through biliary pathway into the feces. Blood biochemistry and hematology analysis showed normal levels of urea, blood cells, hemoglobin and other factors suggesting that there were no toxic effects of NGS-PEG to liver and kidneys. These results suggest that NGS-PEG does not exhibit long-term *in vivo* toxicity in mice.

Kanakia et al. reported the sub acute toxicity of dextran functionalized graphene nanoplatelets (GNP-Dex) administered via intravenous injections to Wistar rats at 1, 50, and 100 mg/kg doses 3 times a week for three weeks [102]. No signs of toxicity were observed for 1 mg/kg and 50 mg/kg doses. All vital parameters such as body weight, blood pressure, breathing and heart rate were normal. However, for 100 mg/kg dose, 2 out of 8 animals died after 2 weeks. A complete blood count analysis showed physiological levels of blood urea nitrogen and creatinine indicating normal kidney function. ALT and ALP levels

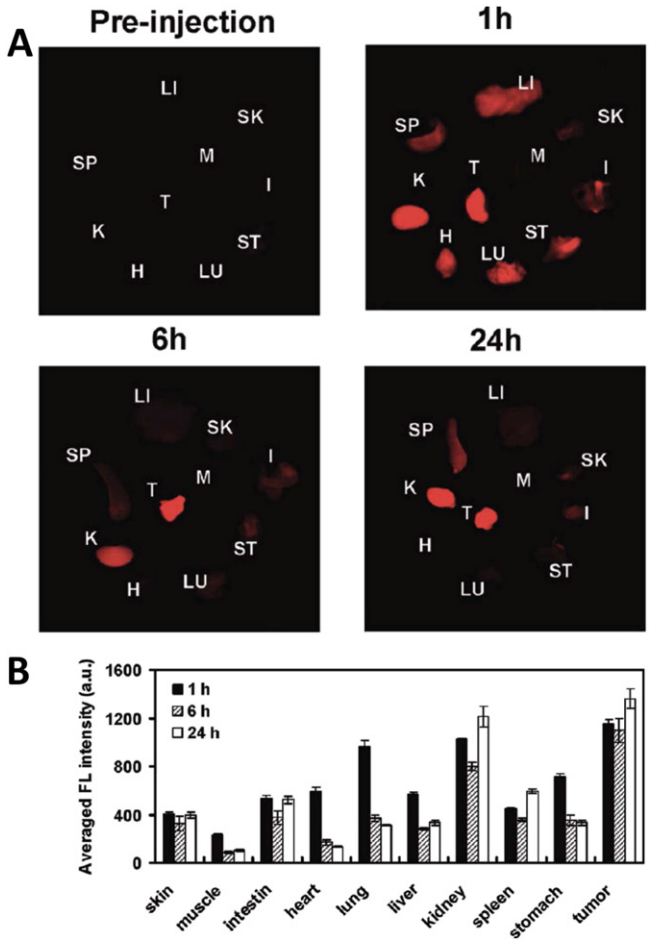

Fig. 10. Biodistribution analysis of Cy7 labeled PEG functionalized nano graphene sheets (NGS-PEG-Cy7). Tumor bearing 4T1 mice were sacrificed after 1, 6, and 24 h of NGS-PEG-Cy7 administration. (A) Spectrally resolved ex vivo fluorescence images of SK—skin, M—muscle, I—intestine, H—heart, LU—lung, LI—liver, K—kidney, SP—spleen, ST—stomach, and T—tumor. (B) Chart depicting semi quantitative biodistribution of each organ for n = 3 mice per group.
Adapted from Reference [100] with permission, copyright © American Chemical Society, 2010.

were elevated, however, blood glucose was normal. Histology analysis after 3 weeks showed the presence of GNP-Dex in hepatic Kupffer cells and pulmonary alveolar macrophages, which increased with increasing dose of GNP-Dex (Fig. 11). No adverse effects or inflammation were observed in brain, heart, spleen and kidney.

Mullick Chowdhury et al. reported the *in vivo* vasoactivity of GNP-Dex using male hamsters cheek pouch model [88]. GNP-Dex was administered at doses ranging from 1 to 50 mg/ml to the excised left cheek pouch tissue of hamsters using a micropipette. The arcade-terminal arteriolar network junction was the microvascular observation site. The baseline diameters of arcade and terminal arterioles were 23 μm and 8 μm, respectively. The administration of 0.1 mg/ml and 0.5 mg/ml GNP-Dex had no significant effect on the arteriole diameters. No significant differences in the dilation of arterioles were observed at higher doses of 10 mg/ml and 50 mg/ml. However, the administration of FDA-approved natural biopolymer dextran at 35 mg/ml resulted in ~23% dilation of arcade arterioles and ~63% dilation of terminal arterioles. The lack of dilation post GNP-Dex administration and an increased dilation due to dextran suggests that the observed minor vasoactive effects of GNP-Dex could be due to the dextran coating of GNPs.

In another study, Kanakia et al. have evaluated the acute toxicity and biodistribution of GNP-Dex administered via intravenous injections in male Wistar rats at doses between 1 and 500 mg/kg after 1 and 30 days [103]. The results show that the maximum tolerable dose (MTD) of GNP-Dex is between 50 and 125 mg/kg. Blood half-life of GNP-Dex is ~30 min. Maximum accumulation of GNP-Dex after day 1 was found in liver and kidney, which reduced (at least 2–4 folds) after 30 days of administration suggesting a clearance of GNP-Dex via RES system (Fig. 12A & B). ICP analysis showed that GNP-Dex administered at 50 mg/kg had a higher blood concentration than 500 mg/kg doses 30 min post-administration (Fig. 12C). Majority of GNP-Dex nanoparticles were excreted via feces (~60–90%) within 24 h (Fig. 12D), small amounts were excreted via urine (Fig. 12E). Histopathological changes (Fig. 12F–J) were observed in heart, lung, liver, kidney and spleen at high treatment concentrations (250 μg/ml). No adverse effects were observed in brain. Hematological factors and cardiovascular parameters remained at physiological levels upto 125 mg/ml treatment doses. These results suggest that GNP-Dex is non-toxic with a MTD of 125 mg/kg.

Jasim et al. reported the *in vivo* biodistribution of chemically functionalized graphene (GO-DOTA) labeled with ^{111}In after intravenous injections in C57BL/6 mice at 200 μl dosage [104]. Post 1, 2, and 24 h of administration, ^{111}In-DOTA-GO was accumulated in bladder and excreted via urine. No fecal elimination was observed. Maximum accumulation was observed in liver and spleen. Furthermore, at later time points, translocation of GO from liver to spleen was also observed. No organ damage was observed at all time points. The results suggested that chemically functionalized GO sheets are non-toxic and possess distinctly different physiological behavior (biodistribution and excretion characteristics) than pristine or non-covalently functionalized graphene sheets.

3.2. Intraperitoneal administration

Intraperitoneal (IP) administration is the injection of the formulation into the peritoneum (or body cavity). Yang et al. have reported the *in vivo* toxicity of PEG functionalized GO administered intraperitoneally and orally in female Balb/c mice [105]. PEG functionalized and ^{125}I labeled nano-graphene oxide (nGO-PEG), reduced graphene oxide (rGO-PEG), and nano reduced graphene oxide (nrGO-PEG) of diameters 25, 50, and 27 nm, respectively, were administered intraperitoneally at 50 mg/kg dose and orally at 100 mg/kg. Animals were euthanized post 1, 7, 30 and 90 days post intraperitoneal administration and 1, 7, and 30 days post oral injections. All major organs were collected for histology and biodistribution analysis and blood was collected from the orbital for complete blood panel and serum biochemistry analysis. The radioactivity of GO formulations after oral administration was undetectable after 1 week suggesting negligible uptake of PEGylated GO administered orally. However, after intraperitoneal administration, PEGylated GO showed high accumulation in RES organs (black colored liver and spleen) after 1 and 7 days. Larger sized RGO-PEG showed higher uptake (>2 fold, determined by radioactivity measurements) than smaller nGO-PEG and nrGO-PEG formulation. No animal death, body weight loss, inflammation, or significant changes in bloody panel or serum biochemistry were observed after 90 days post intraperitoneal administration indicating no signs of toxicity. The results suggested that PEGylated GO do not elicit any adverse effects under the above conditions in rodents, and the biodistribution and clearance profiles depend on the size, surface coating and route of administration.

Ali-Boucetta et al. have investigated the *in vivo* pathogenicity of highly pure, colloidally stable dispersions of GO [106]. Conventional GO (cGO, size >0.10 μm^2) prepared using Hummer's method was subjected to several purification steps to obtain highly pure GO (pGO, size 0.01 μm^2 to 0.02 μm^2). Both, cGO and pGO had similar chemical functional groups (carbonyls, hydroxyls and epoxides). pGO sheets were administered intraperitoneally at a dose of 50 μg/animal for 1 and 7 days. CNTs were used as positive controls. The inflammatory response was investigated by observing the change in protein levels and the change in the number of polymorphonuclear leucocytes 1 and 7 days post administration. After 1 day, pGO did not show a change in polymorphonuclear

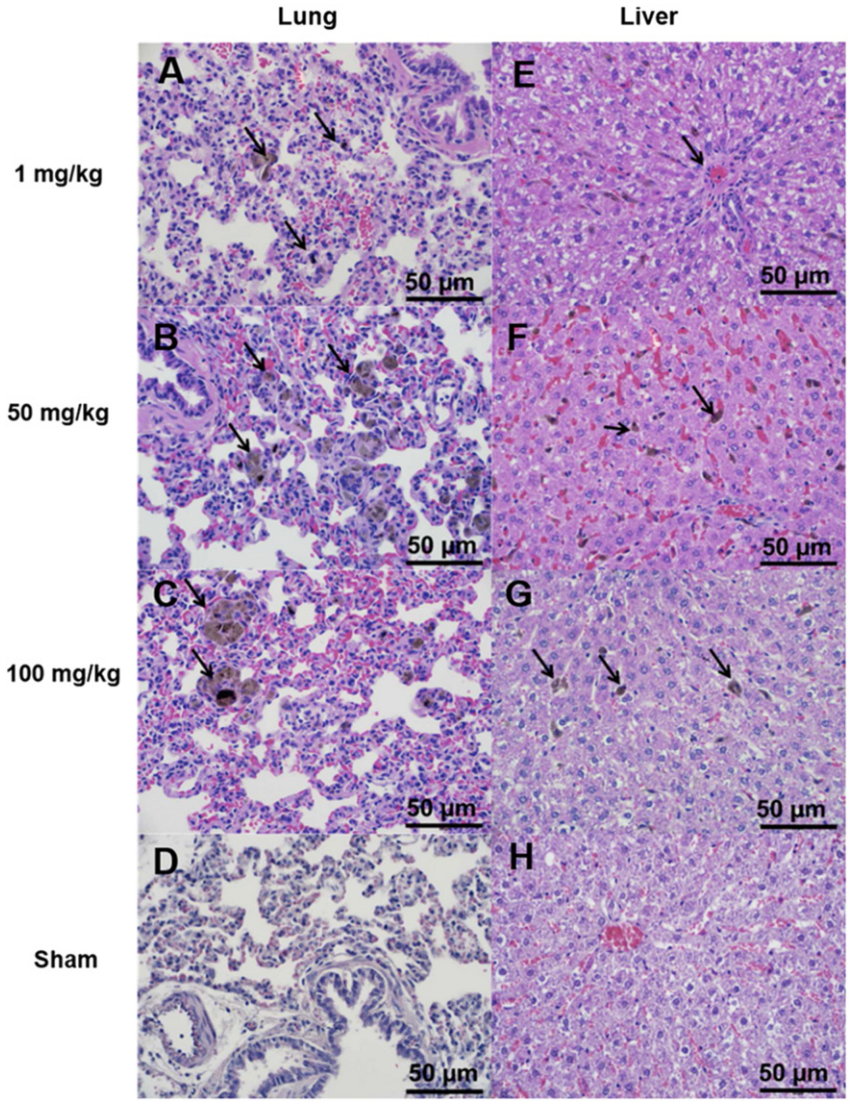

Fig. 11. Representative H&E staining of lung and liver sections post GNP-Dex administration at 1, 50, and 100 mg/kg in Wistar rats. Pigmentation (arrows, A–C) was observed within alveolar macrophages in lungs at all GNP-Dex administration concentrations indicating the presence of graphene nanoparticles. (D) Sham lungs showed no diagnostic abnormalities. Liver sections at 1 mg/kg (E) showed minimal at liver steatosis, at 50 mg/kg (F) showed pigmented macrophages in Kupffer cells indicating the presence of graphene. No signs of inflammation were observed. At 100 mg/kg dose (G), an increase in pigmentation was observed. (H) Sham liver sections showed no diagnostic abnormality.
Adapted from Reference [102] with permission, copyright © Kanakia et al. (open access, Nature Scientific Reports), 2015.

leucocyte (PMN) and protein levels whereas CNT controls induced at least 2-fold increase in total PMN count. After 7 days, there was accumulation of macrophages and giant cells with a deposition of collagen on the mesothelial membrane for CNT controls; pGO groups did not show any such effects. These results indicated that highly pure single layered GO sheets may not induce inflammation or granuloma formation upto 50 μg/animal dose administered intraperitoneally.

Sahu et al. investigated the *in vivo* biocompatibility of GO dispersed pluronic gels administered intraperitoneally via implantation in subcutaneous pockets in 6–7 weeks old Balb/c mice [107]. Mild inflammation was observed 3 weeks post implantation. After 8 weeks, the number of macrophages reduced and no chronic inflammation, tissue necrosis or hemorrhaging was observed. Furthermore, no gel degradation or degradation products were observed in the surrounding tissues.

Strojny et al. reported the intraperitoneal toxicity of GO, graphite and nanodiamonds administered to 6 weeks old female Wistar rats [108]. Nanoparticle suspensions were injected at a dose of 4 mg/kg for 4 or 12 weeks at three-day intervals. After 4 or 12 weeks, rats were euthanized and liver and blood were collected. Results show the presence of nanoparticle aggregates in the peritoneal cavity close to the injection site. Smaller aggregates were observed in the mesentery and liver serosa suggesting transportation and accumulation of nanoparticles in liver. No adverse health effects were observed for all nanoparticles (GO, graphite or nanodiamonds) at all time points (4 or 12 weeks). Blood analysis and liver enzyme levels were normal suggesting liver biocompatibility.

3.3. Oral administration

In oral administration, a formulation/substance is administered via mouth in cases where a systemic effect is desired. Fu et al. have investigated the development of mice offsprings after oral administration of graphene oxide at 0.5, and 0.05 mg/ml to maternal mice [109]. GO suspension in drinking water was administered to female ICR mice (8–9 weeks old) from 1 to 38 postnatal days (PND). Filial mice were administered GO water during the suckling period from 1 to 21 PND and normal water during the weaning period from 22 to 38 PND. After 21 and 38 days, pups were weighed and euthanized. Compared to the control groups that received normal water, significant decrease in body weight, body length and tail length of filial mice were observed for

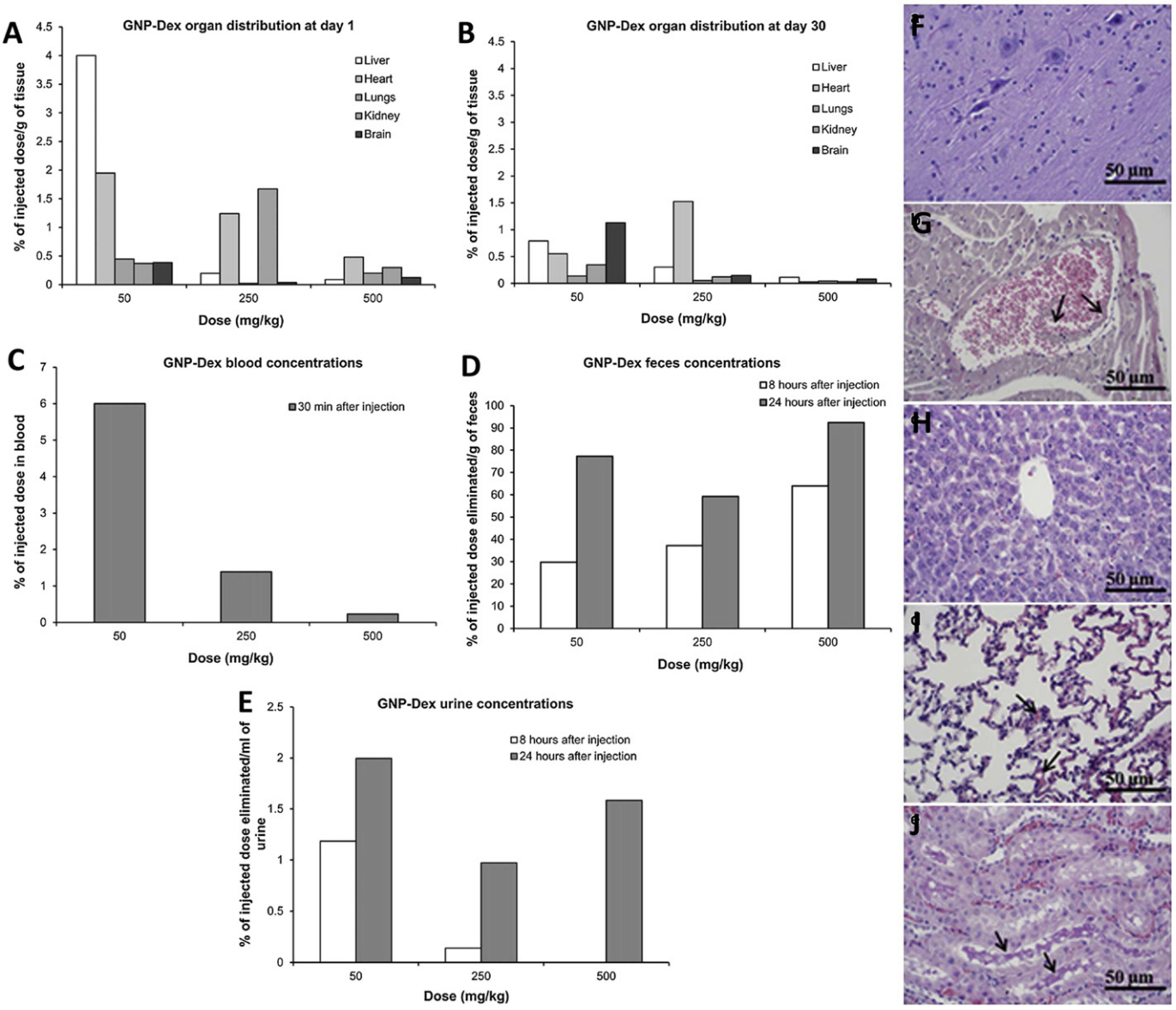

Fig. 12. (A & B) Tissue biodistribution, (C) blood half life, (D) elimination via feces and (E) urine after GNP-Dex administration at doses 50–500 mg/kg to Wistar rats analyzed via ICP-MS. Liver and kidney showed maximum uptake after 24 h of administration. Majority of GNP-Dex was excreted via feces; small amounts were cleared via urine. Histological sections of (F) cerebral cortex, (G) myocardium, (H) liver, (I) pulmonary parenchyma and (J) renal cortex after 24 h of GNP-Dex administration at 250 mg/kg dose. No diagnostic abnormalities were observed in cerebral cortex and liver. Vascular congestion of myocardium was observed. Arrows in (G) show dilated vein containing debris of GNP-Dex. Mild focal congestion was observed in the alveolar capillaries of pulmonary parenchyma. Vascular congestion and proteinaceous casts were observed in renal tubules of renal cortex.
Adapted from Reference [103] with permission, copyright © Elsevier, 2014.

0.5 mg/ml treatment group. Blood biochemistry analysis showed no significant differences in the levels of alanine aminotransferase (ALT), aspartate aminotransferase (AST), blood urea nitrogen (BUN) and creatinine (CREA) for both the GO groups. Pathological examination of heart, lung, spleen, kidney and liver of filial mice administered with 0.5 mg/ml GO suspension showed severe atrophy (Fig. 13A). H&E staining of duodenum, ileum, jejunum (parts of small intestine) showed increase in villi length and duodenum width post GO administration (Fig. 13B). These results show that GO can have significant negative effects on the development of filial mice during the lactation period.

Zhang et al. investigated the short-term and long-term effects of reduced GO (rGO) on general locomotor activity, neuromuscular coordination, balance, anxiety, learning and memory of male C57b/6 mice (6–8 weeks old) using rotarod, open field and Morris water maze tests [110]. HEPES buffer dispersed rGO were administered via oral gavage every 24 h for 5 days at 60 mg/kg dose. rGO treated mice maintained normal body weight, organ weight, and instinctive behaviors (eating, etc.) compared to control mice administered with chow and HEPES buffer. However, initial 3–4 days post treatment, mice showed decreased neuromuscular coordination and locomotor activity failing the rotarod and open field tests. At later time points (15 and 60 days post administration), all these parameters returned to their normal state. No significant differences in blood biochemistry, liver function and kidney function and aging parameters were observed. The morphologies of neurons in the hippocampus and neuroglia cells as well as choline acetyl transferase and hippocampal acetylcholine esterase (enzymes involved in memory and learning) levels also remained normal post rGO administration. These results show that exposure to high concentration of rGO sheets via oral administration results in a short term decrease in neuromuscular coordination and locomotor activity which return to normalcy a few days post exposure; it does not affect learning, memory, anxiety, spatial and exploratory behaviors.

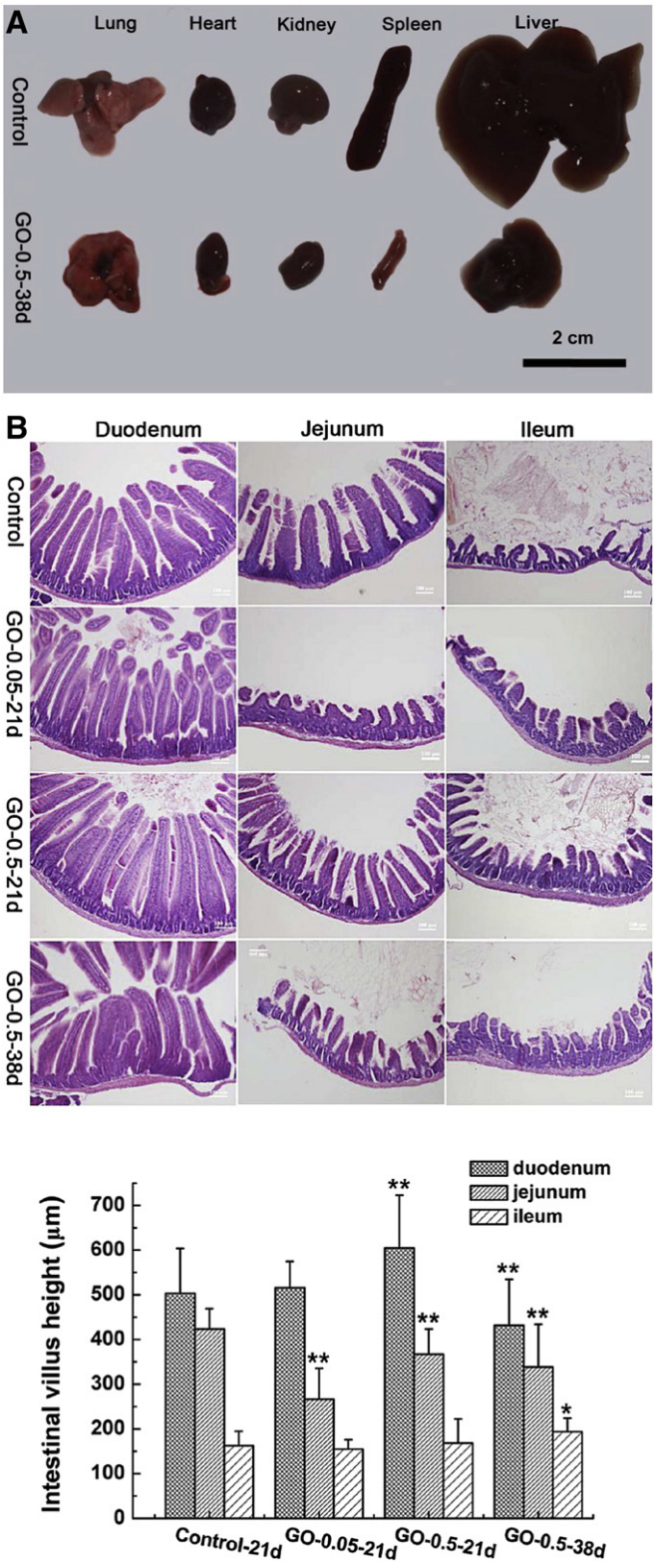

Fig. 13. (A) Pathological examination of lungs, heart, kidney, spleen and liver collected from control and GO administered mice (0.5 mg/ml) after 38 days showing severe atrophy of all major organs. (B) H&E staining of duodenum, jejunum and ileum of GO treated filial mice at 0.05 mg/ml for 21 days and 0.5 mg/ml for 21 and 38 days. The length, width and height of villi of GO administered groups were longer than control groups. Scale bars represent 100 μm.
Adapted from Reference [109] with permission, copyright © Elsevier, 2015.

Wu et al. investigated the toxicity of graphene oxide at doses between 0.1 and 100 mg/l administered orally on nematode *Caenorhabditis elegans* after acute (24 h) and prolonged exposure (larva to adult) [111]. GO was mixed with nematode food (K medium) and lethality, growth, reproduction and locomotion were analyzed. Results show that prolonged exposure at concentrations 0.5 mg/l and greater lead to significant primary (intestine) and secondary (neurons and reproductive)

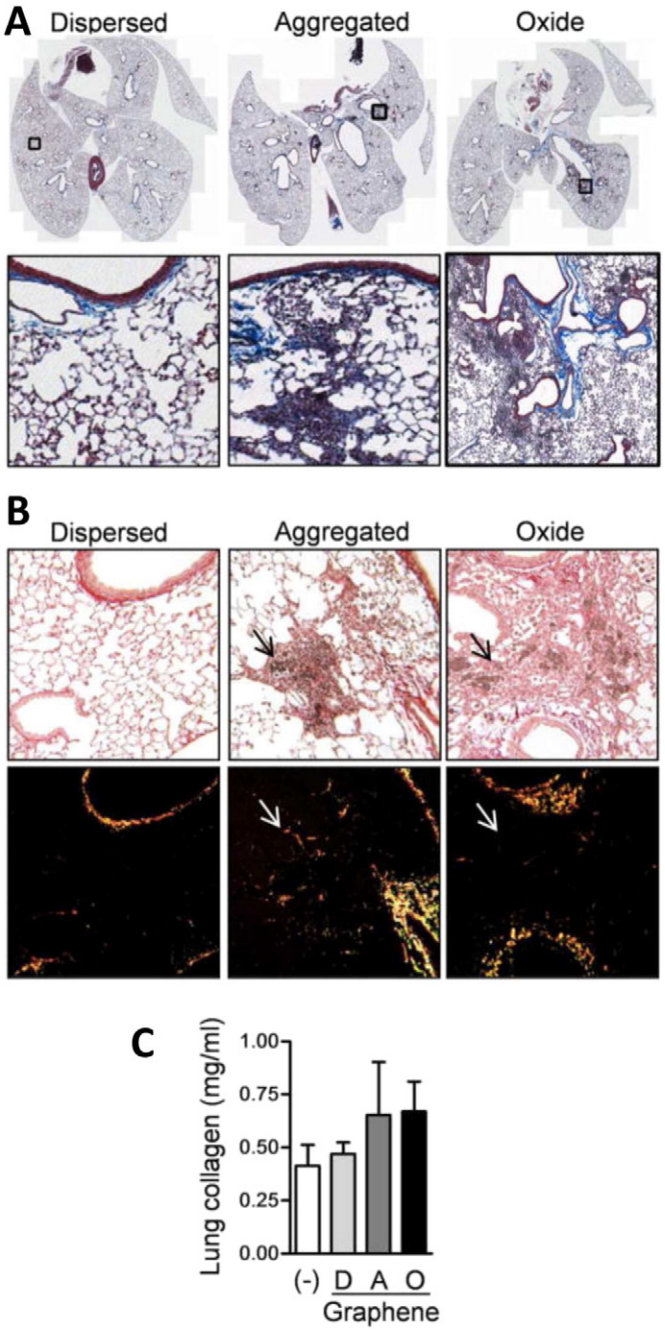

Fig. 14. Aggregated graphene induces patchy fibrosis in mice. Mice were treated with highly purified and dispersed preparations of graphene in 2% Pluronic (dispersed), aggregates of graphene in water (aggregated) or GO in water (oxide) by intratracheal instillation and 21 days later, the lungs were examined for markers of fibrosis. (a) Trichrome stained lung sections. (b) Sirius Red stained lung sections. (c) Total lung collagen determined by picrosirius red precipitation of whole lung homogenates (GD; dispersed graphene, GA; aggregated graphene, GO; graphene oxide).
Adapted from Reference [113] with permission, copyright © American Chemical Society, 2011.

organ damage. Additionally, GO induced loss of villi and translocates into the intestinal walls. Other adverse events noted were increased defecation cycle and hyper permeable intestinal barrier. These results showed that GO upon exposure to environment would come into contact with nematodes, worms and other environmental organisms and may induce long-term adverse effects in the environmental flora.

Table 3
Antibacterial toxicity of graphene.

Material	Characterization	Properties	Dose	Cell line	Assays	Conclusions	References
rGO	FTIR, Raman, TEM, SEM	Size: <5 μm; Raman peaks: 1342 cm^{-1} (D band), 1576 cm^{-1} (G band), $I_G/I_D = 0.85$; FTIR peaks at 3200–3400 cm^{-1} (O–H), 1718 cm^{-1}(C═O), 1579 cm^{-1} (C═C), 1226 cm^{-1} (C–OH), 1070 cm^{-1} (C–O)	0–500 μg/ml	*A. niger*, *F. oxysporum*, *A. oryzae*	Antifungal assay	IC_{50} value is between 50 and 100 μg/ml. rGO shows good antifungal activity.	Sawangphruk et al. [116]
GONW, rGONW	SEM, XPS, Raman	XPS peaks at 285 eV (C–C, C═C, C–H), 285.8 eV (C–OH), 287.6 (C═O), 289.1 eV (O = C–OH); A_{COH}/A_{CC} = 1.35 (GONW) and 0.08 (rGONW). I_D/I_G: 1.78 (GONW) and 1.26 (rGONW)	1 mg/ml	*E. coli*, *S. aureus*	Efflux of RNA	Sharp edges of the nanowalls resulted in efflux of RNA. *S. aureus* bacteria was further damaged as compared to *E. coli*.	Akhavan et al. [117]
PEI-rGO, PEI-rGO-AgNPs	z-Potential, XPS, TEM, UV/vis, AFM, FTIR, XRD	Thickness: 0.6 nm, size: 5–15 nm, zeta potential = −46.7 mV.	0–958 mg/L	*E. coli*, *S. aureus*	Antibacterial test	PEI-rGO shows ~14–20% antibacterial activity which increases to ~90% for PEI-rGO-AgNPs. Blade like edges of PEI-rGO-AgNP causes cell disruption leading to long-term antibacterial effect	Cai et al. [118]
rGO, GO	DLS, AFM, UV–Vis, TEM, Raman, FTIR	Size: 300–600 nm; thickness: 0.76 nm (GO), 1.6 nm (rGO); Raman peaks at 1350 cm^{-1}, 1590 cm^{-1}; UV–Vis peak: 230 nm (GO), 267 nm (rGO); FTIR peaks at 3423 cm^{-1} (O–H), 1750 cm^{-1} (C═O), 1200 cm^{-1} (C–OH), 1050 cm^{-1} (C–O) for GO and 3400 cm^{-1} and 1047 cm^{-1} for rGO.	50–250 μg/ml	*Xanthomonas oryzae* pv. *oryzae*, *Xoo*	Antibacterial activity	GO has extremely prominent dose-dependent inhibitory effect on cell growth due to combination of membrane damage and oxidative stress.	Chen et al. [119]
PVK-GNP thin films	TGA, AFM, UV–Vis	Thickness: 150 nm; roughness: 24.7 nm, UV–Vis peaks at 240, 250, 295, 331 and 344 nm	1, 0.5, 0.05, 0.01 mg/ml	*E. coli*, *B. subtilis*	Metabolic activity assay, bacterial viability assay	Antimicrobial property of PVK-GNP nanocomposite is dependent on the concentration of GNPs. PVK-GNP films do not show cytotoxicity to NIH3T3 fibroblasts.	Santos et al. [120]
PVK-GO	SEM	Size: ~1 μm; thickness: 150 nm; roughness: 24.7 nm, UV–Vis peaks at 240, 250, 295, 331 and 344 nm	10–1000 μg/ml	*Escherichia coli*, *Cupriavidus metallidurans*, *Bacillus subtilis*, *Rhodococcus opacus*	Metabolic activity assay	The addition of PVK to GO enhances antimicrobial properties of the nanocomposite in a dose-dependent manner. PVK-GO nanocomposite has low toxicity towards mammalian cells.	Carpio et al. [121]
GO, rGO and GO or rGO antibacterial paper	SEM, AFM, TEM	Thickness: 1.1 nm (GO), 1 nm (rGO); 1.5 μm (GO paper), 4.6 μm (rGO paper)	0, 20, 85 μg/ml	*E. coli*	ATP assay	GO and rGO demonstrate superior antibacterial effect with only mild cytotoxicity towards mammalian cells (A549). rGO showed slightly greater toxicity towards A549 cells than GO	Hu et al. [122]
Pristine graphene, GO, rGO	TEM, SEM, zeta potential, FTIR	Pristine graphene: size = 1.86 ± 0.6 μm, zeta potential = −17.7 ± 4.3 mV, C═C. GO: size = 1.27 ± 0.1 μm, zeta potential = −49.8 ± 1 mV, O–H, C═C, C═O, C–O, C–H. rGO: size = 2.53 ± 0.2 μm, zeta potential = −25.1 ± 2.6 mV, C═C, C–O, C═O.	25 and 250 μg/ml	*Listeria monocytogenes* and *Salmonella enterica*	Bacterial growth inhibition	GO inhibits (~100% cell death) both bacterial strains at high and low treatment concentration. Pristine graphene and rGO exhibit variable antibacterial response. Presence of oxidative functional groups is important for bacterial cell attachment to graphene	Kurantowicz et al. [126]
GO	AFM, SEM, XPS	Size: 0.753, 0.127, 0.065, 0.035, 0.013, 0.010 $μm^2$, thickness: 1 nm; XPS peaks at 283.17 eV (C═C), 285.21 eV (C–O), 286.9 eV (C═O).	0–80 μg/ml	*E. coli*	Antibacterial activity	Size dependent antibacterial activity of GO sheets. Larger sheets exhibit greater antibacterial activity	Liu et al. [128]
GO, rGO	AFM, SEM, FTIR, XPS	Size: 300 nm (GO), 2.71 μm (rGO); thickness: 1 nm (GO) and few microns (rGO, aggregated); FTIR peaks at 3430 cm^{-1} (O–H), 1720 cm^{-1} (C═O), 1215 cm^{-1} (C–OH), 1050 cm^{-1} (C–O), for rGO no peaks at 1720 cm^{-1}, 1050 cm^{-1} and 1215 cm^{-1}	5–80 μg/ml	*E. coli*	Bacterial membrane, oxidative stress	GO has a higher antibacterial activity than other materials including reduced graphene oxide, graphite oxide and reduced graphite oxide that can be attributed to membrane and oxidative stresses.	Liu et al. [127]

3.4. Pulmonary administration

Schinwald et al. have reported the *in vivo* toxicity of pristine GNPs after intrapleural and pharyngeal administration in 9 weeks old female C57BL/6 mice at 5 μg and 50 μg per mouse doses, respectively [112]. After 24 h and 1 week of administration, a differential cell count of lavage fluid showed that mice exposed to GP had elevated levels (2× of physiological levels) of eosinophils and neutrophils. The chemokine and cytokine protein levels (MIP-1α, MCP-1, MIP-2, IL-8 and IL-1β) were also elevated. Microscopy imaging showed that pleural macrophages were not able to fully phagocytize GNPs due to their size and shape; multiple macrophages surrounding a single GNP forming a rosette-like cell/particle aggregation suggested frustrated phagocytosis. Histological evaluation showed extended retention of GNPs in pleural space and the formation of ganulomatous lesions in bronchiolar lumen. The initial inflammatory response to GNPs reduced after 1-week post administration; reduction in the number of inflammatory cells in the parietal pleura was observed. Clearance of GNPs from the pleural space to cranial mediastinal lymph nodes was observed. 1-week post administration, numerous small sized GNP fragments were observed in lymph nodes. This study shows that the toxicity of GNPs is dependent on the nanomaterial shape and size. The 2D size of GNPs leads to frustrated phagocytosis in lungs.

Duch et al. have reported the pulmonary toxicity of three types of graphene (aggregated pristine graphene in water, pristine graphene in 2% pluronic and graphene oxide) administered via intratracheal instillation to male C56BL/6 mice at 50 μg/mouse dose [113]. After 24 h of administration, mice were euthanized and lungs were analyzed by histology and electron microscopy. Results show that the pulmonary toxicity of graphene varies as a function of dispersion and oxidation state. Highly dispersed pristine graphene in pluronic co-polymer solution induces an acute non-fibrotic lung inflammation, which is significantly lower compared to the local fibrotic response induced by aggregated graphene. Pristine graphene in dispersed or aggregated form does not induce apoptosis or ROS generation in lung macrophages. However, GO formulations lead to persistent lung injury that lasts >21 days (Fig. 14). These results suggest that compared to GO, the use of pristine graphene may reduce potential health risks associated with pulmonary exposure.

Li et al. have analyzed the *in vivo* biodistribution and pulmonary toxicity of GO after intratracheal instillation in kunming mice at a dose of 0, 1, 5 or 10 mg/kg to evaluate dose-dependent acute and chronic pulmonary toxicity for 24 h [114]. The authors have also evaluated time-dependent pulmonary toxicity by administering 10 mg/kg GO for 0, 24, 48, 72 h and 1 week and chronic pulmonary toxicity at 10 mg/kg dose evaluated 1 and 3 months post instillation. Biodistribution was evaluated using SPECT imaging and pulmonary toxicity was assessed using histology and assays for cell injury, lung edema and neutrophil infiltration. Results show that GO was localized in the lungs even after 3 months of administration. Furthermore, GO induced a dose-dependent acute lung injury and resulted in chronic pulmonary fibrosis. A dose-dependent increase in neutrophils was observed in bronchoalveolar lavage fluid. Lung histopathological analysis showed alveolar septa thickening, extensive hemorrhage, changes in alveolar architecture and moderate interstitial edema. Furthermore, increases in the levels of superoxide dismutase and glutathione peroxidase were observed suggesting oxidative stress post 48 h of GO administration. SPECT imaging showed that GO was mainly localized in the lungs with

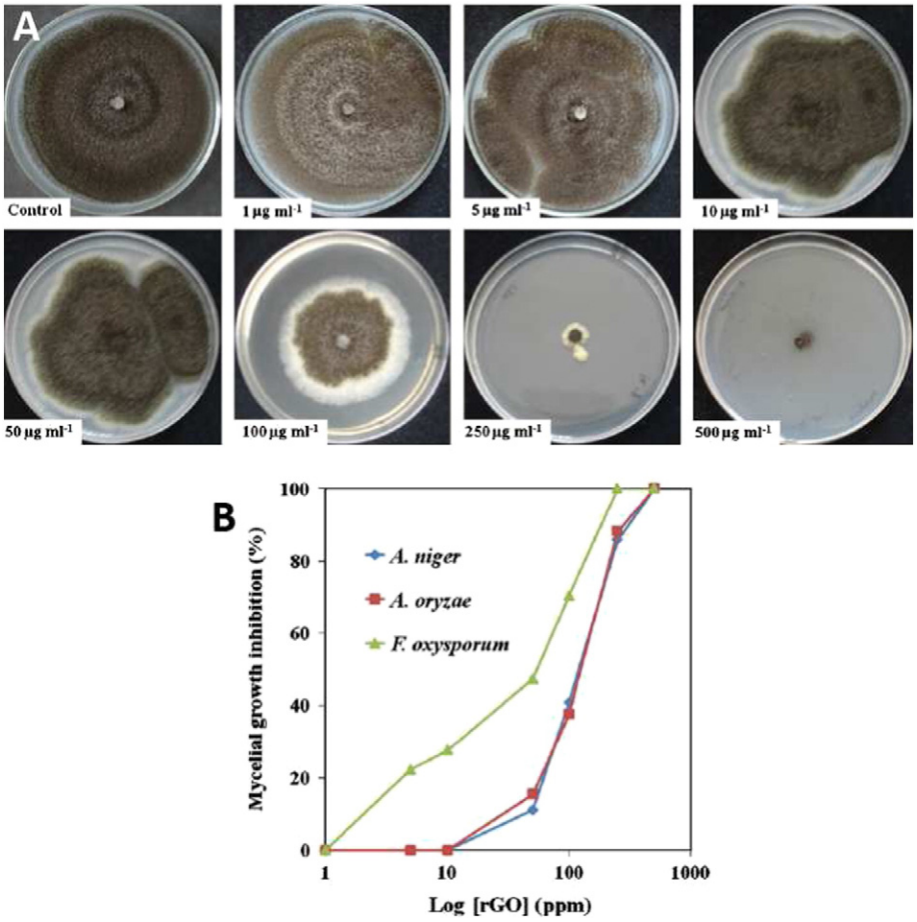

Fig. 15. (A) Mycelial growth inhibition of *A. niger* on media containing 0–500 μg/ml of rGO. (B) Plot of rGO concentration (μg/ml) vs. mycelial growth inhibitory activity (%) of *A. niger*, *A. oryzae* and *F. oxysporum*.
Adapted from Reference [116] with permission, copyright © Elsevier, 2012.

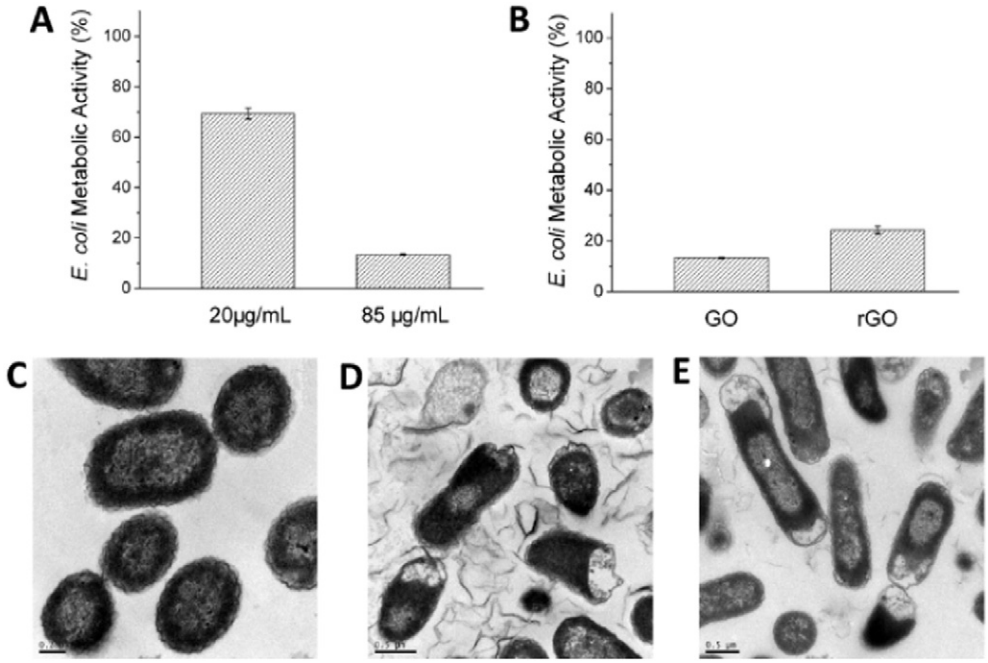

Fig. 16. (A) Metabolic activity of *E. coli* cells upon exposure to GO at 20 and 85 μg/ml concentration for 2 h. (B) Comparative metabolic activity of GO and rGO at 85 μg/ml concentration for 2 h. GO shows greater antibacterial activity than rGO. Transmission electron microscopy images of *E. coli* cells — (C) control (D) after exposure to GO and (E) rGO at 85 μg/ml. Loss of membrane integrity are observed.
Adapted from Reference [122] with permission, copyright © American Chemical Society, 2010.

minor presence in other organs such as liver and intestines suggesting that GO can pass through the air-blood barrier. These results show that GO at the doses and durations used in the study could induce severe pulmonary toxicity.

3.5. Intravitreal administration

In intravitreal administration, a substance/formulation is administered directly into the eye using a needle. Yan et al. have evaluated the ocular toxicity of GO after intravitreal administration in Japanese white rabbits at 0.1, 0.2, or 0.3 mg doses [115]. Eyes were reviewed for the effects of GO using a slit-lamp biomicroscopy and fundoscopy. Results show that GO did not have any effect on the corneas, interior media, posterior media, and the retina compared to the control group. The intraocular pressure showed no difference between the control and the experimental eye. Electroretinography (ERG) was performed to assess changes in the electrical impulse conduction in the eye. Compared to the controls, GO administration did not result in any significant

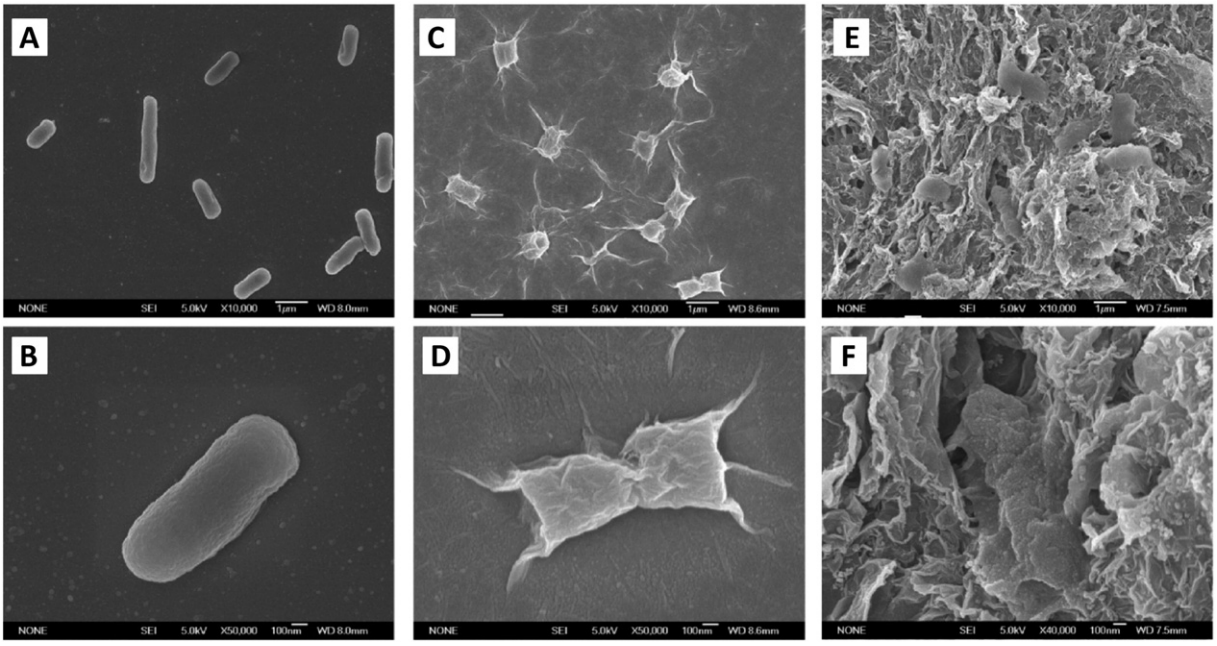

Fig. 17. Scanning electron microscopy images of *E. coli* after 2 h of incubation with (A, B) saline solution, (C, D) GO dispersions 40 μg/ml, (E, F) rGO dispersions at 40 μg/ml. Loss of membrane integrity is clearly observed.
Adapted from Reference [127] with permission, copyright © American Chemical Society, 2011.

Table 4
Environmental toxicity of graphene.

Material	Characterization	Properties	Conclusion	References
Graphene	AFM, SEM, TEM	Height: 1 nm. TEM reveals typical wrinkled structure. Range of length × breadth: 0.5 × 0.6–1.5 × 6.5 μm	Cotyledons and root system growth were slowed down with increasing concentration on tomatoes, cabbage, and red spinach; had no effect on lettuce. Primary roots were shorter and disappeared root hairs compared to the control. Graphene caused decreased root and shoot weight. Decreased number of leaves.	Begum et al. [129]
Few layer graphene	TEM, AFM	Thickness: 2–5 nm; diameter: 100–200 nm	No significant effect on growth of tomato plants.	Khodakovskaya et al. [130]
GONRs	AFM, FTIR, Raman spectroscopy	Bath sonication: 700–900 nm (20 min) Probe sonication: 300–400 nm (1 min), <300 nm (5 min), <200 nm (10 min) I_D/I_G ratio: 1.30 (bath sonication)–2.30 (probe sonication)	Post processing high energy sonication leads to reduction in size of GONRs. Probe sonicated solutions of GONRs show greater medaka embryo mortality compared to non-sonicated or bath sonicated solutions.	Mullick Chowdhury et al. [60]
GO	AFM, XPS, SEM	Interlayer spacing: 1 nm	Inhibition of metabolic activity at all concentrations. GO is biodegraded by at least 50% after 5 h. Inhibition of nitrifying bacteria.	Ahmed et al. [131]
Graphene	TEM, AFM, Raman spectroscopy	No holes or defects, basic hexagonal lattice. Height: 0.34 nm	Post hydrogen peroxide treatment: randomly distributed holes in graphene. Diameter of holes increase with higher concentration of H_2O_2.	Xing et al. [132]
GONRs and rGONRs	TEM, Raman spectroscopy, UV–Vis	Flat, smooth, and uniform multi-layered sheets.	Lignin peroxidase activity: GONR: structure completely degraded by 96 h. rGONR: holes from outer to inner layers in the sheets. Both materials eventually degrade, but there is a delay in degradation for rGONR compared to GONR	Lalwani et al. [133]

changes in ERG amplitudes after 2, 7, 28 or 49 days of administration. H&E staining of eyes harvested 49 days post administration showed small amounts of GO residue, however, no retinal abnormality was observed.

4. Antimicrobial toxicity

Table 3 summarizes the studies assessing antimicrobial toxicity of graphene. Sawangphruk et al. have investigated the antifungal activity of reduced graphene oxide (rGO) against *Aspergillus niger*, *Aspergillus oryzae*, and *Fusarium oxysporum* between 0 and 500 μg/ml treatment concentrations [116]. Antifungal effects of rGO were assessed by quantifying mycelial growth inhibition. It was found that the rGO was effective against all three fungi with IC_{50} value between 50 and 100 μg/ml indicating a good antifungal activity of rGO (Fig. 15). *A. niger* and *F. oxysporum* are pathogenic strains of fungi whereas *A. oryzae* is non-pathogenic, therefore; antifungal activity of rGO against *A. oryzae* could be a concern towards the development of graphene based broad spectrum antifungal agents. Akhavan et al. reported the antibacterial activity of graphene oxide nanowalls (GONWs) and reduced graphene oxide nanowalls (rGONWs) against *Escherichia coli* and *Staphylococcus aureus* [117]. Results showed that bacterial cells were damaged by the direct contact of the cell membrane with extremely sharp edges of GO. Gram positive *S. aureus* without cell membrane showed greater cell death compared to gram positive *E. coli which* was more resistant due to the presence of outer membrane. Additionally, rGONWs were more toxic to bacterial cells than GONWs due to effective charge transfer between bacteria and edges of nanowalls during bacterial cell contact.

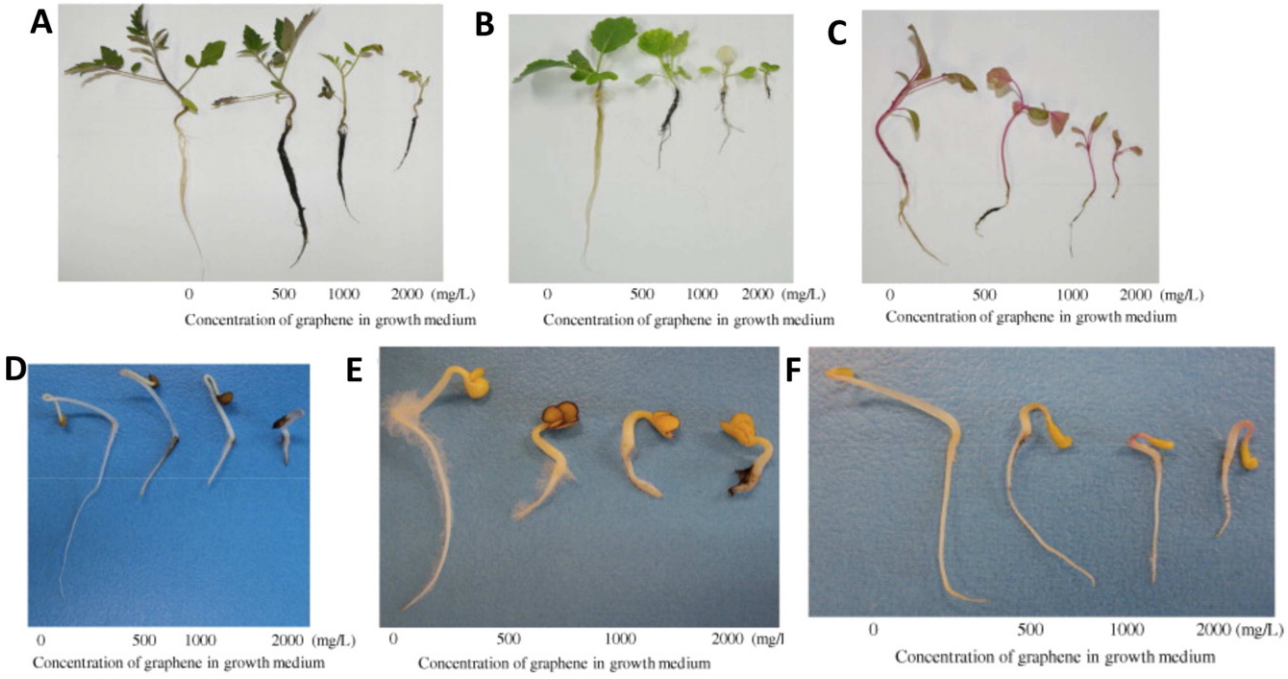

Fig. 18. Effect of graphene on growth and development of (A–C) seedling and (D–F) cotyledons and root systems of cabbage, tomato and red spinach after exposure to 500–2000 mg/l concentration for 20 and 4 days, respectively. A dose-dependent reduction in the plant growth and biomass production is observed.
Adapted from Reference [129] with permission, copyright © Elsevier, 2011.

Cai et al. investigated the antibacterial activity of polyethyleneimine-modified reduced graphene oxide (PEI-rGO) and sliver nanoparticles functionalized PEI-rGO (PEI-rGO-AgNPs) against *E. coli* and *S. aureus* between 0 and 958 mg/l treatment concentration [118]. The results show that PEI-rGO-AgNPs are extremely effective in killing bacteria, >90% reduction in cell viability was observed for both *E. coli* and *S. aureus* colonies at 958 mg/l concentration. The long term antibacterial activity of PEI-rGO-AgNPs was attributed to the damage of bacterial cell due to interactions with sharp blade like edges of GO which may facilitate effective interactions of Ag^{+} ions with the intracellular contents, eventually killing bacteria. Chen et al. have reported the dose-dependent antibacterial activity of GO and rGO against a rod shaped, gram negative phytopathogenic bacterium *Xanthomonas oryzae* pv. *oryzae* (*Xoo*) [119]. GO exhibited a greater antibacterial effect with ~94.5 and 86.4% cell mortality in DI water and 0.9% NaCl dispersions at 250 μg/ml treatment concentration. rGO at 250 μg/ml concentration resulted in 36.1 and 22.3% cell mortality Furthermore, an increased incubation time from 1 h to 4 h resulted in significant increases in the antibacterial activity of GO (from 19.4% to 66.1%) and rGO (13.8% to 30.5%). Further analysis by TEM and thiol quantification assay showed that GO resulted in physical damage and increased oxidative stress to bacterial cells. These results suggest that GO has a significantly greater dose- and time-dependent antibacterial activity compared to rGO.

Santos et al. investigated the antibacterial activity of poly(*N*-vinylcarbazole) graphene (PVK-G) solutions and thin films against *E. coli* and *Bacillus subtilis* at concentrations between 0.01 and 1 mg/ml [120]. Results show a dose-dependent antibacterial effect of PVK-G solutions with ~80% reduction in the percentage of metabolically active cells at 1 mg/ml treatment concentration. AFM imaging showed less bacterial coverage on PVK-G films compared to PVK and ITO (control) surfaces after 24 h of incubation with *E. coli*. Furthermore, PVK-G solutions at 1 mg/ml concentration showed ~80% cell viability of NIH3T3 fibroblast cells. These results showed good antibacterial activity of PVK-G composites and thin films and suggest a potential use of PVK-G nanocomposites for a wide variety of antibacterial applications where bactericidal properties along with good biocompatibility are desired. In another study, Carpio, Santos et al. have investigated the antibacterial properties of PVK-graphene oxide (PVK-GO) nanocomposites between 10 and 1000 μg/ml treatment concentrations against *E. coli*, *Cupriavidus metallidurans*, *B. subtilis*, and *Rhodococcus opacus* [121]. The results showed a similar effect wherein addition of GO to PVK enhances the antimicrobial properties of the nanocomposite. PVK-GO nanocomposites in solution appear to effectively encapsulate the bacterial cells leading to reduction in microbial metabolic potential and eventual cell death. AFM imaging showed significant reduction in *E. coli* biomass after 48 h of culture on PVK-GO films in comparison to PVK and ITO (controls) surfaces. Additionally, similar to PVK-G nanocomposites, PVK-GO nanocomposites were also cytocompatible (~90% cell viability of NIH3T3 cells was observed after 48 h of exposure to PVK-GO solutions at 1000 μg/ml concentration).

Hu et al. investigated the antibacterial activity of GO and rGO nanosheets against *E. coli* cells at concentrations of 0, 20, and 85 μg/ml [122]. After 2 h of incubation with GO at 20 and 85 μg/ml, the metabolic activity of *E. coli* cells (measured by luciferase-based ATP assay) decreased to ~70% and ~13%, respectively (Fig. 16A). rGO exhibited antibacterial activity, 2 h of incubation of *E. coli* cells with rGO solutions at 85 μg/ml resulted in only ~24% cell viability (Fig. 16B). TEM studies showed loss of cell integrity via physical damages to the cell membrane upon exposure to GO and rGO (Fig. 16C–E). Furthermore, cells cultured on GO and rGO paper also showed damages to cell membrane of bacteria. However, Mangadlao et al. [123], Hui et al. [124], and Li et al. [125] have reported that antibacterial effect of GO films is not due to cell membrane rupture by graphene edges. The antibacterial effect is observed due to charge transfer between basal plane of graphene and bacterial cell body leading to inactivation of bacteria.

Kurantowicz et al. investigated the interactions of pristine graphene, graphene oxide (GO) and reduced graphene oxide (rGO) against food

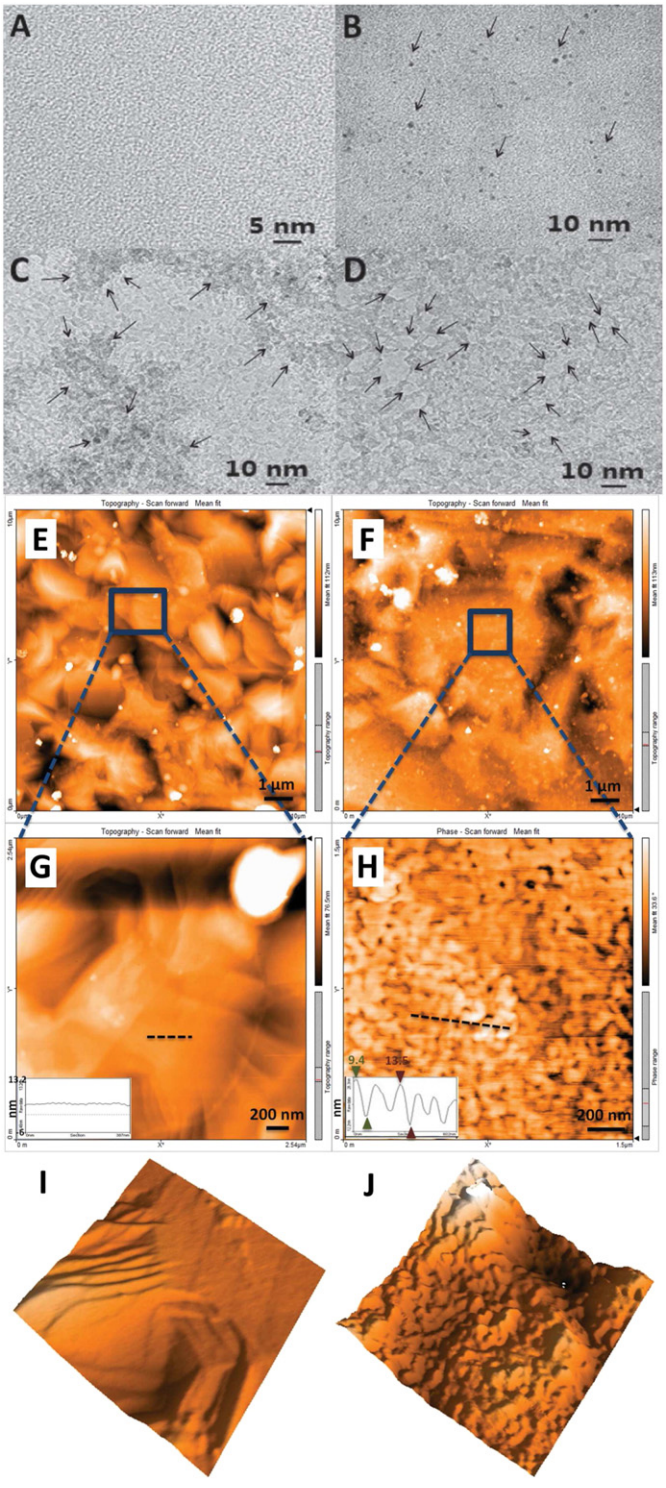

Fig. 19. (A–D) Representative transmission electron microscopy images of multilayered graphene treated with (A) DI water, (B) 1 μM H_2O_2, (C) 100 μM H_2O_2 and (D) 10,000 μM H_2O_2 for 10 h. Arrows in (B) indicate the formation of holes on graphene sheets and in (C) indicate the formation of lighter (few graphene layers) and darker regions (multiple graphene layers) suggesting the degradation of multilayered graphene. (E–J) Representative atomic force microscopy images of multilayered graphene on Ni wafer. (E and G) are topographical scans of graphene incubated with DI water for 25 h. (G and H) show graphene after 25 h of incubation with 10,000 μM H_2O_2. Inset in images (G and H) are corresponding height profiles. (I and J) are 3D representations of images G and H.
Adapted from Reference [132] with permission, copyright © John Wiley and Sons Inc., 2014.

borne bacterial pathogens — *Listeria monocytogenes* and *Salmonella enterica* [126]. Bacteria were incubated with high (250 μg/ml) and low (25 μg/ml) treatment concentrations of pristine graphene, GO and rGO for 18 h. At 250 μg/ml concentration, all nanomaterials consistently inhibited 100% growth of *S. enterica* and *L. monocytogenes*. However, at lower concentration (25 μg/ml), only GO showed 100% inhibition of both bacteria. Pristine graphene inhibited the growth of *S. enterica* by 96.5% and *L. monocytogenes* by 54.5% whereas rGO inhibited the growth of *L. monocytogenes* by 91% and *S. enterica* by 46%. TEM results showed a uniform distribution of bacterial cells over the surface of GO whereas on the surface of pristine graphene and rGO, bacterial cells adhered to the edges and wrinkles of the graphene sheets. The authors hypothesized that the presence of oxidative functional groups throughout the surface of GO and on the edges of pristine graphene and rGO act as bait for attracting bacteria. After attaching to the flakes, cell may be damaged via direct contact or destabilization of the phospholipid cell membrane. These results suggested functionalization-dependent antibacterial effect of graphene and GO.

Liu et al. investigated the time- and dose-dependent antibacterial activity of four types of graphene-based materials (graphite (Gt), graphite oxide (GtO), graphene oxide (GO), and reduced graphene oxide (rGO)) against *E. coli* [127]. At 40 μg/ml treatment concentration after 2 h of incubation, Gt, GtO, GO and rGO showed ~26.1 ± 4.8%, 15.0 ± 3.7%, 69.3 ± 6.1% and 45.9 ± 4.8%, respectively. After 4 h, GO and rGO dispersions lead to ~89.7 ± 3.1% and 74.9 ± 4.8% inhibition of *E. coli*. GO and rGO exhibited a concentration dependent antibacterial activity, cell mortality increases from 10.5 ± 6.6% to 91.6 ± 3.2% by increasing the GO concentration from 5 μg/ml to 80 μg/ml. Similarly, increases in rGO concentration from 5 μg/ml to 80 μg/ml leads to increased *E. coli* mortality from 8.4 ± 7.3% to 76.8 ± 3.1%. The antibacterial activity of GO and rGO was primarily due to inactivation of cellular functions due to loss of cell integrity. SEM imaging showed that direct contact of *E. coli* cells with GO and rGO disrupts cell membrane (Fig. 17). Additionally, graphene-based materials also oxidize glutathione, which is a redox mediator in bacterial cells, leading to oxidative stress. In another study, Liu et al. investigated the lateral-dimension dependent antibacterial activity of GO [128]. The sizes of GO sheets used in this study were 0.753, 0.127, 0.065, 0.035, 0.013, and 0.010 μm^2, respectively. Results showed that large GO sheets exhibit significantly greater antibacterial activity compared to small GO sheets. The results of both these investigations taken together suggested that GO and rGO are effective antibacterial agents and physiochemical properties such as functional group density, size, and morphology play an important role in influencing the antibacterial potential of graphene-based materials.

5. Environmental toxicity

The use of graphene for various industrial and healthcare applications would lead to increased environmental exposure and its disposal into waste streams. Therefore, it is important to assess the short- and

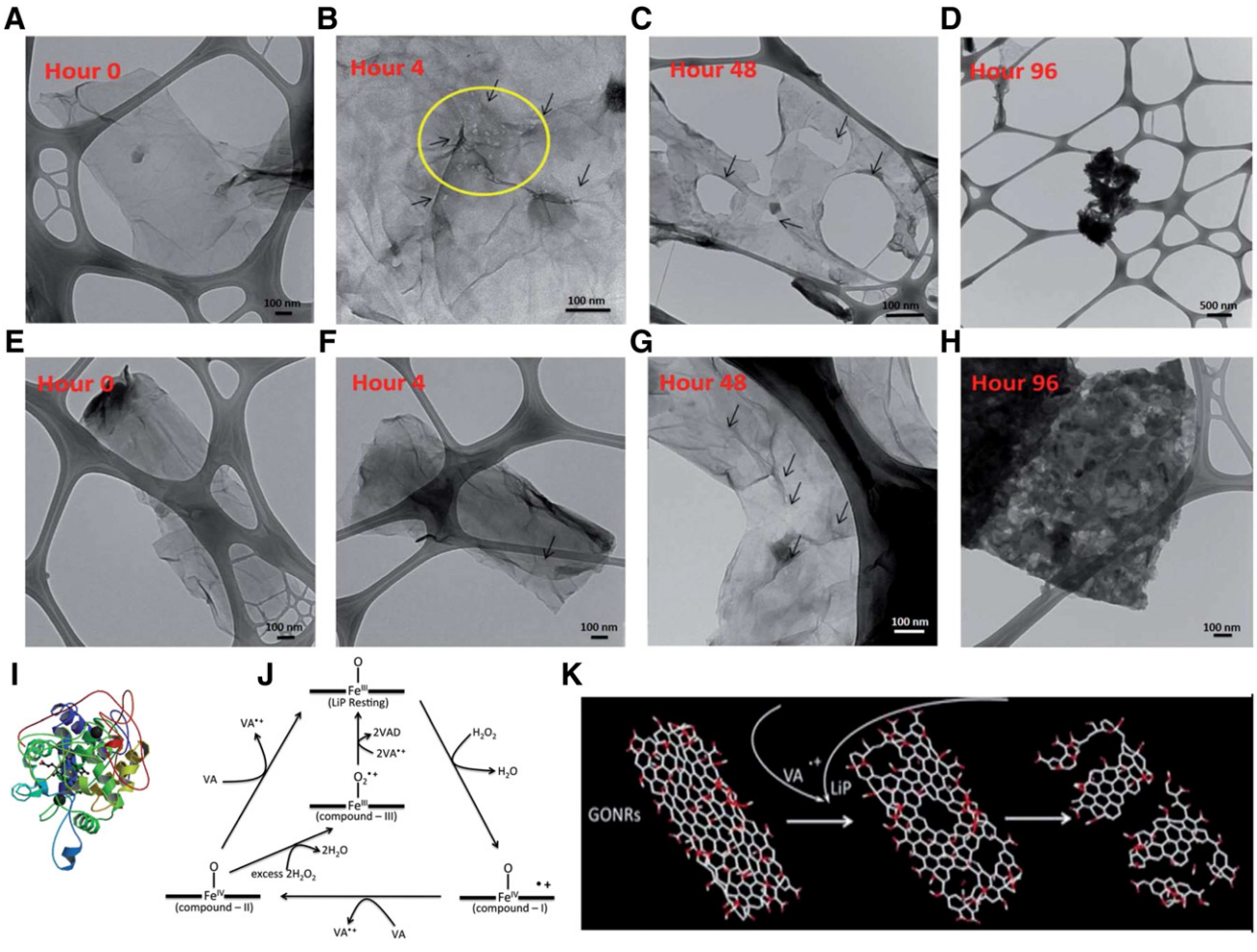

Fig. 20. Representative transmission electron microscopy images of oxidized and reduced graphene oxide nanoribbons (GONRs — A–D) and (rGONRs — E–H) after 0, 4, 48, and 96 h of treatment with lignin peroxidase. Arrows in B, D and G indicate the formation of holes on graphene sheets. Extensive biodegradation of GONRs whereas the formation of holey rGONRs is observed after 96 h of incubation. (I) Ribbon diagram of lignin peroxidase, (J) Enzymatic cycle of lignin peroxidase and (K) Schematic representation of degradation of graphene in the presence of lignin peroxidase.
Adapted from Reference [133] with permission, copyright © Royal Society of Chemistry, 2014.

long-term environmental toxicity of graphene and graphene-based materials and develop effective strategies to minimize any potential deleterious impact to flora and fauna. Table 4 summarizes the studies assessing environmental toxicity of graphene. Begum et al. have investigated the phytotoxicity of graphene and its effects on root and shoot growth and shape, cell death and biomass by incubating seedlings of cabbage, tomatoes, red spinach and lettuce with 500–2000 mg/l for 20 days [129]. The results of physiological and morphological analysis showed that graphene significantly inhibited plant growth and biomass production (Fig. 18) and led to a reduction in the number and size of leaves in a dose-dependent manner. At 2000 mg/l concentration, ~18–78% root growth inhibition was observed depending on the plant species. Furthermore, leaves show wilting, necrotic lesions and reduction in leaf area. Graphene at high treatment concentrations (>500 mg/l) led to the production of reactive oxygen species leading to necrosis, loss of plasma membrane, and eventual cell death. No toxic effects were observed on lettuce at similar treatment concentrations. These results indicated that the phytotoxicity of graphene depends on the concentration, exposure time and plant species.

Khodakovskaya et al. investigated the toxicity of several carbon nanomaterials (activated carbon, graphene, single- and multi-walled carbon nanotubes) on the germination of tomato seedlings [130]. All nanomaterials were mixed with Murashige and Skoog (MS) growth medium at 50 μg/mL used to grow surface sterilized tomato seedlings. Examination of leaves and roots show that graphene (out of all materials tested) induced lowest activation of stress-related *LeAqp2* gene (tomato water-channel protein); highest activation was observed for CNT groups. Photothermal and photoacoustic imaging studies showed that graphene did not affect the plant growth rate due to the inability to penetrate plant tissues.

Mullick Chowdhury et al. evaluated the post-processing effects of graphene oxide nanoribbons (GONRs) dispersed in biological buffers using various sonication steps (bath sonication for 5 or 20 min or probe sonication for 5 or 10 min) on Medaka embryos [60]. Results show precocious hatching of the embryos when exposed to GONR solutions prepared by bath sonication. However, significant mortality (~50% increase in cell death) of the embryos was observed for GONR solutions prepared by probe sonication. AFM imaging showed the presence of smaller GONR particles and carbonaceous debris after probe sonication. Probe sonicated GONR solutions lead to structural damage of the chorionic membrane of embryos. These results suggested that post-processing steps of graphene such as high-energy sonication may lead to variable environmental toxicity.

Ahmed et al. investigated the effects of graphene oxide on the microbial community present in wastewater [131]. Efficient biological wastewater treatment requires functioning of diverse microbial species. Active sludge samples were incubated with 10–300 mg/l concentration of GO for 5 h at room temperature to observe short-term toxicity. Results show a dose-dependent toxicity with significant reduction in bacterial metabolic activity, viability, and their capacity to effectively remove nutrients such as organics, phosphorous and nitrogen from activated sludge in the presence of GO. A dose-dependent reduction in the conversion of ammonia to nitrate was observed suggesting a reduction in the concentration of nitrifying bacteria. It was noted that the presence of GO in wastewater led to deterioration of the quality of final wastewater effluent (increased turbidity was observed). Results showed that interaction of GO with wastewater sludge induced production of reactive oxygen species which may disrupt the functioning of antimicrobial community leading to compromised wastewater treatment performance.

Hydrogen peroxide (H_2O_2) is a naturally occurring ubiquitous compound found in rain and surface water, and in biological systems at concentrations ranging between 1 μM and 10,000 μM. Xing et al. have investigated the effects of hydrogen peroxide on the biodegradation of graphene [132]. TEM and AFM imaging studies show the presence of

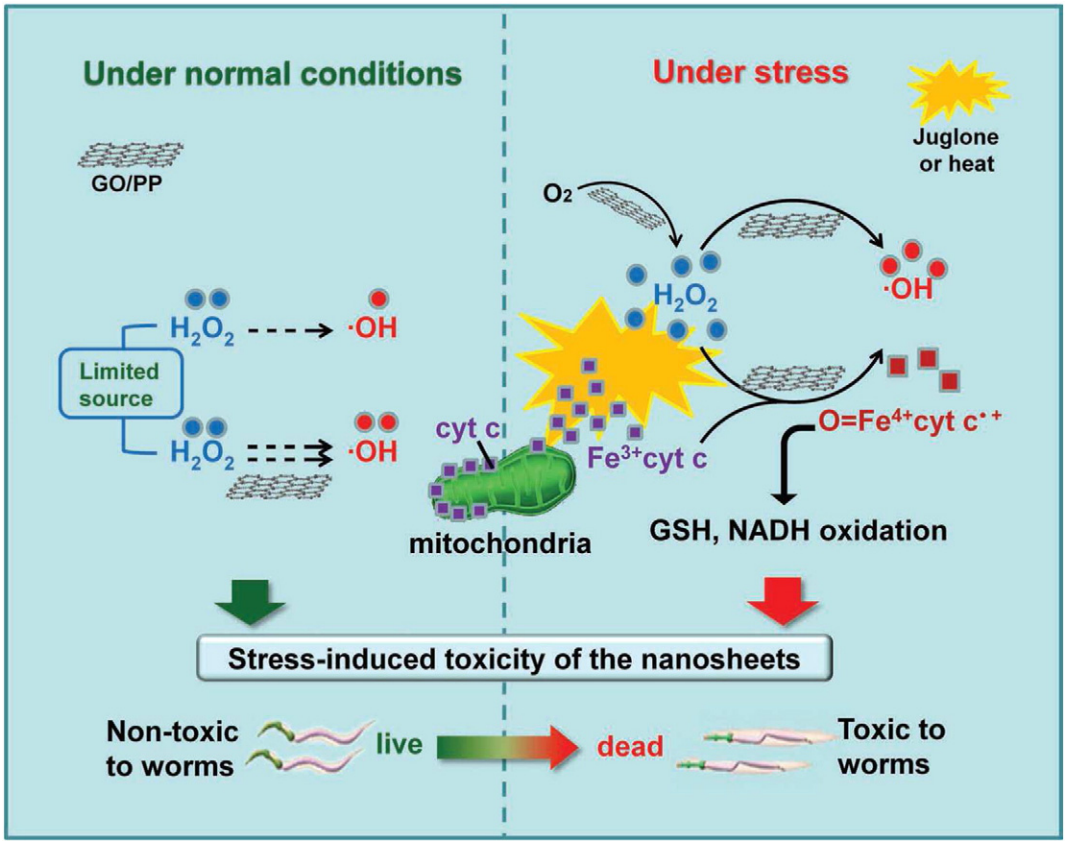

Fig. 21. Schematic representation of the proposed mechanism of oxidative stress induced toxicity by graphene oxide. Adapted from Reference [135] with permission, copyright © John Wiley & Sons Inc., 2012.

randomly distributed holes on graphene sheets in the presence of physiologically and environmentally relevant concentrations of H_2O_2 (Fig. 19). After 10 h of incubation with H_2O_2, the diameter of holes was between 1 and 15 nm. An increase in the concentration of H_2O_2 from 1 μM to 10,000 μM induced the formation of holes with significantly greater diameters (10–30 nm) suggesting a concentration dependent biodegradation of graphene. AFM studies show the depth of holes between 9.4 and 13.5 nm; greater than the height of a single graphene sheet (~0.34 nm). Based on these results, it was concluded that H_2O_2 attacked the inner layers of graphene along with the outer surface layers. Raman spectroscopy results showed a progressive time- and concentration-dependent decrease in the intensity for both D and G bands for all H_2O_2 treatment groups. The biodegradation of graphene by H_2O_2 may further be accelerated by the presence of trace elements such as nickel or iron (used as catalysts during the synthesis of graphene) by catalyzing the conversion of hydrogen peroxide to hydroxyl radicals via the Haber–Weiss reaction. The results of this study showed that multilayered graphene can undergo effective biodegradation at environmental and physiological concentrations of H_2O_2.

Lalwani et al. have investigated the oxidative biodegradation of graphene oxide nanoribbons (GONRs) and reduced graphene oxide nanoribbons (rGONRs) by lignin peroxidase (LiP), an enzyme released by white rot fungi (*Phanerochaete chrysosporium*) distributed worldwide in forests soils with dead and decaying organic matter [133]. LiP degrades lignin — a component of plant cell wall. TEM (Fig. 20) and Raman spectroscopy analysis of GONRs and rGONRs treated with LiP for 4–96 h showed the formation of holes confirming the structural degradation of graphene sheets. It was observed that GONRs showed a higher rate of biodegradation compared to rGONRs; numerous holes (1–5 nm diameter) were detected on GONR sheets within 4 h of treatment which increased to ~300–350 nm after 48 h. The diameter of holes on rGONRs was between 5 and 30 nm after 48 h of enzymatic treatment. After 96 h, GONRs appeared to have

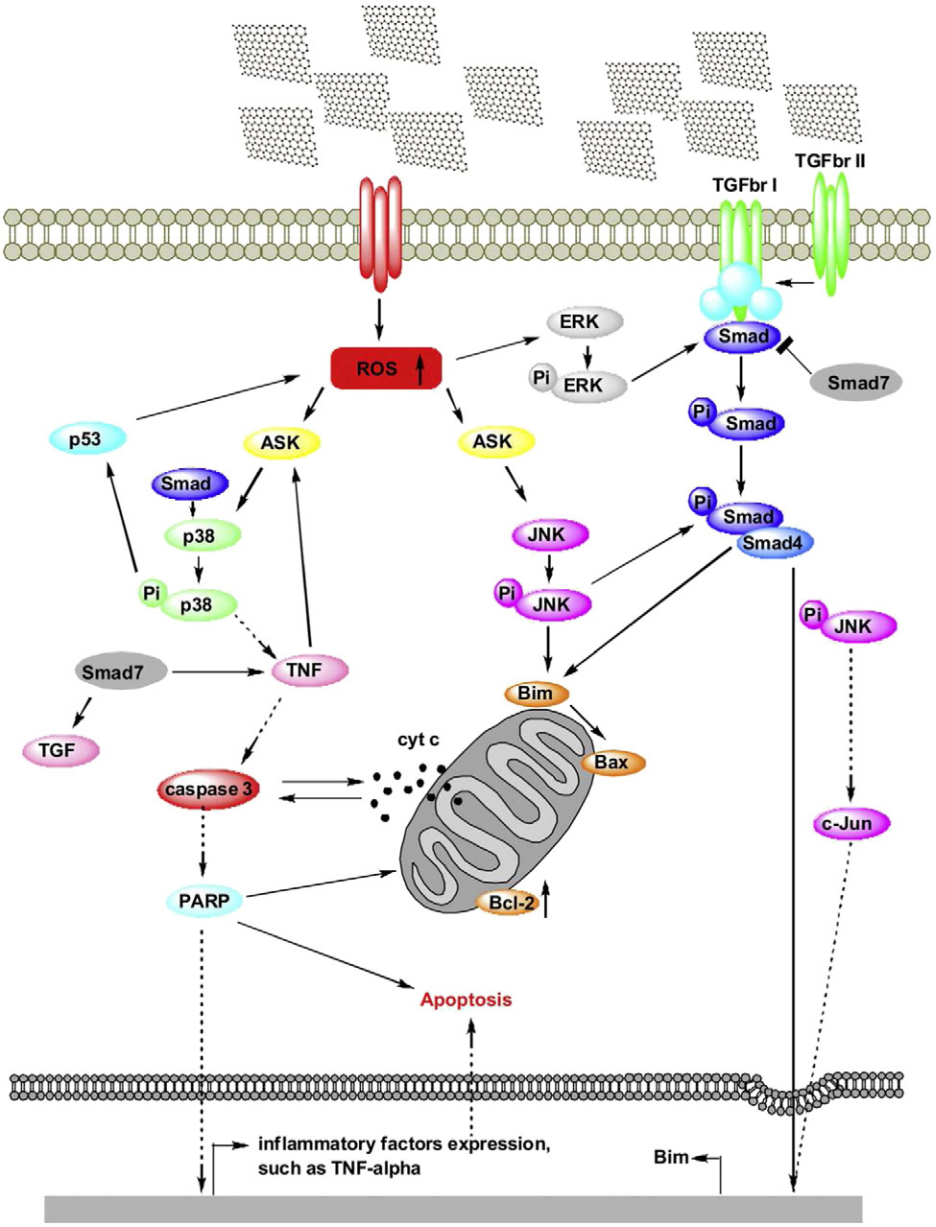

Fig. 22. Schematic illustrating the signaling pathways involved in pristine-graphene induced cell apoptosis via ROS mediated MAPK and TGF-beta pathways (mitochondria dependent apoptotic cascades).
Adapted from Reference [82] with permission, copyright © Elsevier, 2012.

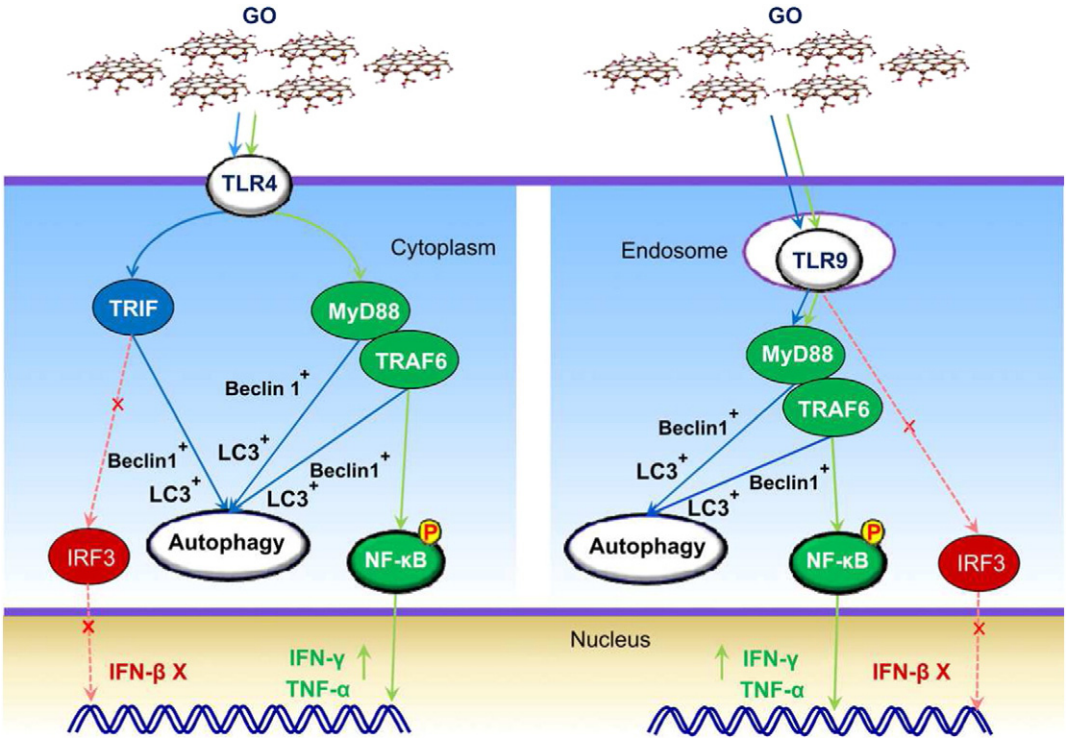

Fig. 23. Overview of the GO-induced cytokine response and autophagy mediated by the TLR4/TLR9 signaling pathway. GO treatment led to the activation of TLR4 and TLR9, which relayed signals through MyD88-TRAF6-NF-κB and ultimately gave rise to cytokine expression. However, GO-induced TLRs signaling neither elicited IFN-b expression nor activated IRF3, suggesting that TRIF and IRF3 were dispensable in the inflammatory response. Conversely, GO-induced TLR4-MyD88-TRAF6 and TLR4-TRIF signaling cascades signaled through Beclin 1 to initiate autophagy. GO engagement of TLR9 also activated MyD88 and TRAF6, leading to Beclin 1 and LC3 activation and subsequent autophagy.
Adapted from Reference [83] with permission, copyright © Elsevier, 2012.

completely degraded whereas numerous holes extending throughout the width of rGONRs were observed. These results suggested that oxidized and reduced graphene nanoribbons released in the environment may undergo oxidative biodegradation by lignin peroxidase.

6. Mechanisms of toxicity

The interactions of graphene with cells, proteins, and other biomolecules are influenced by its physiochemical properties such as

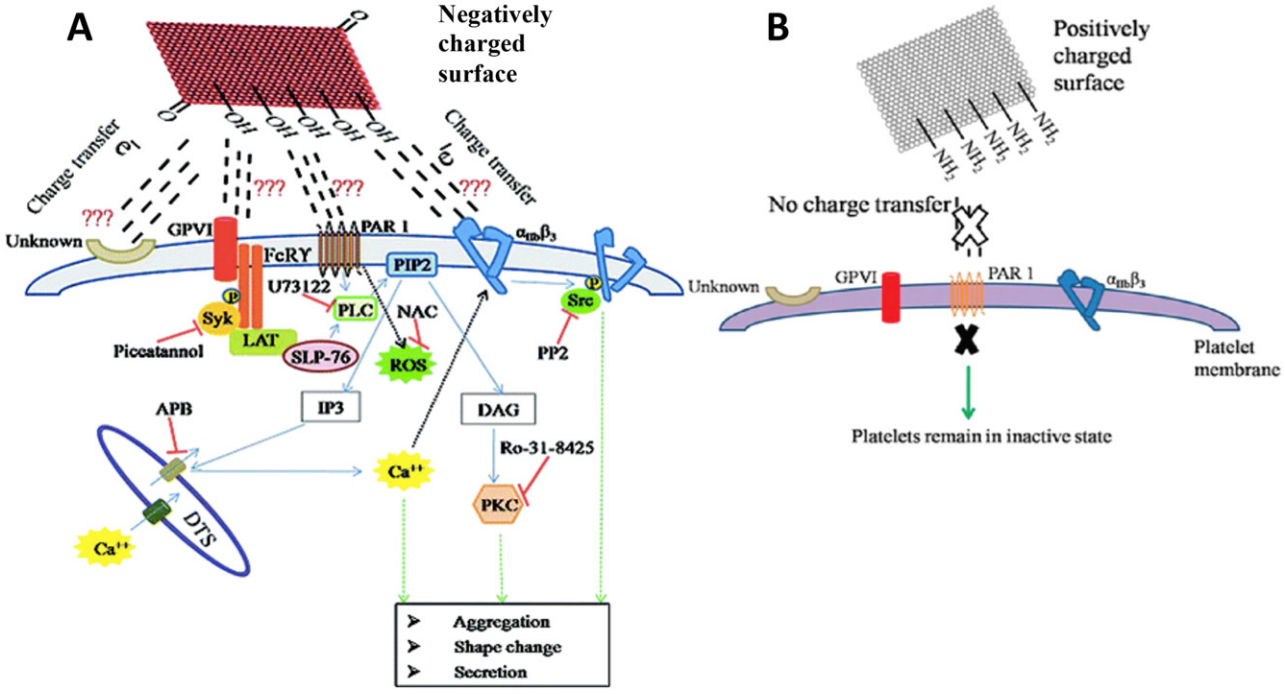

Fig. 24. Schematic illustrating the interaction of (A) graphene oxide (negative surface charge) and (B) amine-modified graphene (positive surface charge) on platelet function. Surface charge distribution determines the interactions of graphene with different agonist receptors on platelet membrane.
(A) Adapted from Reference [86] and (B) adapted from Reference [87] with permissions, copyright © American Chemical Society, 2011 and 2012.

shape, size, functional group density and charge transfer abilities. The main mechanism of graphene toxicity is associated with the generation of intracellular reactive oxygen species that cause damage to proteins and DNA leading to cell death via apoptotic or necrotic pathways [82,134,135]. Graphene can be internalized into cells via passive internalization (endocytosis) [136,137] or active internalization (clathrin mediated energy dependent endocytosis [138] or actin-dependent macropinocytosis [36]). Studies have elucidated two mechanism of graphene mediated ROS damage: (1) Upon cellular internalization, GO interferes with the electron transport system, induces overproduction of H_2O_2 and hydroxyl radicals. This leads to the oxidization of cardiolipin and the release and translocation of hemoprotein from mitochondrial inner membrane to the cytoplasm. This triggers release of cytochrome c complex (*cyt c*) which induces calcium release from endoplasmic reticulum and activates caspase 9 which in turn activates caspases 3 and 7 leading to cell death (Fig. 21) [135]. (2) GO induces the activation of MAPK (JNK, ERK, p38) and TGF-β signaling pathways that lead to activation of Bcl-2 proteins which in turn activate mitochondria-induced apoptosis (Fig. 22) [82]. In addition to ROS induced cell death, GO may also lead to the activation of toll-like receptors and induce autophagy via inflammatory pathways (Fig. 23) [83]. Post internalization; graphene may induce DNA cleavage due to interactions such as pi–pi stacking, hydrophobicity, and electrostatic interactions [139–141]. Singh et al. have shown that surface charge distribution on graphene sheets plays an important role in the activation of *src* kinases and release of calcium eventually leading to platelet aggregation (Fig. 24) [86,94].

Several studies have reported that extremely sharp edges of graphene lead to membrane destabilization and loss of cell integrity by direct contact [66,117]. Wang et al. have shown that adsorption of GO on RBCs leads to the loss of cell membrane resulting in hemolysis [136]. Long sheets of graphene have also been observed to wrap around bacterial cells thereby inhibiting their growth [121]. Single layered GONRs exhibit greater cyto- and geno-toxicity due to the interactions between cells and sharp edges of nanoribbons resulting in extensive chromosomal aberration and DNA fragmentation [66]. Li et al. have shown that graphene micro sheets enter cells through spontaneous membrane penetration at corner sites and edge asperities [142]. Molecular dynamics simulation studies have shown that graphene has a strong affinity for phospholipids and can be localized into the hydrophobic interior of biological membranes [143]. Tu et al. reported that due to strong interactions between graphene and lipids, graphene penetrates into and extracts significantly large amounts of phospholipids from cell membrane leading to cytotoxicity (Fig. 25) [144]. Graphene quantum dots affected cellular function by inserting into cell membrane [145]; pristine GO has been reported to form aggregates on cell

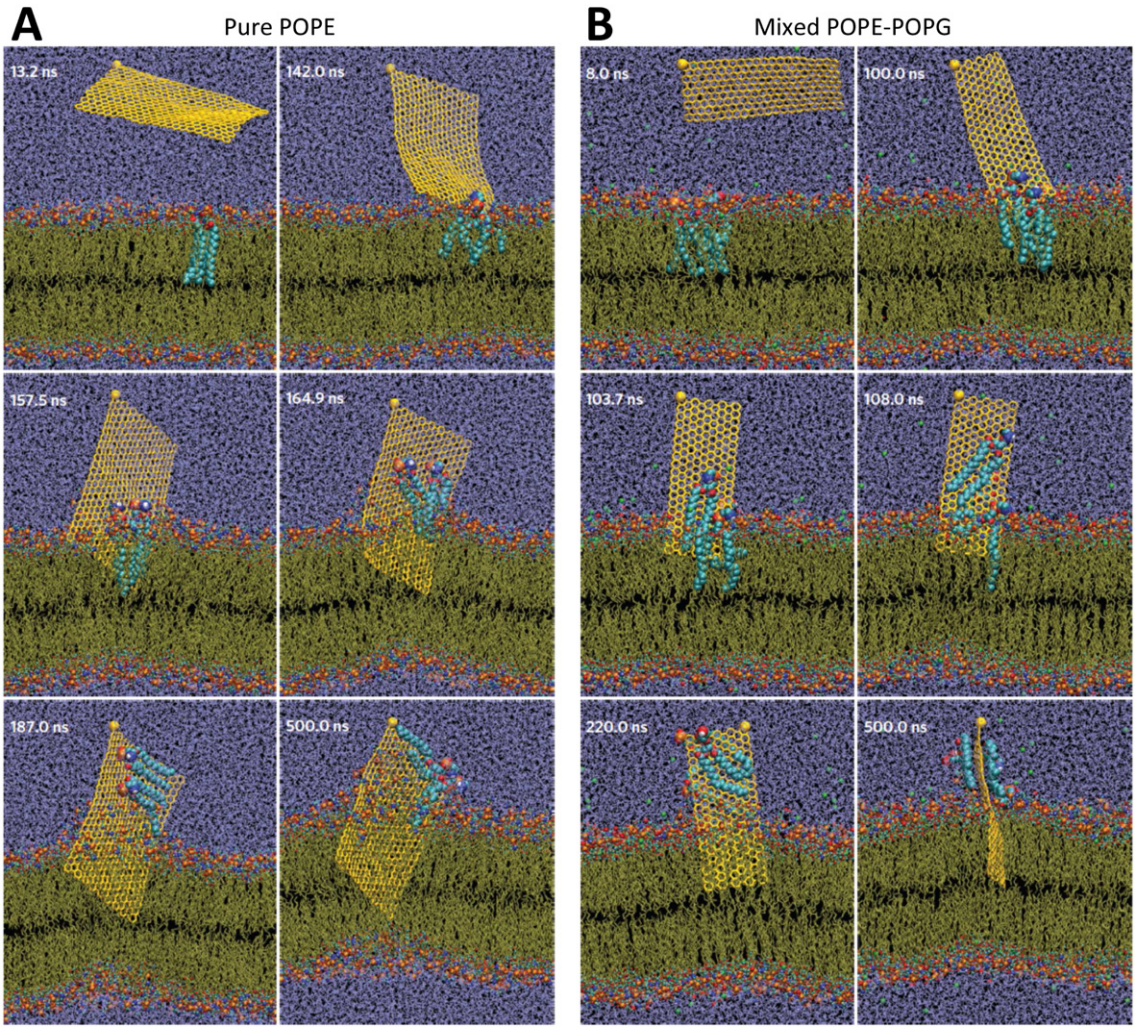

Fig. 25. Representative simulated trajectories of graphene nanosheets insertion and lipid extraction in the outer membrane (pure palmitoyloleoylphosphatidylethanolamine, POPE) and inner membrane (mixed POPE-POPG) of *E. coli*. Water is represented in violet and phospholipids in tan lines with hydrophilic charged atoms as colored spheres (hydrogen — white, oxygen — red, nitrogen — dark blue, carbon — cyan and phosphorus — orange). Graphene is shown as yellow sheet with a large sphere marked at one corner representing restrained atom in simulations. Extracted phospholipids are shown as large spheres.
Adapted from Reference [144] with permission, copyright © Macmillan Publishers Limited, 2013.

membrane thereby affecting cellular morphology [68]. rGO sheets inhibited the growth of fungal mycelium due to their direct insertion into the membrane of fungal cells [116].

7. Conclusion and future perspective

The studies till date indicate that toxicity of graphene could be dependent on the shape, size, purity, post-production processing steps, oxidative state, functional groups, dispersion state, synthesis methods, route and dose of administration, and exposure times. The morphology, shape and size of graphene nanoparticles could influence their cellular uptake characteristics whereas presence of functional groups can alter their interactions with proteins, biomolecules and micronutrients. The initial starting materials and the methods used in the production of oxidized graphene can result in the presence of metallic impurities and oxidative debris in the final product, which could result in variable toxicity effects. The post synthesis processing steps employed to disperse the nanoparticles in aqueous media could also influence toxicity. Reactive oxidation species mediated cell damage has been postulated as a primary cytotoxicity mechanism of graphene. Graphene sheets with sharp edges could induce direct physical damage and interact with phospholipids leading to membrane destabilization. Surface coating of graphene with several biocompatible moieties (e.g. natural polymers) can mitigate these cytotoxicity effects.

The studies taken together provide information on dosaging, biodistribution and pharmacology of various graphene-based formulations. It must be noted that even though there are many types of graphene nanoparticles, GO have been the most widely used for biomedical applications and studies that employ GO dominate the review. While majority of published literature on toxicity of other members of the graphene family have been reviewed herein, more toxicological studies on formulations of other types of graphene nanoparticles are warranted. Additionally, for all types of graphene nanoparticles, it is important to investigate and critically evaluate the potential short- and long-term health risks and toxicity hazards after acute, sub-acute and chronic exposures using *in vitro* and *in vivo* (small and large animal) models. Towards clinical translation of any graphene-based biomedical application that requires its systemic administration, formulations with high purity, dispersibility in aqueous media, and controlled physiochemical properties are highly desirable. For each of these formulations, regulatory compliance would require mapping of their chemistry, manufacturing and control (CMC) process and completing new drug (IND)-enabling preclinical studies. With advancements in the synthesis methods and establishment of several commercial ventures for large-scale industrial production of graphene, the widespread use of graphene for several consumer products is becoming a reality. This ubiquitous use would lead to an increased environmental exposure of graphene. Therefore, more studies assessing the long-term environmental impact of graphene are required. Recent efforts have also involved incorporation of graphene nanoparticles in polymer matrices or their assembly in coating, films and porous scaffolds for bio-sensing, localized drug delivery or tissue engineering applications [146,147]. For these applications, additional *in vitro* and *in vivo* toxicological studies specific to biomedical devices and implants would be needed. Finally, advances in graphene-like inorganic nanoparticles for biomedical applications allow opportunities to compare the biological response of graphene and its inorganic analogs [41,43,148–151]. All these studies will further advance the knowledge required to develop safe graphene-based technologies and products suitable for healthcare applications and to minimize risks to human health.

Acknowledgments

The authors acknowledge the financial support of National Institutes of Health (grant no. 1DP2OD007394-01) and Wallace H. Coulter Foundation's Translational Research Award.

References

[1] M.S. Dresselhaus, G. Dresselhaus, P.C. Eklund, Science of Fullerenes and Carbon Nanotubes: Their Properties and Applications, Academic press, 1996.
[2] A.K. Geim, Graphene: status and prospects, Science 324 (5934) (2009) 1530–1534.
[3] G. Lalwani, B. Sitharaman, Multifunctional fullerene-and metallofullerene-based nanobiomaterials, Nano. LIFE 3 (3) (2013) 1342003 (-1-22).
[4] The rise and rise of graphene, Nat. Nanotechnol. 5 (11) (2010) 755.
[5] The Kavli Prize, Kavli Prize Laureates in Nanoscience, http://www.kavliprize.org/prizes-and-laureates/prizes/2008-kavli-prize-laureates-nanoscience2008 ( ).
[6] A.K. Geim, K.S. Novoselov, The rise of graphene, Nat. Mater. 6 (3) (2007) 183–191.
[7] J. Slonczewski, P. Weiss, Band structure of graphite, Phys. Rev. 109 (2) (1958) 272.
[8] R. Peierls, Quelques propriétés typiques des corps solides, Annales de l'institut Henri Poincaré, 1935.
[9] L. Landau, Zur Theorie der phasenumwandlungen II, Phys. Z. Sowjetunion 11 (1937) 26–35.
[10] L.D. Landau, E. Lifshitz, Statistical physics, part I, Course Theor. Phys. 5 (1980) 468.
[11] N.D. Mermin, Crystalline order in two dimensions, Phys. Rev. 176 (1) (1968) 250.
[12] K.S. Novoselov, A.K. Geim, S. Morozov, D. Jiang, Y. Zhang, S.A. Dubonos, I. Grigorieva, A. Firsov, Electric field effect in atomically thin carbon films, Science 306 (5696) (2004) 666–669.
[13] K. Novoselov, A.K. Geim, S. Morozov, D. Jiang, M. Katsnelson, I. Grigorieva, S. Dubonos, A. Firsov, Two-dimensional gas of massless Dirac fermions in graphene, Nature 438 (7065) (2005) 197–200.
[14] K. Novoselov, D. Jiang, F. Schedin, T. Booth, V. Khotkevich, S. Morozov, A. Geim, Two-dimensional atomic crystals, Proc. Natl. Acad. Sci. U. S. A. 102 (30) (2005) 10451–10453.
[15] D. Johnson, Europe invests €1 billion to become "graphene valley", IEEE Spectr. (2013).
[16] M. Spasenovic, South Korea to spend US$40 million on graphene development, Graphene Tracker, 2013.
[17] M. Brown, Government announces £50m funding hub for UK graphene research, WIRED, 2011.
[18] HUAWEI, Huawei Announces Partnership With the University of Manchester to Develop Graphene-based Technologies, 2015.
[19] K.I. Bolotin, K. Sikes, Z. Jiang, M. Klima, G. Fudenberg, J. Hone, P. Kim, H. Stormer, Ultrahigh electron mobility in suspended graphene, Solid State Commun. 146 (9) (2008) 351–355.
[20] X. Du, I. Skachko, A. Barker, E.Y. Andrei, Approaching ballistic transport in suspended graphene, Nat. Nanotechnol. 3 (8) (2008) 491–495.
[21] M.D. Stoller, S. Park, Y. Zhu, J. An, R.S. Ruoff, Graphene-based ultracapacitors, Nano Lett. 8 (10) (2008) 3498–3502.
[22] L. Ponomarenko, A. Geim, A. Zhukov, R. Jalil, S. Morozov, K. Novoselov, I. Grigorieva, E. Hill, V. Cheianov, V. Fal'Ko, Tunable metal–insulator transition in double-layer graphene heterostructures, Nat. Phys. 7 (12) (2011) 958–961.
[23] Y. Zhang, Y.-W. Tan, H.L. Stormer, P. Kim, Experimental observation of the quantum Hall effect and Berry's phase in graphene, Nature 438 (7065) (2005) 201–204.
[24] A.A. Balandin, S. Ghosh, W. Bao, I. Calizo, D. Teweldebrhan, F. Miao, C.N. Lau, Superior thermal conductivity of single-layer graphene, Nano Lett. 8 (3) (2008) 902–907.
[25] C. Lee, X. Wei, J.W. Kysar, J. Hone, Measurement of the elastic properties and intrinsic strength of monolayer graphene, Science 321 (5887) (2008) 385–388.
[26] R. Nair, P. Blake, A. Grigorenko, K. Novoselov, T. Booth, T. Stauber, N. Peres, A. Geim, Fine structure constant defines visual transparency of graphene, Science 320 (5881) (2008) 1308.
[27] P. Avouris, C. Dimitrakopoulos, Graphene: synthesis and applications, Mater. Today 15 (3) (2012) 86–97.
[28] K. Subrahmanyam, L. Panchakarla, A. Govindaraj, C. Rao, Simple method of preparing graphene flakes by an arc-discharge method, J. Phys. Chem. C 113 (11) (2009) 4257–4259.
[29] K.S. Kim, Y. Zhao, H. Jang, S.Y. Lee, J.M. Kim, K.S. Kim, J.-H. Ahn, P. Kim, J.-Y. Choi, B.H. Hong, Large-scale pattern growth of graphene films for stretchable transparent electrodes, Nature 457 (7230) (2009) 706–710.
[30] S. Stankovich, D.A. Dikin, R.D. Piner, K.A. Kohlhaas, A. Kleinhammes, Y. Jia, Y. Wu, S.T. Nguyen, R.S. Ruoff, Synthesis of graphene-based nanosheets via chemical reduction of exfoliated graphite oxide, Carbon 45 (7) (2007) 1558–1565.
[31] D.V. Kosynkin, A.L. Higginbotham, A. Sinitskii, J.R. Lomeda, A. Dimiev, B.K. Price, J.M. Tour, Longitudinal unzipping of carbon nanotubes to form graphene nanoribbons, Nature 458 (7240) (2009) 872–876.
[32] S. Pei, H.-M. Cheng, The reduction of graphene oxide, Carbon 50 (9) (2012) 3210–3228.
[33] S. Kanakia, J.D. Toussaint, S.M. Chowdhury, G. Lalwani, T. Tembulkar, T. Button, K.R. Shroyer, W. Moore, B. Sitharaman, Physicochemical characterization of a novel graphene-based magnetic resonance imaging contrast agent, Int. J. Nanomedicine 8 (2013) 2821.
[34] G. Lalwani, X. Cai, L. Nie, L.V. Wang, B. Sitharaman, Graphene-based contrast agents for photoacoustic and thermoacoustic tomography, Photoacoustics 1 (3) (2013) 62–67.
[35] G. Lalwani, J.L. Sundararaj, K. Schaefer, T. Button, B. Sitharaman, Synthesis, characterization, in vitro phantom imaging, and cytotoxicity of a novel graphene-based multimodal magnetic resonance imaging-X-ray computed tomography contrast agent, J. Mater. Chem. B 2 (22) (2014) 3519–3530.
[36] S. Mullick Chowdhury, G. Lalwani, K. Zhang, J.Y. Yang, K. Neville, B. Sitharaman, Cell specific cytotoxicity and uptake of graphene nanoribbons, Biomaterials 34 (1) (2013) 283–293.
[37] S.M. Chowdhury, C. Surhland, Z. Sanchez, P. Chaudhary, M.S. Kumar, S. Lee, L.A. Peña, M. Waring, B. Sitharaman, M. Naidu, Graphene nanoribbons as a drug delivery agent for lucanthone mediated therapy of glioblastoma multiforme, Nanomed.: Nanotechnol., Biol. Med. 11 (1) (2015) 109–118.
[38] L. Feng, S. Zhang, Z. Liu, Graphene based gene transfection, Nanoscale 3 (3) (2011) 1252–1257.
[39] B. Tian, C. Wang, S. Zhang, L. Feng, Z. Liu, Photothermally enhanced photodynamic therapy delivered by nano-graphene oxide, ACS Nano 5 (9) (2011) 7000–7009.
[40] P. Huang, C. Xu, J. Lin, C. Wang, X. Wang, C. Zhang, X. Zhou, S. Guo, D. Cui, Folic acid-conjugated graphene oxide loaded with photosensitizers for targeting photodynamic therapy, Theranostics 1 (2011) 240.

[41] G. Lalwani, A.M. Henslee, B. Farshid, L. Lin, F.K. Kasper, Y.-X. Qin, A.G. Mikos, B. Sitharaman, Two-dimensional nanostructure-reinforced biodegradable polymeric nanocomposites for bone tissue engineering, Biomacromolecules 14 (3) (2013) 900–909.
[42] S.C. Patel, G. Lalwani, K. Grover, Y.-X. Qin, B. Sitharaman, Fabrication and cytocompatibility of in situ crosslinked carbon nanomaterial films, Scie. Rep. 5 (2015).
[43] B. Farshid, G. Lalwani, B. Sitharaman, In vitro cytocompatibility of one-dimensional and two-dimensional nanostructure-reinforced biodegradable polymeric nanocomposites, J. Biomed. Mater. Res. Part A 103 (7) (2015) 2309–2321.
[44] Y. Talukdar, J.T. Rashkow, G. Lalwani, S. Kanakia, B. Sitharaman, The effects of graphene nanostructures on mesenchymal stem cells, Biomaterials 35 (18) (2014) 4863–4877.
[45] T.R. Nayak, H. Andersen, V.S. Makam, C. Khaw, S. Bae, X. Xu, P.-L.R. Ee, J.-H. Ahn, B.H. Hong, G. Pastorin, Graphene for controlled and accelerated osteogenic differentiation of human mesenchymal stem cells, ACS Nano 5 (6) (2011) 4670–4678.
[46] Y. Yang, A.M. Asiri, Z. Tang, D. Du, Y. Lin, Graphene based materials for biomedical applications, Mater. Today 16 (10) (2013) 365–373.
[47] K. Yang, L. Feng, X. Shi, Z. Liu, Nano-graphene in biomedicine: theranostic applications, Chem. Soc. Rev. 42 (2) (2013) 530–547.
[48] X. Hu, Q. Zhou, Health and ecosystem risks of graphene, Chem. Rev. 113 (5) (2013) 3815–3835.
[49] A.B. Seabra, A.J. Paula, R. de Lima, O.L. Alves, N. Durán, Nanotoxicity of graphene and graphene oxide, Chem. Res. Toxicol. 27 (2) (2014) 159–168.
[50] J. Zhao, Z. Wang, J.C. White, B. Xing, Graphene in the aquatic environment: adsorption, dispersion, toxicity and transformation, Environ. Sci. Technol. 48 (17) (2014) 9995–10009.
[51] F.M. Tonelli, V.A. Goulart, K.N. Gomes, M.S. Ladeira, A.K. Santos, E. Lorençon, L.O. Ladeira, R.R. Resende, Graphene-based nanomaterials: biological and medical applications and toxicity, Nanomedicine 10 (15) (2015) 2423–2450.
[52] D. Bitounis, H. Ali-Boucetta, B.H. Hong, D.H. Min, K. Kostarelos, Prospects and challenges of graphene in biomedical applications, Adv. Mater. 25 (16) (2013) 2258–2268.
[53] A. Bianco, Graphene: safe or toxic? The two faces of the medal, Angew. Chem. Int. Ed. 52 (19) (2013) 4986–4997.
[54] K. Yang, Y. Li, X. Tan, R. Peng, Z. Liu, Behavior and toxicity of graphene and its functionalized derivatives in biological systems, Small 9 (9–10) (2013) 1492–1503.
[55] V.C. Sanchez, A. Jachak, R.H. Hurt, A.B. Kane, Biological interactions of graphene-family nanomaterials: an interdisciplinary review, Chem. Res. Toxicol. 25 (1) (2011) 15–34.
[56] A.M. Jastrzębska, P. Kurtycz, A.R. Olszyna, Recent advances in graphene family materials toxicity investigations, J. Nanopart. Res. 14 (12) (2012) 1–21.
[57] B. Zhang, Y. Wang, G. Zhai, Biomedical applications of the graphene-based materials, Mater. Sci. Eng. C (2015).
[58] C.H.A. Wong, Z. Sofer, M. Kubešová, J. Kučera, S. Matějková, M. Pumera, Synthetic routes contaminate graphene materials with a whole spectrum of unanticipated metallic elements, Proc. Natl. Acad. Sci. 111 (38) (2014) 13774–13779.
[59] A. Ambrosi, C.K. Chua, B. Khezri, Z. Sofer, R.D. Webster, M. Pumera, Chemically reduced graphene contains inherent metallic impurities present in parent natural and synthetic graphite, Proc. Natl. Acad. Sci. 109 (32) (2012) 12899–12904.
[60] S. Mullick Chowdhury, S. Dasgupta, A.E. McElroy, B. Sitharaman, Structural disruption increases toxicity of graphene nanoribbons, J. Appl. Toxicol. 34 (11) (2014) 1235–1246.
[61] Y. Zhang, S.F. Ali, E. Dervishi, Y. Xu, Z. Li, D. Casciano, A.S. Biris, Cytotoxicity effects of graphene and single-wall carbon nanotubes in neural phaeochromocytoma-derived PC12 cells, ACS Nano 4 (6) (2010) 3181–3186.
[62] N.V. Vallabani, S. Mittal, R.K. Shukla, A.K. Pandey, S.R. Dhakate, R. Pasricha, A. Dhawan, Toxicity of graphene in normal human lung cells (BEAS-2B), J. Biomed. Nanotechnol. 7 (1) (2011) 106–107.
[63] J. Yuan, H. Gao, J. Sui, H. Duan, W.N. Chen, C.B. Ching, Cytotoxicity evaluation of oxidized single-walled carbon nanotubes and graphene oxide on human hepatoma HepG2 cells: an iTRAQ-coupled 2D LC–MS/MS proteome analysis, Toxicol. Sci. 126 (1) (2012) 149–161.
[64] M. Lv, Y. Zhang, L. Liang, M. Wei, W. Hu, X. Li, Q. Huang, Effect of graphene oxide on undifferentiated and retinoic acid-differentiated SH-SY5Y cells line, Nanoscale 4 (13) (2012) 3861–3866.
[65] E.L.K. Chng, C.K. Chua, M. Pumera, Graphene oxide nanoribbons exhibit significantly greater toxicity than graphene oxide nanoplatelets, Nanoscale 6 (18) (2014) 10792–10797.
[66] O. Akhavan, E. Ghaderi, H. Emamy, F. Akhavan, Genotoxicity of graphene nanoribbons in human mesenchymal stem cells, Carbon 54 (2013) 419–431.
[67] S. Jaworski, E. Sawosz, M. Grodzik, A. Winnicka, M. Prasek, M. Wierzbicki, A. Chwalibog, In vitro evaluation of the effects of graphene platelets on glioblastoma multiforme cells, Int. J. Nanomedicine 8 (2013) 413–420.
[68] A. Sasidharan, L.S. Panchakarla, P. Chandran, D. Menon, S. Nair, C.N. Rao, M. Koyakutty, Differential nano-bio interactions and toxicity effects of pristine versus functionalized graphene, Nanoscale 3 (6) (2011) 2461–2464.
[69] M.C. Matesanz, M. Vila, M.J. Feito, J. Linares, G. Goncalves, M. Vallet-Regi, P.A. Marques, M.T. Portoles, The effects of graphene oxide nanosheets localized on F-actin filaments on cell-cycle alterations, Biomaterials 34 (5) (2013) 1562–1569.
[70] X. Yuan, Z. Liu, Z. Guo, Y. Ji, M. Jin, X. Wang, Cellular distribution and cytotoxicity of graphene quantum dots with different functional groups, Nanoscale Res. Lett. 9 (1) (2014) 1–9.
[71] L. Horváth, A. Magrez, M. Burghard, K. Kern, L. Forró, B. Schwaller, Evaluation of the toxicity of graphene derivatives on cells of the lung luminal surface, Carbon 64 (2013) 45–60.
[72] S. Das, S. Singh, V. Singh, D. Joung, J.M. Dowding, D. Reid, J. Anderson, L. Zhai, S.I. Khondaker, W.T. Self, Oxygenated functional group density on graphene oxide: its effect on cell toxicity, Part. Part. Syst. Charact. 30 (2) (2013) 148–157.
[73] Y. Chong, Y. Ma, H. Shen, X. Tu, X. Zhou, J. Xu, J. Dai, S. Fan, Z. Zhang, The in vitro and in vivo toxicity of graphene quantum dots, Biomaterials 35 (19) (2014) 5041–5048.
[74] W.Z. Teo, E.L.K. Chng, Z. Sofer, M. Pumera, Cytotoxicity of halogenated graphenes, Nanoscale 6 (2) (2014) 1173–1180.
[75] W.Z. Teo, Z. Sofer, F. Šembera, Z. Janoušek, M. Pumera, Cytotoxicity of fluorographene, RSC Adv. 5 (129) (2015) 107158–107165.
[76] E.L.K. Chng, Z. Sofer, M. Pumera, Cytotoxicity profile of highly hydrogenated graphene, Chem. Eur. J. 20 (21) (2014) 6366–6373.
[77] E. Sawosz, S. Jaworski, M. Kutwin, K.P. Vadalasetty, M. Grodzik, M. Wierzbicki, N. Kurantowicz, B. Strojny, A. Hotowy, L. Lipińska, Graphene functionalized with arginine decreases the development of glioblastoma multiforme tumor in a gene-dependent manner, Int. J. Mol. Sci. 16 (10) (2015) 25214–25233.
[78] O. Akhavan, E. Ghaderi, A. Akhavan, Size-dependent genotoxicity of graphene nanoplatelets in human stem cells, Biomaterials 33 (32) (2012) 8017–8025.
[79] Y. Chang, S.T. Yang, J.H. Liu, E. Dong, Y. Wang, A. Cao, Y. Liu, H. Wang, In vitro toxicity evaluation of graphene oxide on A549 cells, Toxicol. Lett. 200 (3) (2011) 201–210.
[80] H. Yue, W. Wei, Z. Yue, B. Wang, N. Luo, Y. Gao, D. Ma, G. Ma, Z. Su, The role of the lateral dimension of graphene oxide in the regulation of cellular responses, Biomaterials 33 (16) (2012) 4013–4021.
[81] X. Zhi, H. Fang, C. Bao, G. Shen, J. Zhang, K. Wang, S. Guo, T. Wan, D. Cui, The immunotoxicity of graphene oxides and the effect of PVP-coating, Biomaterials 34 (21) (2013) 5254–5261.
[82] Y. Li, Y. Liu, Y. Fu, T. Wei, L. Le Guyader, G. Gao, R.S. Liu, Y.Z. Chang, C. Chen, The triggering of apoptosis in macrophages by pristine graphene through the MAPK and TGF-beta signaling pathways, Biomaterials 33 (2) (2012) 402–411.
[83] G.Y. Chen, H.J. Yang, C.H. Lu, Y.C. Chao, S.M. Hwang, C.L. Chen, K.W. Lo, L.Y. Sung, W.Y. Luo, H.Y. Tuan, Y.C. Hu, Simultaneous induction of autophagy and toll-like receptor signaling pathways by graphene oxide, Biomaterials 33 (27) (2012) 6559–6569.
[84] A.V. Tkach, N. Yanamala, S. Stanley, M.R. Shurin, G.V. Shurin, E.R. Kisin, A.R. Murray, S. Pareso, T. Khaliullin, G.P. Kotchey, V. Castranova, S. Mathur, B. Fadeel, A. Star, V.E. Kagan, A.A. Shvedova, Graphene oxide, but not fullerenes, targets immunoproteasomes and suppresses antigen presentation by dendritic cells, Small 9 (9–10) (2013) 1686–1690.
[85] K.H. Liao, Y.S. Lin, C.W. Macosko, C.L. Haynes, Cytotoxicity of graphene oxide and graphene in human erythrocytes and skin fibroblasts, ACS Appl. Mater. Interfaces 3 (7) (2011) 2607–2615.
[86] S.K. Singh, M.K. Singh, M.K. Nayak, S. Kumari, S. Shrivastava, J.J. Gracio, D. Dash, Thrombus inducing property of atomically thin graphene oxide sheets, ACS Nano 5 (6) (2011) 4987–4996.
[87] S.K. Singh, M.K. Singh, P.P. Kulkarni, V.K. Sonkar, J.J. Gracio, D. Dash, Amine-modified graphene: thrombo-protective safer alternative to graphene oxide for biomedical applications, ACS Nano 6 (3) (2012) 2731–2740.
[88] S.M. Chowdhury, S. Kanakia, J.D. Toussaint, M.D. Frame, A.M. Dewar, K.R. Shroyer, W. Moore, B. Sitharaman, In vitro hematological and in vivo vasoactivity assessment of dextran functionalized graphene, Sci. Rep. 3 (2013).
[89] S.M. Chowdhury, J. Fang, B. Sitharaman, Interaction of graphene nanoribbons with components of the blood vascular system, Future Sci. OA (2015) **1**(3).
[90] M. Wojtoniszak, X. Chen, R.J. Kalenczuk, A. Wajda, J. Lapczuk, M. Kurzewski, M. Drozdzik, P.K. Chu, E. Borowiak-Palen, Synthesis, dispersion, and cytocompatibility of graphene oxide and reduced graphene oxide, Colloids Surf. B: Biointerfaces 89 (2012) 79–85.
[91] W. Hu, C. Peng, M. Lv, X. Li, Y. Zhang, N. Chen, C. Fan, Q. Huang, Protein corona-mediated mitigation of cytotoxicity of graphene oxide, ACS Nano 5 (5) (2011) 3693–3700.
[92] Q. Mu, G. Su, L. Li, B.O. Gilbertson, L.H. Yu, Q. Zhang, Y.P. Sun, B. Yan, Size-dependent cell uptake of protein-coated graphene oxide nanosheets, ACS Appl. Mater. Interfaces 4 (4) (2012) 2259–2266.
[93] D.A. Mbeh, O. Akhavan, T. Javanbakht, M. Mahmoudi, L.H. Yahia, Cytotoxicity of protein corona-graphene oxide nanoribbons on human epithelial cells, Appl. Surf. Sci. 320 (2014) 596–601.
[94] S.K. Singh, M.K. Singh, P.P. Kulkarni, V.K. Sonkar, J.J. Grácio, D. Dash, Amine-modified graphene: thrombo-protective safer alternative to graphene oxide for biomedical applications, ACS Nano 6 (3) (2012) 2731–2740.
[95] A. Sasidharan, S. Swaroop, C.K. Koduri, C.M. Girish, P. Chandran, L. Panchakarla, V.H. Somasundaram, G.S. Gowd, S. Nair, M. Koyakutty, Comparative in vivo toxicity, organ biodistribution and immune response of pristine, carboxylated and PEGylated few-layer graphene sheets in Swiss albino mice: a three month study, Carbon 95 (2015) 511–524.
[96] S. Zhang, K. Yang, L. Feng, Z. Liu, In vitro and in vivo behaviors of dextran functionalized graphene, Carbon 49 (12) (2011) 4040–4049.
[97] X. Zhang, J. Yin, C. Peng, W. Hu, Z. Zhu, W. Li, C. Fan, Q. Huang, Distribution and biocompatibility studies of graphene oxide in mice after intravenous administration, Carbon 49 (3) (2011) 986–995.
[98] K. Wang, J. Ruan, H. Song, J. Zhang, Y. Wo, S. Guo, D. Cui, Biocompatibility of graphene oxide, Nanoscale Res. Lett. 6 (8) (2011) 1–8.
[99] J.-H. Liu, S.-T. Yang, H. Wang, Y. Chang, A. Cao, Y. Liu, Effect of size and dose on the biodistribution of graphene oxide in mice, Nanomedicine 7 (12) (2012) 1801–1812.
[100] K. Yang, S. Zhang, G. Zhang, X. Sun, S.-T. Lee, Z. Liu, Graphene in mice: ultrahigh in vivo tumor uptake and efficient photothermal therapy, Nano Lett. 10 (9) (2010) 3318–3323.
[101] K. Yang, J. Wan, S. Zhang, Y. Zhang, S.-T. Lee, Z. Liu, In vivo pharmacokinetics, long-term biodistribution, and toxicology of PEGylated graphene in mice, ACS Nano 5 (1) (2010) 516–522.
[102] S. Kanakia, J. Toussaint, D.M. Hoang, S. Mullick Chowdhury, S. Lee, K.R. Shroyer, W. Moore, Y.Z. Wadghiri, B. Sitharaman, Towards an advanced graphene-based magnetic resonance imaging contrast agent: sub-acute toxicity and efficacy studies in small animals, Scie. Rep. 5 (2015) 17182.
[103] S. Kanakia, J.D. Toussaint, S.M. Chowdhury, T. Tembulkar, S. Lee, Y.-P. Jiang, R.Z. Lin, K.R. Shroyer, W. Moore, B. Sitharaman, Dose ranging, expanded acute toxicity and safety pharmacology studies for intravenously administered functionalized graphene nanoparticle formulations, Biomaterials 35 (25) (2014) 7022–7031.
[104] D.A. Jasim, C. Ménard-Moyon, D. Bégin, A. Bianco, K. Kostarelos, Tissue distribution and urinary excretion of intravenously administered chemically functionalized graphene oxide sheets, Chem. Sci. (2015).
[105] K. Yang, H. Gong, X. Shi, J. Wan, Y. Zhang, Z. Liu, In vivo biodistribution and toxicology of functionalized nano-graphene oxide in mice after oral and intraperitoneal administration, Biomaterials 34 (11) (2013) 2787–2795.
[106] H. Ali-Boucetta, D. Bitounis, R. Raveendran-Nair, A. Servant, J. Van den Bossche, K. Kostarelos, Purified graphene oxide dispersions lack in vitro cytotoxicity and in vivo pathogenicity, Adv. Healthcare Mater. 2 (3) (2013) 433–441.
[107] A. Sahu, W.I. Choi, G. Tae, A stimuli-sensitive injectable graphene oxide composite hydrogel, Chem. Commun. 48 (47) (2012) 5820–5822.

[108] B. Strojny, N. Kurantowicz, E. Sawosz, M. Grodzik, S. Jaworski, M. Kutwin, M. Wierzbicki, A. Hotowy, L. Lipińska, A. Chwalibog, Long term influence of carbon nanoparticles on health and liver status in rats, PLoS One 10 (12) (2015), e0144821.
[109] C. Fu, T. Liu, L. Li, H. Liu, Q. Liang, X. Meng, Effects of graphene oxide on the development of offspring mice in lactation period, Biomaterials 40 (2015) 23–31.
[110] D. Zhang, Z. Zhang, Y. Liu, M. Chu, C. Yang, W. Li, Y. Shao, Y. Yue, R. Xu, The short-and long-term effects of orally administered high-dose reduced graphene oxide nanosheets on mouse behaviors, Biomaterials 68 (2015) 100–113.
[111] Q. Wu, L. Yin, X. Li, M. Tang, T. Zhang, D. Wang, Contributions of altered permeability of intestinal barrier and defecation behavior to toxicity formation from graphene oxide in nematode *Caenorhabditis elegans*, Nanoscale 5 (20) (2013) 9934–9943.
[112] A. Schinwald, F.A. Murphy, A. Jones, W. MacNee, K. Donaldson, Graphene-based nanoplatelets: a new risk to the respiratory system as a consequence of their unusual aerodynamic properties, ACS Nano 6 (1) (2012) 736–746.
[113] M.C. Duch, G.S. Budinger, Y.T. Liang, S. Soberanes, D. Urich, S.E. Chiarella, L.A. Campochiaro, A. Gonzalez, N.S. Chandel, M.C. Hersam, Minimizing oxidation and stable nanoscale dispersion improves the biocompatibility of graphene in the lung, Nano Lett. 11 (12) (2011) 5201–5207.
[114] B. Li, J. Yang, Q. Huang, Y. Zhang, C. Peng, Y. Zhang, Y. He, J. Shi, W. Li, J. Hu, Biodistribution and pulmonary toxicity of intratracheally instilled graphene oxide in mice, NPG Asia Mater. 5 (4) (2013), e44.
[115] L. Yan, Y. Wang, X. Xu, C. Zeng, J. Hou, M. Lin, J. Xu, F. Sun, X. Huang, L. Dai, Can graphene oxide cause damage to eyesight? Chem. Res. Toxicol. 25 (6) (2012) 1265–1270.
[116] M. Sawangphruk, P. Srimuk, P. Chiochan, T. Sangsri, P. Siwayaprahm, Synthesis and antifungal activity of reduced graphene oxide nanosheets, Carbon 50 (14) (2012) 5156–5161.
[117] O. Akhavan, E. Ghaderi, Toxicity of graphene and graphene oxide nanowalls against bacteria, ACS Nano 4 (10) (2010) 5731–5736.
[118] X. Cai, M. Lin, S. Tan, W. Mai, Y. Zhang, Z. Liang, Z. Lin, X. Zhang, The use of polyethyleneimine-modified reduced graphene oxide as a substrate for silver nanoparticles to produce a material with lower cytotoxicity and long-term antibacterial activity, Carbon 50 (10) (2012) 3407–3415.
[119] J. Chen, X. Wang, H. Han, A new function of graphene oxide emerges: inactivating phytopathogenic bacterium *Xanthomonas oryzae* pv. *oryzae*, J. Nanopart. Res. 15 (5) (2013) 1–14.
[120] C.M. Santos, J. Mangadlao, F. Ahmed, A. Leon, R.C. Advincula, D.F. Rodrigues, Graphene nanocomposite for biomedical applications: fabrication, antimicrobial and cytotoxic investigations, Nanotechnology 23 (39) (2012) 395101.
[121] I.E.M. Carpio, C.M. Santos, X. Wei, D.F. Rodrigues, Toxicity of a polymer–graphene oxide composite against bacterial planktonic cells, biofilms, and mammalian cells, Nanoscale 4 (15) (2012) 4746–4756.
[122] W. Hu, C. Peng, W. Luo, M. Lv, X. Li, D. Li, Q. Huang, C. Fan, Graphene-based antibacterial paper, ACS Nano 4 (7) (2010) 4317–4323.
[123] A. Áde Leon, On the antibacterial mechanism of graphene oxide (GO) Langmuir–Blodgett films, Chem. Commun. 51 (14) (2015) 2886–2889.
[124] L. Hui, J.G. Piao, J. Auletta, K. Hu, Y. Zhu, T. Meyer, H. Liu, L. Yang, Availability of the basal planes of graphene oxide determines whether it is antibacterial, ACS Appl. Mater. Interfaces 6 (15) (2014) 13183–13190.
[125] J. Li, G. Wang, H. Zhu, M. Zhang, X. Zheng, Z. Di, X. Liu, X. Wang, Antibacterial activity of large-area monolayer graphene film manipulated by charge transfer, Sci. Report. 4 (2014) 4359.
[126] N. Kurantowicz, E. Sawosz, S. Jaworski, M. Kutwin, B. Strojny, M. Wierzbicki, J. Szeliga, A. Hotowy, L. Lipińska, R. Koziński, Interaction of graphene family materials with *Listeria monocytogenes* and *Salmonella enterica*, Nanoscale Res. Lett. 10 (1) (2015) 1–12.
[127] S. Liu, T.H. Zeng, M. Hofmann, E. Burcombe, J. Wei, R. Jiang, J. Kong, Y. Chen, Antibacterial activity of graphite, graphite oxide, graphene oxide, and reduced graphene oxide: membrane and oxidative stress, ACS Nano 5 (9) (2011) 6971–6980.
[128] S. Liu, M. Hu, T.H. Zeng, R. Wu, R. Jiang, J. Wei, L. Wang, J. Kong, Y. Chen, Lateral dimension-dependent antibacterial activity of graphene oxide sheets, Langmuir 28 (33) (2012) 12364–12372.
[129] P. Begum, R. Ikhtiari, B. Fugetsu, Graphene phytotoxicity in the seedling stage of cabbage, tomato, red spinach, and lettuce, Carbon 49 (12) (2011) 3907–3919.
[130] M.V. Khodakovskaya, K. de Silva, D.A. Nedosekin, E. Dervishi, A.S. Biris, E.V. Shashkov, E.I. Galanzha, V.P. Zharov, Complex genetic, photothermal, and photoacoustic analysis of nanoparticle–plant interactions, Proc. Natl. Acad. Sci. 108 (3) (2011) 1028–1033.
[131] F. Ahmed, D.F. Rodrigues, Investigation of acute effects of graphene oxide on wastewater microbial community: a case study, J. Hazard. Mater. 256 (2013) 33–39.
[132] W. Xing, G. Lalwani, I. Rusakova, B. Sitharaman, Degradation of graphene by hydrogen peroxide, Part. Part. Syst. Charact. 31 (7) (2014) 745–750.
[133] G. Lalwani, W. Xing, B. Sitharaman, Enzymatic degradation of oxidized and reduced graphene nanoribbons by lignin peroxidase, J. Mater. Chem. B 2 (37) (2014) 6354–6362.
[134] Y. Ma, H. Shen, X. Tu, Z. Zhang, Assessing in vivo toxicity of graphene materials: current methods and future outlook, Nanomedicine 9 (10) (2014) 1565–1580.
[135] W. Zhang, C. Wang, Z. Li, Z. Lu, Y. Li, J.J. Yin, Y.T. Zhou, X. Gao, Y. Fang, G. Nie, Unraveling stress-induced toxicity properties of graphene oxide and the underlying mechanism, Adv. Mater. 24 (39) (2012) 5391–5397.
[136] T. Wang, S. Zhu, X. Jiang, Toxicity mechanism of graphene oxide and nitrogen-doped graphene quantum dots in RBCs revealed by surface-enhanced infrared absorption spectroscopy, Toxicol. Res. (2015).
[137] K. Liu, J.-J. Zhang, F.-F. Cheng, T.-T. Zheng, C. Wang, J.-J. Zhu, Green and facile synthesis of highly biocompatible graphene nanosheets and its application for cellular imaging and drug delivery, J. Mater. Chem. 21 (32) (2011) 12034–12040.
[138] J. Huang, C. Zong, H. Shen, M. Liu, B. Chen, B. Ren, Z. Zhang, Mechanism of cellular uptake of graphene oxide studied by surface-enhanced raman spectroscopy, Small 8 (16) (2012) 2577–2584.
[139] H. Ren, C. Wang, J. Zhang, X. Zhou, D. Xu, J. Zheng, S. Guo, J. Zhang, DNA cleavage system of nanosized graphene oxide sheets and copper ions, ACS Nano 4 (12) (2010) 7169–7174.
[140] L. Zhang, Z. Wang, Z. Lu, H. Shen, J. Huang, Q. Zhao, M. Liu, N. He, Z. Zhang, PEGylated reduced graphene oxide as a superior ssRNA delivery system, J. Mater. Chem. B 1 (6) (2013) 749–755.
[141] M. Wu, R. Kempaiah, P.-J.J. Huang, V. Maheshwari, J. Liu, Adsorption and desorption of DNA on graphene oxide studied by fluorescently labeled oligonucleotides, Langmuir 27 (6) (2011) 2731–2738.
[142] Y. Li, H. Yuan, A. von dem Bussche, M. Creighton, R.H. Hurt, A.B. Kane, H. Gao, Graphene microsheets enter cells through spontaneous membrane penetration at edge asperities and corner sites, Proc. Natl. Acad. Sci. 110 (30) (2013) 12295–12300.
[143] A.V. Titov, P. Král, R. Pearson, Sandwiched graphene–membrane superstructures, ACS Nano 4 (1) (2009) 229–234.
[144] Y. Tu, M. Lv, P. Xiu, T. Huynh, M. Zhang, M. Castelli, Z. Liu, Q. Huang, C. Fan, H. Fang, Destructive extraction of phospholipids from *Escherichia coli* membranes by graphene nanosheets, Nat. Nanotechnol. 8 (8) (2013) 594–601.
[145] M. Nurunnabi, Z. Khatun, K.M. Huh, S.Y. Park, D.Y. Lee, K.J. Cho, Y.-k. Lee, In vivo biodistribution and toxicology of carboxylated graphene quantum dots, ACS Nano 7 (8) (2013) 6858–6867.
[146] G. Lalwani, Two- and three-dimensional all-carbon nanomaterial assemblies for tissue engineering and regenerative medicine, Ann. Biomed. Eng. (2016) 1–16, http://dx.doi.org/10.1007/s10439-016-1623-5 (Early View Online).
[147] Lalwani, G., M. D'Agati, A. Gopalan, M. Rao, J. Schneller, and B. Sitharaman, Three-dimensional macroporous graphene scaffolds for tissue engineering. J. Biomed. Mater. Res. Part A – (Accepted for publication), 2016.
[148] B. Farshid, G. Lalwani, M. Shir Mohammadi, J. Simonsen, B. Sitharaman, Boron nitride nanotubes and nanoplatelets as reinforcing agents of polymeric matrices for bone tissue engineering, J. Biomed. Mater. Res. B Appl. Biomater. (2015), http://dx.doi.org/10.1002/jbm.b.33565 (Early View Online).
[149] J.T. Rashkow, Y. Talukdar, G. Lalwani, B. Sitharaman, Interactions of 1D-and 2D-layered inorganic nanoparticles with fibroblasts and human mesenchymal stem cells, Nanomedicine 10 (11) (2015) 1693–1706.
[150] W.Z. Teo, E.L.K. Chng, Z. Sofer, M. Pumera, Cytotoxicity of exfoliated transition-metal dichalcogenides (MoS_2, WS_2, and WSe_2) is lower than that of graphene and its analogues, Chem. Eur. J. 20 (31) (2014) 9627–9632.
[151] E.L.K. Chng, Z. Sofer, M. Pumera, MoS_2 exhibits stronger toxicity with increased exfoliation, Nanoscale 6 (23) (2014) 14412–14418.